August 2017

Sparse MRI and CT Reconstruction

Ali Pouryazdanpanah Kermani
University of Nevada, Las Vegas, ali.pouryazdanpanah@gmail.com

SPARSE MRI AND CT RECONSTRUCTION

By

Ali Pouryazdanpanah Kermani

Bachelor of Science in Electrical and Computer Engineering
University of Science and Research
2007

Master of Science in in Electrical and Computer Engineering
University of Science and Research
2010

A dissertation submitted in partial fulfillment
of the requirements for the

Doctor of Philosophy - Electrical Engineering

Department of Electrical and Computer Engineering
Howard R. Hughes College of Engineering
The Graduate College

University of Nevada, Las Vegas
May 2017

UNLV | GRADUATE COLLEGE

Dissertation Approval

The Graduate College
The University of Nevada, Las Vegas

May 4, 2017

This dissertation prepared by

Ali Pouryazdanpanah Kermani

entitled

Sparse MRI and CT Reconstruction

is approved in partial fulfillment of the requirements for the degree of

Doctor of Philosophy - Electrical Engineering
Department of Electrical and Computer Engineering

Emma Regentova, Ph.D.
Examination Committee Chair

Kathryn Hausbeck Korgan, Ph.D.
Graduate College Interim Dean

Venkatesan Muthukumar, Ph.D.
Examination Committee Member

Shahram Latifi, Ph.D.
Examination Committee Member

Alexander Barzilov, Ph.D.
Graduate College Faculty Representative

ABSTRACT

Sparse signal reconstruction is of the utmost importance for efficient medical imaging, conducting accurate screening for security and inspection, and for non-destructive testing. The sparsity of the signal is dictated by either feasibility, or the cost and the screening time constraints of the system. In this work, two major sparse signal reconstruction systems such as compressed sensing magnetic resonance imaging (MRI) and sparse-view computed tomography (CT) are investigated.

For medical CT, a limited number of views (sparse-view) is an option for whether reducing the amount of ionizing radiation or the screening time and the cost of the procedure. In applications such as non-destructive testing or inspection of large objects, like a cargo container, one angular view can take up to a few minutes for only one slice. On the other hand, some views can be unavailable due to the configuration of the system. A problem of data sufficiency and on how to estimate a tomographic image when the projection data are not ideally sufficient for precise reconstruction is one of two major objectives of this work. Three CT reconstruction methods are proposed: algebraic iterative reconstruction-reprojection (AIRR), sparse-view CT reconstruction based on curvelet and total variation regularization (CTV), and sparse-view CT reconstruction based on nonconvex L1-L2 regularization. The experimental results confirm a high performance based on subjective and objective quality metrics. Additionally, sparse-view neutron-photon tomography is studied based on Monte-Carlo modelling to demonstrate shape reconstruction, material discrimination and visualization based on the proposed 3D object reconstruction method and material discrimination signatures.

One of the methods for efficient acquisition of multidimensional signals is the compressed sensing (CS). A significantly low number of measurements can be obtained in different ways, and

one is undersampling, that is sampling below the Shannon-Nyquist limit. Magnetic resonance imaging (MRI) suffers inherently from its slow data acquisition. The compressed sensing MRI (CSMRI) offers significant scan time reduction with advantages for patients and health care economics. In this work, three frameworks are proposed and evaluated, i.e., CSMRI based on curvelet transform and total generalized variation (CT-TGV), CSMRI using curvelet sparsity and nonlocal total variation: CS-NLTV, CSMRI that explores shearlet sparsity and nonlocal total variation: SS-NLTV. The proposed methods are evaluated experimentally and compared to the previously reported state-of-the-art methods. Results demonstrate a significant improvement of image reconstruction quality on different medical MRI datasets.

DEDICATION

This study is dedicated to my parents.

Without their continued and unconditional love and support, I would not be the person I am today.

TABLE OF CONTENTS

LIST OF TABLES

LIST OF FIGURES

CHAPTER 1- INTRODUCTION

1.1. Imaging Models: CT and MRI

Imaging includes acquisition, processing, interpretation and visualization. Image modelling is one of fundamental problems underlying the whole range of imaging tasks [1-4]. The models that are studied and developed in this work are designed for reconstructing images obtained from two different physical systems, i.e., tomographic and nuclear magnetic resonance. In the former, multiple projections of an object under x-ray scan are acquired; and in the latter, scanned objects are exposed to magnetic fields and radiofrequency pulses to record magnetic gradients and place them into frequency space. As the data primarily serve for human observers the acquired signals are to be reconstructed to images such that they represent shapes, textures and structures. The quality of reconstructed images at low computation and acquisition is the focus of this work.

1.1.1. CT

Computed tomography (CT) is an x-ray imaging procedure that is performed by scanning objects and creating projections from different view angles followed by mathematical reconstruction of scenes from those projections. CT is used in various fields. An important and well-known application is the medical CT. Other examples include security and inspection, non-destructive testing, biomedical imaging, material science, and geophysics. Figure 1.1 depicts the CT system that takes projections from two angles. The system that includes the CT scanner and a reconstruction method is called a CT-scanner or CT machine. CT machines have been established as an indispensable medical imaging tool for decades, and it is still is a subject of the active

research. The modern CT-machines are designed for classical reconstruction methods such as filtered backprojection (FBP) [5]. The achievable image quality is proportional to the number of angles the projections are taken from, and that in turn is proportional to the ionizing radiation patients receive. In order to obtain an image of a sufficiently high quality, a relatively high number of angles is to be used. Another concern is the time and the cost of the procedure. While the time is highly reduced by modern technologies as well as a radiation dose related to the x-ray power for obtaining a high-quality image, they are still are hindering factors of safe and low cost applications of CT. That is specifically true for security and inspection wherein a very high power such as 10-20 MeV is used for inspection of large cargo containers or turbines.

1.1.1.1. Sparse-view CT

The main advantage of sparse-view CT (Figure 1.2) is a lower radiation dose and faster scanning for higher dimension ($\geq$ 2D) imaging. The challenge here lies in how to accurately reconstruct images from severely undersampled projection data. Such reconstruction is known in mathematics as an ill-posed problem. In order to improve the reconstruction and regularize the solution of an ill-posed problem, it is necessary to use advanced methods such as modern iterative CT reconstruction methods with the cost function that includes regularization.

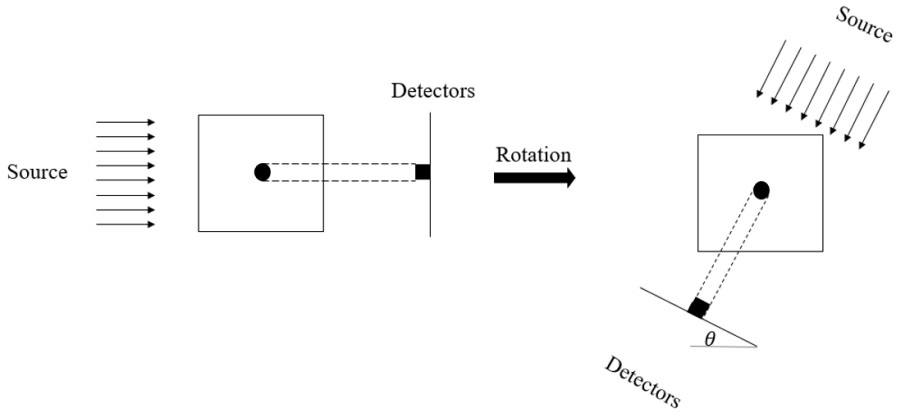

Figure 1.1 Computed tomography system: projections from two angles (two views).

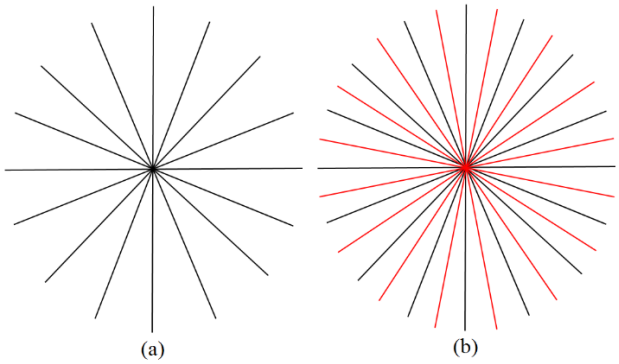

Figure 1.2 Sparse-view (few-views): (a) 16 angles; (b) 32 angles.

A computed tomography system can be defined as a linear equation:

$$A\mathrm{x} = b \tag{1}$$

where $b \in \mathbb{R}^N$ is the projection data, $\mathrm{x} \in \mathbb{R}^M$ is the reconstruction image, $A \in \mathbb{R}^{N \times M}$ is the system geometry matrix. Considering the sparse-view model, the reconstruction problem is ill-posed for minimizing the least-squares function. As a result, the following cost function with a regularization term has been considered:

$$\min_{x} |\Phi(\mathrm{x})|_1 \quad subject\ to \quad \|b - A\mathrm{x}\|_2^2 \leq \sigma \tag{2}$$

where Φ is a sparsifying transform, and σ is an upper bound of the uncertainty in the projections (b). Here ℓ_1-norm denoted by $|.|_1$ and ℓ_2-norm by $\|.\|_2$. Total Variation (TV) regularization methods [6, 7] is very well suited for edge-preserving imaging problems in sparse-view settings. A drawback of the TV-based methods is that they produce images with oil-painting artifact.

In the next chapter, we will briefly summarize the classical approach to solving the inverse problem and then introduce three sparse-view CT reconstruction methods including AIRR, CTV, and Nonconvex L1-L2 CT methods.

1.1.2. MRI

MRI is a powerful non-invasive medical imaging modality. In addition to its nonionizing radiation nature, a distinct advantage of MRI compared to other imaging modalities, such as CT, x-ray radiography, and nuclear medicine, is that MRI is able to provide superior contrasts based on the intrinsic properties of soft tissues.

Compressed sensing (CS) implies that signals are reconstructed from significantly fewer measurements than were traditionally thought necessary (Shannon-Nyquist sampling theorem). Magnetic resonance imaging (MRI) are featured by slow data acquisition process. The CS MRI has a high potential of significant reduction of the scan time. Twofold benefit from CS MRI is the patients' convenience and the lower cost of the procedure. Compressed sensing for MRI is potentially successful because 1) imagery is inherently compressible in the transform domain (for example, wavelet domain), and 2) MRI scanners obtain samples in the spatial-frequency domain.

1.1.2.1. Compressed sensing MRI (CSMRI)

Compressed sensing [8-10] framework (Figure 1.3) plays an important role in signal processing applications now days and shows remarkable results. Signal reconstruction and specifically reconstruction of magnetic resonance images is one of those fundamental applications especially for very sparse data samples compared to the standard sampling theory. The gain is twofold; with the high quality, given the sparse sampling, there is a significant speed up of the scan time for magnetic resonance imaging [8,11].

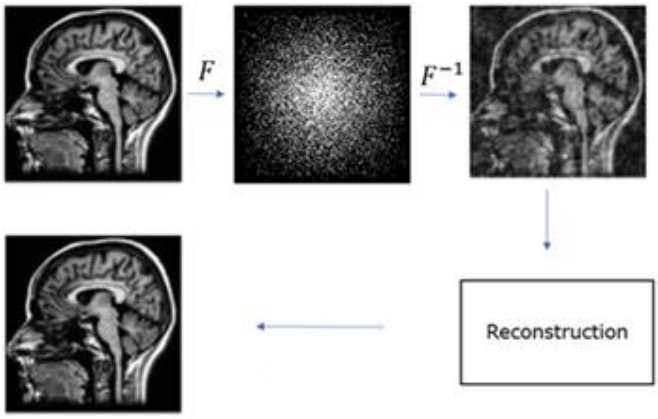

Figure 1.3 Compressed sensing MRI framework

Compressed sensing hypothesis [9] makes it possible to recover MR images from vastly under-sampled k-space data and the whole process includes encoding, sensing, and decoding processes. Most of the compressed MR imaging algorithm try to solve following linear model:

$$A\mathrm{x} = b \tag{3}$$

when

$$A = SF \tag{4}$$

where S is a sampling, or a selection matrix, and F is a 2D discrete Fourier matrix, and b is the observed k-space data which invades the classical Shannon–Nyquist sampling criterion. Having the sparsity assumption of $\hat{\mathrm{x}}$, one possible solution would be

$$\min_{\mathrm{x}} |\mathrm{x}|_0 \text{ subject to } A\mathrm{x} = b \tag{5}$$

Since ℓ_o-minimization problem is an NP-hard [12], a more reasonable alternative would be

$$\min_{\mathrm{x}} \ |\mathrm{x}|_1 \ \text{subject to} \ A\mathrm{x} = b \tag{6}$$

Almost all the recent CS MRI algorithms are the generalized versions of that with different regularization and penalty terms.

He et al. [13] proposed a model for compressed MR imaging using two non-smooth regularization terms which reached better accuracies compared to the traditional total variation regularization model [14]. Chang et al. [15] proposed partial differential equation (PDE) based method to reconstruct MR images. Lysaker et al. [16] improved the quality of reconstructed images by introducing fourth-order regularization term in their compressed MR imaging model, but the model was too complex to solve for high resolution images. Lustig et al. [17] reviewed different compressed MR imaging steps. They developed the model using the sparsity in a wavelet domain and exploited ℓ_1-minimization to reconstruct MR image. Jung et al. [18], Ye et al. [19], Candes et al. [20], and Chartrand et al. [21], exploited ℓ_p-quasinorm minimization model $0 < p < 1$ using the method FOCUSS [22] to reconstruct MR images, but because of non-convexity of their objective function, the optimization may not end up with global minima. Trzasko et al. [23] also proposed homotopic nonconvex objective function based on ℓ_0 minimization model, however it has the global minima issue.

Recent CS MRI strive to find a best combination of sparsifying transforms in order to increase the reconstruction quality from a very sparse data space [24-29]. In recent, different methods have been presented to reconstruct magnetic resonance images from under sampled k-

space data. Ma et al., introduced an operator-splitting algorithm, Total variation (TV) compressed MR imaging (TVCMRI) [24] for MR image reconstruction. By taking advantage of fast wavelet and Fourier transforms, TVCMRI can process actual MR data accurately. Another method proposed by Yang et al. [25] solved the same objective function presented in [24] differently. They proposed a variable splitting method (RecPF) which is TV-based ℓ_1-ℓ_2 MR reconstruction. This method uses alternating direction method for recovering MRI images from incomplete Fourier measurements. The optimization, was solved based on the approach in [26]. A fast composite splitting algorithm (FCSA) [27] is proposed by Huang et al. FCSA is based on combination of variable and operator splitting. It splits the variable x, that is an image to reconstruct into two variables; and it exploits operator splitting to minimize the regularization terms over the splitting variables. Nonlocal total variation for MR reconstruction (NTVMR) [28], and framelet + nonlocal TV (FNTV) [29] have been proposed lately. Unlike the immense reputation of all TV-based minimization approaches, these methods, which are based on the first order derivatives, have two major shortcomings such as oil-painting artifacts, and/or contrast loss [30]. Out of those two methods which use nonlocal TV regularization, FNTV functions better in terms of quality. FNTV tries to minimize the combination of nonlocal TV, framelet, and least square data fitting terms using the split Bregman method. Recently, Shearlet based methods are proposed for MR reconstruction purposes [31, 32]. In [32], a new framework, nonseparable shearlet transform iterative soft thresholding reconstruction algorithm (FNSISTRA), is presented by Pejoski et al. which used both fast iterative soft thresholding algorithm (FISTA) [34,35] and discrete nonseparable shearlet transform (DNST) [33] to solve their reconstruction formulation. They modified FISTA algorithm to exploit the 2D DFT of the spatial domain to solve their minimization formulation. Not only their result accomplished better signal to noise ratio (SNR) compared to

previously shearlet based method [31], but also, they achieved better performance compared to all previously mentioned methods.

In the next chapter, three compressed sensing MRI methods are proposed including CT-TGV, CS-NLTV, and SS-NLTV.

CHAPTER 2- METHODS

In this chapter, six methods for CT and MRI reconstruction are proposed. Furthermore, the 3D object reconstruction method and a novel material discrimination for sparse-view neutron-photon CT are elaborated.

2.1. Computed tomography reconstruction

In this section, three proposed CT reconstruction methods including AIRR, CTV, and Nonconvex L1-L2 CT and the proposed 3D object reconstruction and material discrimination methods in sparse-view Neutron-Photon computed tomography are explained.

2.1.1. Computed tomography method: algebraic iterative reconstruction-reprojection (AIRR) method

In this section, we introduce the shearlet regularization in an algebraic iterative reconstruction-re-projection (AIRR) for the sparse-view CT reconstruction. When the sparsity increases, the reconstruction error causes a large divergence. The iterative reconstruction-re-projection (IRR) algorithm [36,37] based on the filtered back projection (FBP) has served initially for the sparse-view CT reconstruction. The IRR-TV [38] has had a higher performance on the account of the total variation (TV) minimization. In this section, we first review the IRR and then introduce the algebraic iterative reconstruction-reprojection with the shearlet regularization in the image space. We will show then that a better approximation in the projection space is attained and a better quality of reconstruction evaluated by subjective and objective quality metrics is produced by the proposed AIRR.

2.1.1.1. Traditional IRR method

The IRR is a transformation reconstruction method which approximates the absent angular projections by alternating back-projection and reprojection spaces. It is arithmetically similar to the Gerchberg-Papoulis method that iterates in the Fourier space. It is shown that it converges for the case of band-limiting data [39, 40].

The IRR method includes three steps:

$$g^i(r,\theta) = h(r) * p^i(r,\theta) \tag{7}$$

$$f^i(r,\theta) = \int_0^{2\pi} g^i(xcos(\theta) + ysin(\theta))d\theta \tag{8},$$

$$p_{rep}^{i+1}(r,\theta) = \int_{-L}^{L} f^i(rcos(\theta) - tsin(\theta), rsin(\theta) + tcos(\theta))dt \tag{9}.$$

In the above equations, $g^i(r,\theta)$ is the i-th reconstruction of the filtered projection data, $h(r)$ is the time-domain filter. $p_{rep}^{i}(r,\theta)$ is the reprojection data computed from (i-1)th reconstructed image, f^{i-1} .

The error propagation presented in the back-projection and reprojection iterations is the key drawback of the IRR algorithm. In [36], authors combined Eq. (8) and Eq. (9) into one stage in the projection space to decrease the interpolation error as follows:

$$p_{rep}^{i+1}(r,\theta) = 2Lsin(\theta_m)g^i(r,\theta) + \int_0^{\pi} \int_{L\cos(\theta-\acute{\theta}+\theta_m)}^{L\cos(\theta-\acute{\theta}-\theta_m)} \frac{g^i(\acute{r},\acute{\theta})}{\sin(\theta-\acute{\theta})} d\acute{r}d\acute{\theta} \quad (10),$$

where $\theta_m = \cos^{-1}(l/L)$ and L is the reconstructed region radius. This technique is computationally expensive, and after few iterations the divergence is occurred.

In [38], Duan et. al utilized the total variation to expand the IRR accuracy by inserting the TV step to the technique. The TV-based model is defined as below:

$$\min TV(f) \ st. \ Mf = p \quad (11),$$

where M is a measurement matrix, and p is the sparse-view projection.

$$TV(f) = \sqrt{(f_{x,y} - f_{x-1,y})^2 + (f_{x,y} - f_{x,y-1})^2} \quad (12),$$

where $TV(f)$ is the TV of the 2D image, f. The whole procedure is defined then by Eq. (13).

$$\hat{f} = \hat{f} - d\frac{\partial TV(\hat{f})}{\partial \hat{f}} \quad (13)$$

where $\hat{f}$ is the reconstructed image from projection p obtained by FBP algorithm. The IRR+TV method performs better than its traditional counterpart, under the rigorously controlled number of iterations. The IRR-TV reconstruction method splits the whole procedure in the image and the projection spaces and applies TV in the image domain to attain sparse-view projections. While the IRR-TV has a higher performance compared to the traditional IRR algorithm, the number of iterations is rigorously controlled for preventing the divergence which occurs after just few iterations.

2.1.1.2. AIRR method

In the AIRR method, the reconstruction procedure is defined as a linear equation for two different cases: a noise-free described by Eq. (14) and the noisy case given by Eq. (15).

$$Af = b \tag{14}$$

$$Af + n = b \tag{15}$$

where $A \in \mathbb{R}^{N \times M}$ is the system geometry matrix, $b \in \mathbb{R}^{N}$ is the projection data, and $f \in \mathbb{R}^{M}$ is the reconstruction result,

The AIRR algorithm includes three processes in each iteration:

- Iterative Algebraic Reconstruction
- Shearlet-based denoising
- Reprojection

2.1.1.2.1. Iterative algebraic reconstruction

The FBP method is replaced by simultaneous algebraic reconstruction technique (SART) [41] with a stopping criteria. The SART convergence has been proved in [43].

The reconstruction of f is performed by iterating as follows:

$$f^{k+1} = f^k + \lambda_k C^{-1} V A^T W (b - A f^k) \tag{16}$$

where $V = diag(1/\sum_{i=1}^{N} a_{i,j})$ for $j = 1, .., M$ and $V = diag\left(1/\sum_{j=1}^{M} a_{i,j}\right)$ for $i = 1, .., N$. C is the exponential weighting matrix which moderates the errors due to large values of b [42, 44].

$$C = diag(c_0, c_1, \dots, c_i) \quad when \;\; c_i = e^{-E[b_i]} \tag{17}$$

Projection values are used to estimate $E[b_i]$. Algebraic reconstruction is carried out with the non-negativity constraint, $\acute{f}(x, y) = 0$ for $\acute{f}(x, y) < 0$, when $\acute{f} = f^q$ if the iteration stops at $k = q$. The discrepancy principle criteria is utilized as the stopping condition by obtaining the smallest k such that

$$\left\| W^{1/2}(b - A f^k) \right\|_2 \leq \tau \delta \tag{18},$$

where τ can be found experimentally.

2.1.1.2.2. Shearlet-based denoising

The discrete shearlet transformation (DST) has been developed in [45, 46, 47, 48]. $\psi_{a,s,t}(x)$ denotes the shearlet basis functions. The continuous shearlet transformation of image $f(x)$ is defined as

$$SH_{\varphi}(a,s,t) = \int_{R^2} \acute{f}(x)\psi_{a,s,t}(t-x)dx \quad (19),$$

where $s \in R, a \in R$, and $t \in R^2$ describe the orientation, scale, and location in the spatial domain, respectively and $\acute{f}(x) \in R^2$ is a two-dimensional reconstructed image.

Shearlets are shaped by dilating, shearing and translating the $\psi_{a,s,t} \in R^2$, as below:

$$\psi_{a,s,t}(x) = \left|det\, K_{a,s}\right|^{\frac{-1}{2}} \psi\left(K_{a,s}^{-1}(x-t)\right) \quad (20)$$

$$K_{a,s} = \begin{pmatrix} a & \sqrt{a}s \\ 0 & \sqrt{a} \end{pmatrix} = BS = \begin{pmatrix} 1 & s \\ 0 & 1 \end{pmatrix}\begin{pmatrix} a & 0 \\ 0 & \sqrt{a} \end{pmatrix} \quad (21),$$

where S is an anisotropic scaling matrix with a scaling factor $a > 0$, and B is a shear matrix with a parameter $s \in R$. B and S are both invertible matrices, with $det\, B = 1$.

The ψ (mother shearlet function) is a compound wavelet which accomplishes admissibility conditions [42, 49]. The Meyer wavelet with a good localization ability in both time and frequency spaces is utilized as a mother wavelet for $\psi(\omega_x)$ in the shearlet transformation. Besides, Meyer wavelet filters are directly defined in the frequency space by $\Psi(\omega) = \Psi_1(\omega_x)\Psi_2\left(\frac{\omega_y}{\omega_x}\right)$ with $\omega = [\omega_x \omega_y]$, $\Psi_1(\omega_x)$ being Fourier transform of the wavelet function and $\Psi_2(\omega_y)$ is a compactly supported bump function $\Psi_2(\omega_y) = 0 \leftrightarrow \omega_y \notin [-1,1]$ [50, 51].

Figure 2.1 denotes the shearlet transformation subbands coefficients in the first scale, applied to Shepp–Logan phantom image (in the remainder simply called phantom) [53].

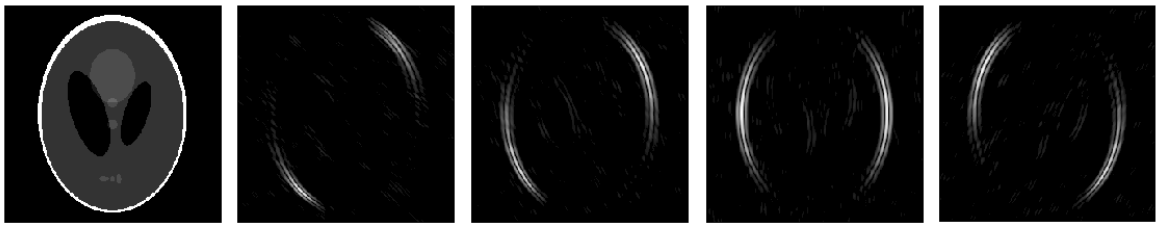

Figure 2.1 Original phantom and its shearlet transformation coefficients (first scale with four different directions)

In [52], Cunha et. al. have demonstrated a good performance of image denoising by thresholding the contourlet coefficients. We adopt the thresholding method in [52], for the shearlet shrinkage in shearlet-based denoisting step. The threshold is computed as in Eq. (22)

$$T_{i,j} = \frac{\sigma_{i,j}^2}{\sigma_{i,j,n}^2} \quad (22),$$

where $\sigma_{i,j,n}^2$ is the n-th coefficient variance at the *i-th* shearing direction subband in the *j-th* scale, and $\sigma_{i,j}^2$ is the noise variance in direction *i* at scale *j*. $\sigma_{i,j}^2$ is estimated as follows: First, the variances are calculated for a few normalized noise images and then to get an estimate of $\sigma_{i,j}^2$, all the estimates averaged. The variances of the signal in each subband are computed by utilizing the maximum likelihood estimator applied on the neighboring coefficients in a square window. After thresholding the coefficients, we reconstruct back $(x) \in R^2$:

$$\hat{f} = \sum_{a,s,t} \widehat{SH_{\varphi}} \psi_{a,s,t} \quad (23).$$

2.1.1.2.3. Reprojection

In the re-projection step, we reproject $\hat{f}$ back to the projection space using the updated geometry matrix A. In each iteration, we modify the geometry matrix and double the number of angels of the first sparse-view problem by interpolation.

If we define the sparse-view problem with $0{:}\,d{:}\,360$ angles where d is a step size, then we reproject $\hat{f}$ back into the projection space utilizing $0{:}\,\frac{d}{2}{:}\,360$ angles with A_{new} (Figure 2.2).

$$A_{new}\hat{f} = \hat{b} \quad (24)$$

Figure 2.3 shows a pseudo-code of the AIRR method.

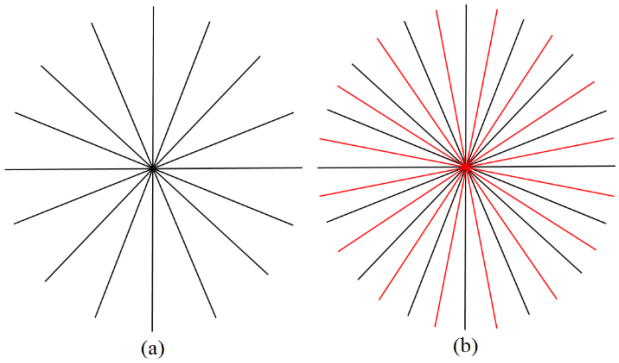

Figure 2.2 (a) Original views; (b) Angular interpolation of a) for updating the geometry matrix in reprojection phase

While $\left\|W^{1/2}(b - Af^k)\right\|_2 > \tau\delta$ {

$$f^{k+1} = f^k + \lambda_k C^{-1} V A^T W (b - Af^k)$$

}

$$\acute{f} = f^{k+1}$$

$$SH_\varphi(a,s,t) = \langle \acute{f}, \psi_{a,s,t} \rangle$$

$$\widehat{SH_\varphi} = Shrinkage\left(SH_\varphi(a,s,t), T_\alpha\right)$$

$$\hat{f} = \sum_{a,s,t} \widehat{SH_\varphi} \psi_{a,s,t}$$

$$A_{new}\hat{f} = \hat{b}$$

Figure 2.3 AIRR method

2.1.2. Computed Tomography Method: Sparse-View CT Reconstruction using Curvelet and TV-based Regularization (CTV)

In this section, we introduce a new regularization model for CT reconstruction by combining regularization based on total variation and the curvelet transform. Combining curvelet regularizer, which is optimally sparse with a better directional sensitivity than that of wavelet transforms with the total variation was expected to yield a unique regularization model for attaining a better reconstruction quality. The Split-Bregman technique has been utilized as a solver. The approach makes it easy to incorporate multiple regularization terms including the one based on the multiresolution transformation, in our case curvelet, into our optimization process.

CTV Method

A CT system can be described as a linear problem in two different cases: noise-free (Eq. (25)) and noisy (Eq. (26)):

$$A\mathrm{x} = b \tag{25}$$

$$A\mathrm{x} + n = b \tag{26},$$

where $b \in \mathbb{R}^N$ is the projection data, $\mathrm{x} \in \mathbb{R}^M$ is the reconstruction image, $A \in \mathbb{R}^{N \times M}$ is the geometry matrix, and n is the approximation of the interference of noise, error, and other factors

present in a practical imaging process. Assuming noise and the sparse-view scenario, the reconstruction process is ill-posed. Therefore, the following cost function has been considered.

$$\min_{x} |\Phi(\mathrm{x})|_1 \quad subject\ to \quad \|b - A\mathrm{x}\|_2^2 \leq \sigma \tag{27},$$

where Φ is a sparsifying transform and σ is an upper bound of the uncertainty in the projections. The constrained optimization in Eq. (27) is similar to the subsequent unconstrained problem [42, 54]:

$$\min_{x} \ |\Phi(\mathrm{x})|_1 + \lambda \ \|b - A\mathrm{x}\|_2^2 \tag{28},$$

where $\lambda > 0$ is a balancing constant which depends on the sparsity of the image x space. Considering the problem, the sparsifying term can comprise different regularizers. In this method, we formulate the optimization problem using a combination of both curvelet and TV regularizers. In the CT reconstruction:

$$|\Phi(\mathrm{x})|_1 = \alpha_{TV} \left(|\nabla_x(\mathrm{x})|_1 + \ \left|\nabla_y(\mathrm{x})\right|_1 \right) + \alpha_C |C(\mathrm{x})|_1 \tag{29},$$

where constants α_{TV} and α_C are the weighting parameters stressing the TV and curvelet terms and ∇ is the discrete gradient operator and C is the curvelet transform. TV is preferably suitable if the reconstructed data are piecewise constant throughout the image [56]. Recently, curvelet regularizer has been utilized for denoising, and for general applications like inverse problems [55, 57]. By taking advantage of a sparsity constraint in the curvelet space, we can consider the curvelet regularization as a sparsifying transform.

Since the proposed formulation include both l_1 and l_2-norm terms that complicates finding the solution in a closed-form. The split Bregman method [54] is adopted in this method.

The optimization problem

$$\hat{\mathrm{x}} = \underset{\mathrm{x}}{argmin} |\Phi(\mathrm{x})|_1 + \lambda \|b - A\mathrm{x}\|_2^2 \tag{30}$$

is solved by iterating over the following equations:

$$\mathrm{x}^{(i+1)} = \underset{\mathrm{x}}{argmin} \frac{\lambda}{2} \|b - A\mathrm{x}\|_2^2 + \frac{\mu}{2} \left\| d_{TV,x}^{(i)} - \nabla_x(\mathrm{x}) - v_{TV,x}^{(i)} \right\|_2^2 + \\ + \frac{\mu}{2} \left\| d_{TV,y}^{(i)} - \nabla_y(\mathrm{x}) - v_{TV,y}^{(i)} \right\|_2^2 + \frac{\mu}{2} \left\| d_C^{(i)} - C(\mathrm{x}) - v_C^{(i)} \right\|_2^2 \tag{31}$$

$$d_{TV,x}^{(i+1)} = \underset{d}{argmin} |d|_1 + \frac{\mu}{2} \left\| d - \nabla_x(\mathrm{x}^{(i+1)}) - v_{TV,x}^{(i)} \right\|_2^2 \tag{32}$$

$$d_{TV,y}^{(i+1)} = \underset{d}{argmin}\ |d|_1 + \frac{\mu}{2}\left\|d - \nabla_y(\mathrm{x}^{(i+1)}) - v_{TV,y}^{(i)}\right\|_2^2 \tag{33}$$

$$d_C^{(i+1)} = \underset{d}{argmin}\ |d|_1 + \frac{\mu}{2}\left\|d - C(\mathrm{x}^{(i+1)}) - v_C^{(i)}\right\|_2^2 \tag{34}$$

$$v_{TV,x}^{(i+1)} = v_{TV,x}^{(i)} + (\nabla_x(\mathrm{x}^{(i+1)}) - d_{TV,x}^{(i+1)}) \tag{35}$$

$$v_{TV,y}^{(i+1)} = v_{TV,y}^{(i)} + (\nabla_y(\mathrm{x}^{(i+1)}) - d_{TV,y}^{(i+1)}) \tag{36}$$

$$v_C^{(i+1)} = v_C^{(i)} + (C(\mathrm{x}^{(i+1)}) - d_C^{(i+1)}) \tag{37}$$

The general solution for the subproblem (31), needs finding its derivatives roots:

$$A^{\dagger}(b - A\mathrm{x}) + \frac{\mu}{\lambda}\Phi^{\dagger}\left(d^{(i)} - \Phi(\mathrm{x}) - v^{(i)}\right) = 0 \tag{38}$$

This equation can be rewritten as:

$$\left(A^{\dagger}A + \frac{\mu}{\lambda}\Phi^{\dagger}\Phi\right)\mathrm{x} = A^{\dagger}b + \frac{\mu}{\lambda}\Phi^{\dagger}\left(d^{(i)} - v^{(i)}\right) \tag{39}$$

where $\Phi^{\dagger}, A^{\dagger}$ are the backward sparsifying transformation and the back projector, respectively. However, the normal inversion cannot be acquired, since A is not a square matrix

and $\Phi^{\dagger}\Phi \neq I$, therefore, the conjugate gradient method [58] was selected as a solution for Eq. (39). The solution for d in Eq. (32 - 34), can be obtained by using a shrinkage operator as follows:

$$d^{(i+1)} = shrink\left(\Phi(x) + v^{(i)}, \frac{1}{\mu}\right) \tag{40}$$

$$shrink\ (k, t\ ) = \frac{k}{|k|}\ max(|k| - t, 0) \tag{41}$$

where k is each of the coefficients for the point-wise shrinkage operator and$t$ is a threshold.

2.1.3. Computed Tomography Method: Sparse-View CT Reconstruction Based on Nonconvex L1-L2 Regularization (Nonconvex L1-L2 CT)

As we discussed in section 2.1.2, a computed tomography system can be defined as a linear equation in two different scenarios: noise-free and noisy cases:

$$A\mathrm{x} = b \tag{42}$$

$$A\mathrm{x} + n = b \tag{43}$$

The reconstruction problem can be solved using a constrained optimization problem,

$$\underset{x}{minimize}\ |\mathrm{x}|_0 \quad subject\ to\ \ A\mathrm{x} = b \tag{44},$$

A constrained L1-L2 minimization problem can be defined by replacing L0 in Eq. (44) with L1-L2:

$$\underset{\mathrm{x}}{min}\ |\mathrm{x}|_1 - \|\mathrm{x}\|_2 \quad subject\ to \quad A\mathrm{x} = \mathrm{b} \tag{45},$$

In the optimization problem, to minimize L1-L2, a difference of convex algorithm (DCA) [59] is utilized. DCA includes linearization of the nonconvex term (second term) in the cost function to raise a new term by solving the L1-norm subproblem

$$\mathrm{x}^{k+1} = \underset{\mathrm{x}}{argmin}\ \{|\mathrm{x}|_1 - \langle p^k, \mathrm{x}\rangle \ \ subject\ to \quad A\mathrm{x} = \mathrm{b}\} \tag{46},$$

where $p^k = \frac{x^k}{\|x^k\|_2}$

The DCA method handles the minimization of a cost function in a form of Q(x) = f(x)-g(x). f(x) and g(x) are lower semi-continuous convex functions, f - g is a DC decomposition of Q. g and f are considered as DC components of Q. In the DCA method, we build two sequences x^k and z^k as nominees for primal and dual optimal solutions. They are computed by iterating over the following equations:

$$\left\{ \begin{matrix} z^k \in \partial g(x^k) \\ x^{k+1} = \underset{x}{argmin} \;\; f(x) - (g(x^k) + \langle z^k, x - x^k \rangle) \end{matrix} \right\} \quad (47),$$

where z^k is a subgradient of g(x) at x^k. The unconstrained minimization for Eq. (45):

$$\underset{x}{minimize} \;\; \frac{1}{2}\|b - Ax\|_2^2 + \lambda(|x|_1 - \|x\|_2) \quad (48)$$

The unconstrained cost function in Eq. (48) has the following DC decomposition:

$$Q(x) = \; (\frac{1}{2}\|b - Ax\|_2^2 + \lambda|x|_1) - \lambda\|x\|_2 \quad (49)$$

Considering $\|x\|_2$ is differentiable with gradient $\frac{x}{\|x\|_2}$ and for x = 0, $0 \in \partial\|x\|_2$, the following can be written:

$$\mathrm{x}^{k+1} = \begin{cases} \underset{\mathrm{x}}{argmin} \ \ \frac{1}{2}\|b - A\mathrm{x}\|_2^2 + \lambda|\mathrm{x}|_1 & \text{if} \quad \mathrm{x}^k = 0 \\ \underset{\mathrm{x}}{argmin} \ \ \frac{1}{2}\|b - A\mathrm{x}\|_2^2 + \lambda|\mathrm{x}|_1 \ - \langle \mathrm{x}, \lambda \frac{\mathrm{x}^k}{\|\mathrm{x}^k\|_2} \rangle & otherwise \end{cases} \tag{50}$$

In each DCA iteration, the following L1-norm convex subproblem is solved:

$$\underset{\mathrm{x}}{minimize} \ \ \frac{1}{2}\|b - A\mathrm{x}\|_2^2 + \lambda|\mathrm{x}|_1 \ - \langle \mathrm{x}, u \rangle \tag{51}$$

Equation (51) can be solved using alternating direction of multiplier method (ADMM) [60]. First Eq. (51) can be rewritten as

$$\underset{\mathrm{x}}{minimize} \ \ \frac{1}{2}\|b - A\mathrm{x}\|_2^2 + \lambda|v|_1 \ - \langle \mathrm{x}, u \rangle \ \ s.t. \quad \mathrm{x} - v = 0 \tag{52}$$

Then we form a Lagrangian as

$$\mathcal{L}(\mathrm{x}, v, \rho) = \ \frac{1}{2}\|b - A\mathrm{x}\|_2^2 + \lambda|v|_1 \ - \langle \mathrm{x}, u \rangle + \ \rho^T(\mathrm{x} - v) + \frac{\eta}{2}\|\mathrm{x} - v\|_2^2 \tag{53}$$

where η is the penalty parameter and ρ is the Lagrangian multiplier. ADMM iterations are as follows

$$\begin{cases} \mathrm{x}^{i+1} \ = \ \underset{\mathrm{x}}{argmin} \ \ \mathcal{L}\left(\mathrm{x}, v^i, \rho^i\right) \\ v^{i+1} = \underset{\mathrm{x}}{argmin} \ \ \mathcal{L}\left(\mathrm{x}^{i+1}, v, \rho^i\right) \\ \rho^{i+1} = \rho^i + \eta\left(\mathrm{x}^{i+1} - v^{i+1}\right) \end{cases} \tag{54}$$

The closed-form solution for v in the second step of (54) can be found using a shrinkage operator:

$$v^{i+1} = shrink(\frac{\mathrm{x}^{i+1}+\rho^{i}}{\eta}, \frac{\lambda}{\eta}) \tag{55}$$

where

$$shrink(x, \xi) = sign(x_n).\max\{|x_n - \xi|, 0\} \tag{56}$$

Since matrix A is not a square matrix, and thus the normal inversion cannot be obtained, the conjugate gradient method [58] has been chosen as a solution for the first step of Eq. (54). A pseudo-code of the solution for each DCA iteration in Eq. (51) is depicted here Figure 2.4.

Define x^0, v^0, ρ^0

for $i = 1,2,\dots,iteration$

$$\mathrm{x}^{i+1} = \underset{\mathrm{x}}{argmin}\ \mathcal{L}(\mathrm{x}, v^i, \rho^i)$$

$$v^{i+1} = shrink\left(\frac{\mathrm{x}^{i+1}+\rho^{i}}{\eta}, \frac{\lambda}{\eta}\right)$$

$$\rho^{i+1} = \rho^i + \eta(\mathrm{x}^{i+1} - v^{i+1})$$

end

Figure 2.4 DCA Iteration Solution

2.1.4. Computer tomography application

In this section, we investigate an application of computed tomography with two different radiation sources (neutrons and photons) for shape reconstruction and material classification. Combining two radiation types by using photon and neutron sources for radiography, rather than two identical sources of different energies is expected to improve visualization of objects with different attenuation and provide better material discrimination. The concept of using the ratio of the radiation transmissions through the object for two photon energies in dual-energy radiography can be applied towards the neutron and photon sources as well [61]. Neutrons and photons interact differently with matter and thus one can analyze the ratio of numbers of transmitted photons to the numbers of transmitted neutrons, in the same geometry of the radiographic system.

2.1.4.1. Computed tomography application: sparse-view fan-beam neutron-photon computed tomography

In this section, the application of the combined fan-beam neutron-photon computed tomography for reconstruction and imaging of 3D scenes has been examined using MCNP5 computer simulation [62] for objects of simple shapes with different materials. 2D transmission projections were determined in fan-beam scans utilizing accelerator-based 2.5-MeV deuterium-deuterium and 14-MeV deuterium-tritium neutron sources, and high-energy x-ray sources, such as 1MeV, 6 MeV and 9 MeV. Owing to inherent differences between neutron and photon interactions with matter and by applying a developed imaging method, objects and their material compositions have been efficiently visualized.

2.1.4.1.1. Neutron-photon configuration

A tomography model for a combined neutron and photon transmission imaging is shown in Figure 2.5. The rotary table rotates about the vertical axis through the center of the scanned object and that provides projections from different views. The rotation step is of 5°. Photon transmission, $T_p(x)$, through a specific material of a given thickness (x) and the average density (p) can be determined from Eq. (57). The mass-attenuation coefficient (μ) is dependent on the incident photon energy, and $I_p(0)$ is the recorded photon flux without container/objects in presence.

$$T_p(x) = I_p(x)/I_p(0) = e^{-\mu_p x} \tag{57}$$

Neutron transmission, $T_n(x)$, is evaluated using Eq. (58) that assumes transmission of neutrons through a specific material of a given thickness (x) and is dependent on the material's total macroscopic neutron cross-section (Σt), which is dependent on the incident neutron energy:

$$T_n(x) = I_n(x)/I_n(0) = e^{-\Sigma_t x} \tag{58}$$

One can evaluate the ratio of the photon-to-neutron transmission $(R_{p/n})$ as $T_p(x)/T_n(x)$. The feature characterizes materials based on the photon mass attenuation coefficient, material density, and the total macroscopic neutron cross-section. The feature does not require a priori information about the mass of the material present along the radiation beam path. It is possible to experimentally determine the transmission values, and consequently the transmission ratios without requiring details about the object or its geometry.

The ideal transmission ratios for a selection of materials are included in Table 2.1 Transmission ratios were calculated for two cases, (a) using 6-MeV and 9-MeV dual x-ray radiography and (b) using 2.5-MeV neutrons and 6-MeV photons. The table illustrates that values of $R_{p/n}$ are considerably more varied for the neutron-photon radiography than those of dual-energy photon radiography for the same materials. This feature makes the neutron-photon technology a better candidate for material classification.

Table 2.1 Transmission ratios for low-Z and high-Z materials.

Material	Dual-energy photon radiography, T_p (6 MeV) / T_p (9 MeV)	Combined neutron-photon radiography, T_p (6 MeV) / T_n (2.5 MeV)
Polyethylene (C2H4)	0.9537	10.7330
Water (H2O)	0.9553	5.6013
Aluminum (27Al)	0.9247	3.3370
Iron (56Fe)	0.9465	2.1702
Lead (natural)	1.6293	0.0794
Tungsten (natural)	2.1571	0.0113

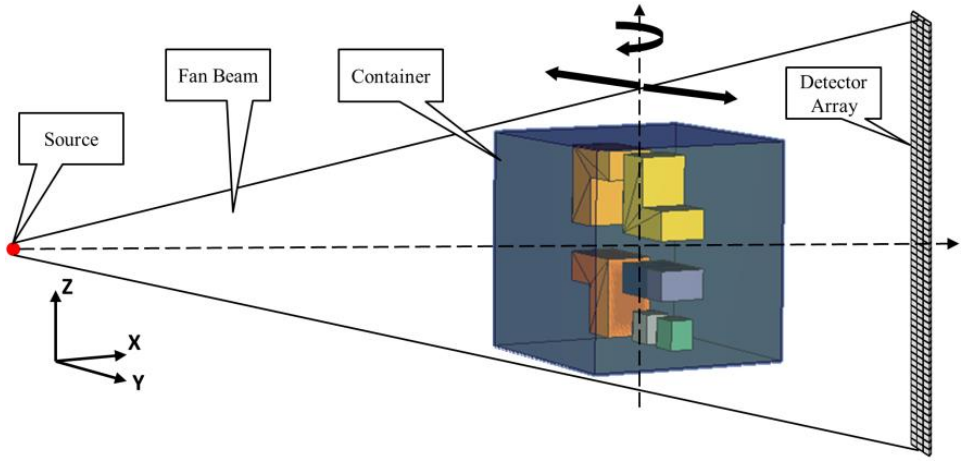

Figure 2.5 The neutron-photon CT geometry: 3D view of the source, scanned object and detector array [63]

The three-dimensional model is shown in Figure 2.5. The exterior dimensions of the container are (50×50×50) cm3, with 3-cm-thick aluminum walls. The fan beam is generated using a lead collimator. The distance between the collimator and the container is 2.39 m. With the given geometry, the beam is to be 3-cm-wide, and the detector array is placed 37 cm away behind the container wall. 2.5-MeV deuterium-deuterium (DD) and 14-MeV deuterium-tritium (DT) neutron

fusion generators are used for modelling, neutron sources. Photon sources are modelled with the end energies as high as 0.3 MeV, 1 MeV, 3 MeV, and 6 MeV.

The size of the detector array is 6 cm x 92 cm. In the image plane that corresponds to vertical strips of 3 by 100 pixels. A tomographic 2D projection of 36 pixels by 100 pixels is produced by combining transmission data in vertical columns for different orientations of the container modelled as a shift of the frame supporting the container. The container in Figure 2.6 is "filled" with objects of various sizes, shapes and materials such polyethylene (poly), iron and lead. Details about the objects and geometry are in Table 2.2.

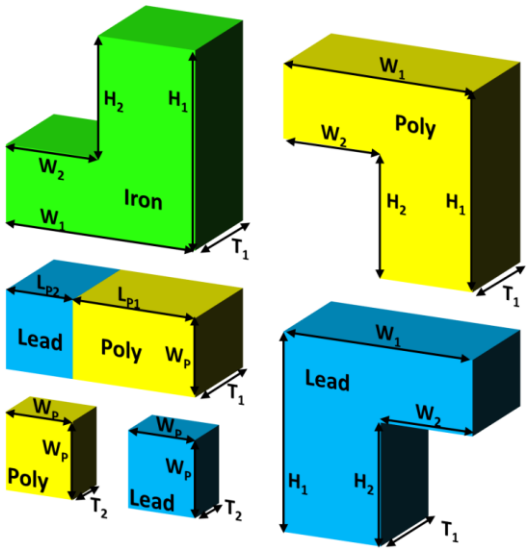

Figure 2.6 Objects placed in the container [63]

Table 2.2 Container model: geometry of objects.

Object	Quantity	Dimensions (cm)
L-shape	3	$16(H_1) \times 16(W_1) \times 10(H_2) \times 8(W_2) \times 5(T_1)$
Parallelepiped	1	$10(LP_1) \times 6(W_P) \times 10(T_1)$
Parallelepiped	1	$6(LP_2) \times 6(W_P) \times 10(T_1)$
Parallelepiped	2	$6(W_P) \times 6(W_P) \times 5(T_2)$

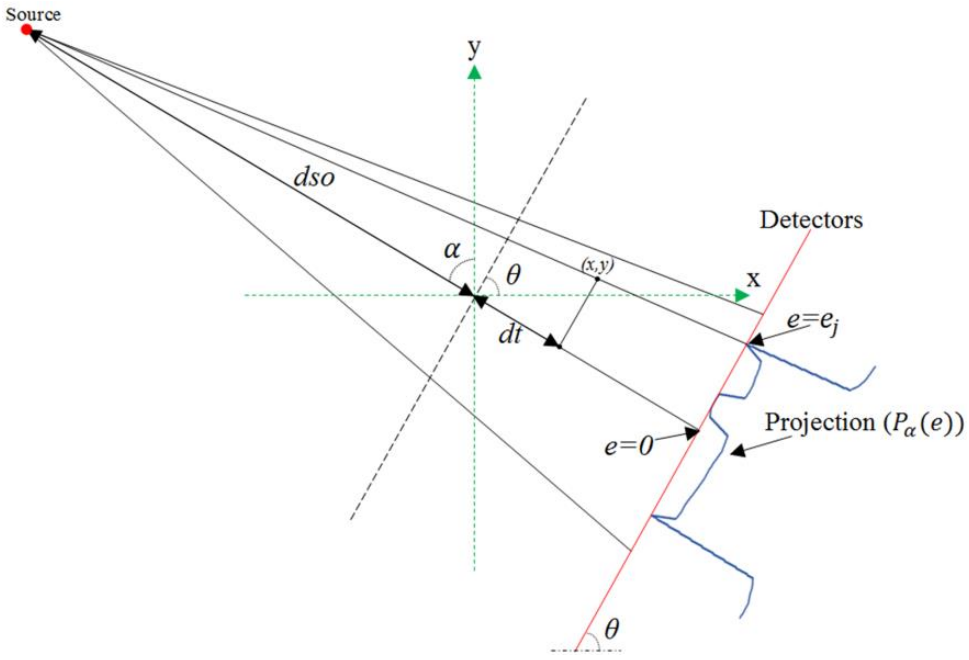

Figure 2.7 Geometry of the reconstruction

Two-dimensional CT projections are produced by rotating the container incrementally with a step of 5° about its central vertical axis between 0° and 180° .

2.1.4.1.2. CT reconstruction and imaging

To reconstruct 3D imagery, we use the filtered back-projection (FBP) [64]. The geometry and the parameters of the process are shown in Figure 2.7 and Table 2.3. The following steps summarize the method:

Assume that the projection for each slice $P_\alpha(e)$ is sampled with n sampling interval ($P_\alpha(kn)$), where $k = 0$ corresponds to the central ray passing through the rotation center origin. A slice in computed tomography is a 2D image of the section reconstructed from one circular scan that is from a single projection.

Convolve each modified projection with the filter $g(kn)$ to generate the corresponding filtered projection:

$$Q_{\alpha_i}(kn) = \left(P_{\alpha_i}(kn) \frac{dso}{\sqrt{dso^2 + (kn)^2}} \right) \otimes g(kn) \tag{59}$$

$$g(kn) = \begin{cases} \frac{1}{8n^2} & k = 0 \\ 0 & k = even \\ -\frac{1}{2(k\pi n)^2} & k = odd \end{cases} \tag{60},$$

where $\otimes$ is the convolution operator. The conventional ramp filter was used for filtering the reconstruction noise and image enhancement. Perform a weighted back-projection of each filtered projection along the corresponding fan. The reconstructed image is derived from the sum of all the back-projections:

$$(x, \mathrm{y}) = \Delta\alpha \sum_{i=1}^{M} \frac{1}{U^2(x,y,\alpha_i)} Q_{\alpha_i}(e) \tag{61}$$

$$U(x, y, \alpha_i) = \frac{dso+dt}{dso} \tag{62},$$

where U is defined for each pixel (x, y), the ratio of st $(dso + dt)$ to the source to rotation distance (dso). Note that st is the projection of the distance from the source to the pixel (x, y) on the central ray. The e is a ray that passes through (x, y) in the fan for the source located at the angle α_i.

Table 2.3 CT reconstruction parameters

Parameter	Value (cm)
Distance from source to rotation center (dso)	274
Distance from rotation center to detector (dod)	55
Height of detector	92
Width of detector	6
Detector pixel size (width × height)	2 × 0.92

2.1.4.2. Computed tomography application: sparse-view cone-beam neutron-photon computed tomography

In our previous section, we considered fan beam geometry and models with only few materials to investigate the possibility of combined neutron-photon computed tomography and its material discrimination ability using traditional filtered back-projection algorithm for reconstruction and the ratio of the radiation transmissions for material discrimination. In this section, we investigate the ability of the two-source system to precisely reconstruct 3D objects in the complex modelled scenes in a cone-beam geometry using our robust regularization formulation by combining regularization methods based on curvelet and TV. Then we study the material discrimination in the combined source tomography using a novel proposed material discrimination method. It uses 2D signatures calculated using both the ratios of transmissions under different sources and the neutron transmission through the object's space voxels.

2.1.4.2.1. Neutron-photon configuration

Figure 2.8 show the model of the cone beam neutron-photon radiography system. Isotropic point sources were used to produce cone beams of neutrons and photons incident on the object under scrutiny. Two target configurations were used, each consisting of an aluminum box with a set of objects placed inside. The source-to-detector array geometry was set to cover the container size used in the study that is 50 cm × 50cm × 50 cm container which is a regular unit load for air cargo. The size, shape and composition of the objects were varied to provide a range of scenarios. To generate the 2D radiographic projections, the box was rotated about the central vertical axis with angle step increments of 5°.

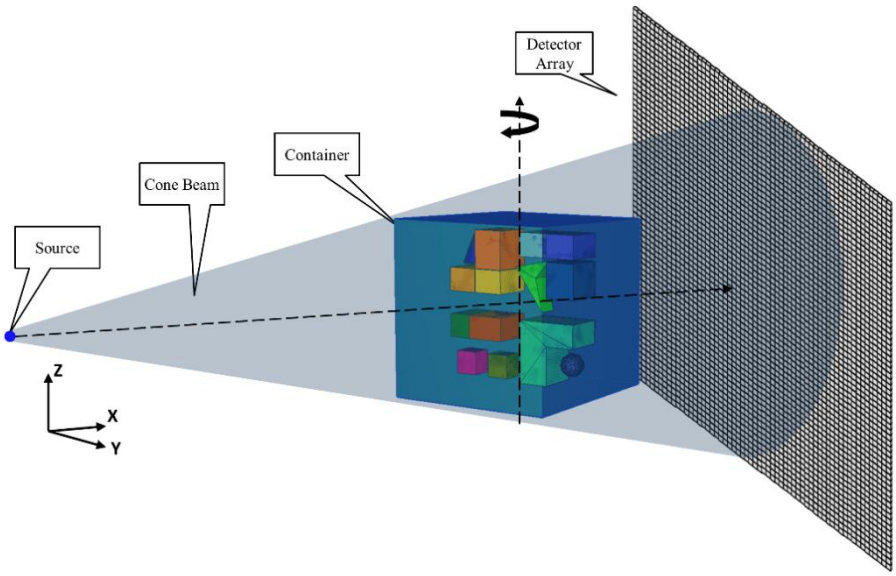

Figure 2.8 3D scheme of the neutron-photon system

Figure 2.9 depicts a schematic of the container contents for two models demonstrating shapes, orientation, and materials of the objects whose geometric properties are listed in Table 2.4 and Table 2.5. In two models, the target object is an aluminum container with exterior dimensions of 50 cm×50 cm×50 cm, and walls with a 3cm thickness. The distance from the source to the nearest surface of the container was 249 cm. The detector array was placed 30 cm away from the back wall of the container. Computations were performed using neutron and photon sources which were selected based on commercially available, state-of-the-art systems. For each model, the neutron source was defined with an initial energy of 2.5-MeV. Photon sources were defined with an initial energy of 6-MeV. The source-to-array geometry was set to cover the container of size of 50 cm × 50 cm × 50 cm to study the object reconstruction and material discrimination in an air freight container. If other object dimensions are of interest the geometry can be modified, accordingly. The detector array was defined for a 92 cm by 92 cm area (100 pixels horizontally by 100 pixels vertically).

Table 2.4 Model 1: geometry of objects inside container

(Number) Object	Dimensions (cm)
(1) Cone	6(Diameter) × 8(Height)
(2) L-shape	16(H1) × 16(W1) × 10(H2) × 8(W2) × 10(T)
(3) L-shape	16(H1) × 16(W1) × 10(H2) × 8(W2) × 10(T)
(4) Irregular Body	10.198 × 13.601 × 8.732 × 6.021
(5) Parallelepiped	6(L) × 6(W) × 10(T)
(6) Parallelepiped	10(L) × 6(W) × 10(T)
(7) Parallelepiped	6(W) × 6(W) × 5(T)
(8) Parallelepiped	6(W) × 6(W) × 5(T)
(9) L-shape	16(H1) × 16(W1) × 10(H2) × 8(W2) × 10(T)
(10) Sphere	6(Diameter)

The radiography tallies for both neutrons and photons were computed for a limited number of views. 36 projection views were taken for angles ranging from 0° to 180° using 5° increments. Model 1 was intended to illustrate the ability of tomographic reconstruction methods to represent simple shapes such as a sphere, cone, L-shape, and parallelepiped and to test the separation of high-Z and low-Z materials like lead, iron, and polyethylene. The container in Model 2 includes a wider selection of materials than that in the Model 1. Additionally, the 1-mm gaps were maintained between the parallel faces of objects 2, 3, 4, and the 1-cm gaps were introduced between the parallel faces of objects 5, 6, and 8. This was done to test the ability of the reconstruction technique to separate objects under sparse-view conditions.

Table 2.5 Model 2: geometry of objects inside container

(Number) Object	Dimensions (cm)
(1) Cone	6(Diameter) × 8(Height)
(2) Parallelepiped	8(L) × 9.9(W) × 10(T)
(3) Parallelepiped	7.9(L) ×6(W) × 10(T)
(4) Parallelepiped	8(L) × 6(W) × 10(T)
(5) Parallelepiped	7(L) × 6(W) × 10(T)
(6) Parallelepiped	8(L) × 6(W) × 10(T)
(7) Irregular Body	10.198 × 13.601 × 8.732 × 6.021
(8) Parallelepiped	8(L) × 9(W) × 10(T)
(9) Parallelepiped	6(L) × 6(W) × 10(T)
(10) Parallelepiped	10(L) × 6(W) × 10(T)
(11) Parallelepiped	6(L) × 6(W) × 5(T)
(12) Parallelepiped	6(L) × 6(W) × 5(T)
(13) L-shape	16(H1) × 16(W1) × 10(H2) × 8(W2) × 10(T)
(14) Sphere	6(Diameter)

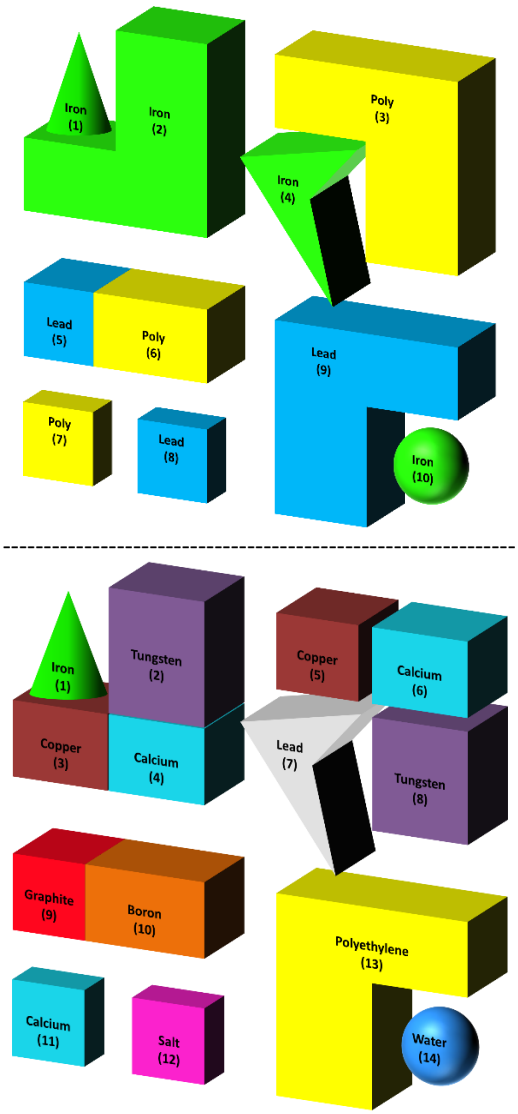

Figure 2.9 Configuration, shapes, and materials of objects placed inside the container; Top: Model 1; bottom: Model 2

2.1.4.2.2. CT reconstruction and imaging

2.1.4.2.2.1. Imaging

Two imaging models have been used in most of the neutron-photon system: noisy and noise-free. In the noise-free model, the problem can be defined as a linear equation:

$$A\mathrm{x} = b \tag{63}$$

where $b \in \mathbb{R}^N$ is the projection data, $\mathrm{x} \in \mathbb{R}^M$ is the reconstruction result, and $A \in \mathbb{R}^{N\times M}$ is the system geometry matrix, which model either neutron or photon transport in the tomography system. This inverse problem in Eq. (63) can be solved by minimizing f(x),

$$f(\mathrm{x}) = \|A\mathrm{x} - b\|_2^2 \tag{64}$$

using gradient descent method.

In the noisy model, the imaging problem is described by a linear system:

$$A\mathrm{x} + n = b \tag{65}$$

Assuming noise and the sparse-view scenario, the problem is severely ill-posed which makes it difficult to solve. Therefore, a different cost function with a regularization term has been considered.

$$\min_{\mathrm{x}} |\Phi(\mathrm{x})|_1 \quad subject\ to \quad \|b - A\mathrm{x}\|_2^2 \leq \sigma \tag{66}$$

where Φ is a "sparsifying" transformation which should be convex. The constrained optimization is similar to the following unconstrained optimization problem [7, 16]:

$$\min_{\mathrm{x}} \ |\Phi(\mathrm{x})|_1 + \lambda \ \|b - A\mathrm{x}\|_2^2 \tag{67}$$

where $\lambda > 0$ is a balancing constant depends on the sparsity of the underlying image x. Considering the problem of sparse-view computed tomography, we have the complete under-sampling for $N \ll M$, so a good regularization term in the reconstruction model will be necessary to yield a high-quality 3D reconstruction.

2.1.4.2.2.2. Regularization terms

TV, as a regularizer, is a best match for reconstructing signals which are piecewise constant or have low total variations throughout the image [65,66,67].

Total variation (TV)

The gradient operator (∇) is utilized as the sparsifying transform function ($\Phi(\mathrm{x})$).

$$\Phi(\mathrm{x}) = \sum \sqrt{(\nabla_x \mathrm{x})^2 + (\nabla_y \mathrm{x})^2 + (\nabla_z \mathrm{x})^2} \tag{68}$$

Wavelet regularizer (W)

Wavelet regularization has been considered as a regularizer for CT and generally for solving the inverse problems in [17,68,69]. Wavelet transform has a better directional sensitivity than TV, because it filters the local differences.

Here the discrete wavelet basis (ψ) is used as the sparsifying transform function (Φ).

$$\Phi(\mathrm{x}) = \sum_m \langle \mathrm{x}, \psi_m \rangle \tag{69}$$

where ψ_m is a discrete Daubechies wavelet basis at scale m which has been chosen experimentally to achieve the best result.

CTV

Unlike wavelets who are limited in representing directions, curvelets have a better sensitivity in that respect. They are also sparse in the sense of l_1-norm sparsity, and can be considered almost optimal non-adaptive sparse representation of objects with edges. Curvelets have been intensively used in various image and video processing applications, fluid mechanics, compressed sensing, and generally for solving inverse problems [55,57]. Thus, the curvelet transform suits for sparse-view CT reconstruction. We use the proposed in this work CTV formulated regularization model:

$$|\Phi(\mathrm{x})|_1 = \alpha_{TV}\left(|\nabla_x \mathrm{x}|_1 + \left|\nabla_y \mathrm{x}\right|_1 + |\nabla_z \mathrm{x}|_1\right) + \alpha_C(|C\mathrm{x}|_1) \tag{70}$$

where ∇ is the gradient operator, C is the curvelet transform and constants α_{TV} and α_C are the weights assigned for TV and curvelet terms, respectively.

CTV will be compared to TV and WT regularizers.

2.1.4.2.2.3. Solver

The constrained optimization problem can be solved using various methods as in [42,65,69,71]. The optimization problem (70) has both l_1 and l_2-norm terms thus makes it difficult to find a closed-form solution to the equation. The split Bregman method [54] is adopted in this paper due to its ease of implementation and iteration speed.

The constrained optimization problem Eq. (71):

$$\min_{x} |\Phi(\mathrm{x})|_1 \quad subject\ to \quad \|b - A\mathrm{x}\|_2^2 \leq \sigma \tag{71}$$

is solved by iterating over the following three update equations:

$$\mathrm{x}^{(i+1)} = \underset{\mathrm{x}}{argmin}\ \frac{\lambda}{2}\|b - A\mathrm{x}\|_2^2 + \frac{\mu}{2}\left\|d^{(i)} - \Phi(\mathrm{x}) - v^{(i)}\right\|_2^2 \tag{72}$$

$$d^{(i+1)} = \underset{\mathrm{x}}{argmin}\ |d|_1 + \frac{\mu}{2}\left\|d - \Phi(\mathrm{x}^{(i+1)}) - v^{(i)}\right\|_2^2 \tag{73}$$

$$v^{(i+1)} = v^{(i)} + (\Phi(\mathrm{x}^{(i+1)}) - d^{(i+1)}) \tag{74}$$

The increase of λ causes lesser regularization and the increase of μ causes more regularization and thus in the case of TV the results is expected to be smoothed. Two sub-problems of equations (72) and (73) are solved first. The sub-problem (72) should be precisely resolved, that requires roots of its derivatives (75):

$$A^{\dagger}(b - A\mathrm{x}) + \frac{\mu}{\lambda}\Phi^{\dagger}\left(d^{(i)} - \Phi(\mathrm{x}) - v^{(i)}\right) = 0 \tag{75}$$

This can be rewritten as:

$$\left(A^{\dagger}A + \frac{\mu}{\lambda}\Phi^{\dagger}\Phi\right)\mathrm{x} = A^{\dagger}b + \frac{\mu}{\lambda}\Phi^{\dagger}\left(d^{(i)} - v^{(i)}\right) \tag{76}$$

where $\Phi^{\dagger}, A^{\dagger}$ are the backward sparsifying transformation and the back projector, respectively. However, the normal inversion cannot be obtained, because $\Phi^{\dagger}\Phi \neq I$ and A is not a square matrix, so the conjugate gradient method [58] was chosen as a solution for Eq. (76). The solution for d in Eq. (73), is found using a shrinkage operator as follows:

$$d^{(i+1)} = shrink\left(\Phi(\mathrm{x}) + v^{(i)}, \frac{1}{\mu}\right) \tag{77}$$

where

$$shrink\,(k, t\,) = \frac{k}{|k|}\,max(|k| - t, 0) \tag{78}$$

Where t is the shrinkage threshold and k is each of the coefficients for the point-wise shrinkage operator.

2.2. Compressed Sensing MRI Methods

In this section, three proposed compressed sensing MRI methods including CT-TGV, CS-NLTV, and SS-NLTV are explained.

2.2.1. Compressed Sensing MRI Using Curvelet Transform and Total Generalized Variation (CT-TGV)

In this section, we introduce a novel compressed sensing MRI method, CT-TGV that exploits adaptively curvelet transform (CT) and total generalized variation (TGV) regulaizers. The curvelet transform is optimal sparsifying transform with excellent directional sensitivity than that of wavelet transform. The TGV, on the other hand, is based on second order derivatives and can selectively regularize at different regularity levels. We have used a novel approach of combining alternating direction method of multiplier (ADMM), adaptive weighting, and splitting variables technique to solve the formulated optimization problem.

CT-TGV method

Magnetic resonance imaging (MRI) model can be defined as follows

$$A\mathrm{x} = b \tag{79},$$

where $x \in \mathbb{R}^M$ is a MR image, $A \in \mathbb{R}^{N \times M}$ is a measurement matrix with $N \ll M$, and $b \in \mathbb{R}^N$ is the observed data. The MR data can be restored by solving the minimization problem

$$minimize\, J(x) \quad subject\ to \quad Ax = b \tag{80},$$

$$when\, J(x) = |\Phi(x)|_1 \tag{81}.$$

Here Φ is a sparsifying transform and $J(x)$ is regularizing functional. In the compressed sensing/compressive sampling (CS) model of MRI, $A = SF$, where S is a selection or sampling matrix, F is 2D discrete Fourier matrix, and b is the observed k-space data. Assuming the sparsity of the model, the problem is ill-posed for minimizing the least-squares function. Therefore, the following cost function with a regularization term has been considered.

$$\min_x |\Phi(x)|_1 \text{ subject to } \quad \|Ax - b\|_2^2 \leq \sigma \tag{82},$$

where σ is the variance of noise in b.

The constrained optimization in Eq. (80) is similar to the following unconstrained optimization problem [54]:

$$\min_x |\Phi(x)|_1 + \frac{\lambda}{2} \|Ax - b\|_2^2 \tag{83},$$

where $\lambda > 0$ is a balancing constant which count on the sparsity of the underlying MR image x under linear transformation.

Considering the problem, we propose and formulate the optimization problem using a combination of both TGV and curvelet regularizers. The proposed optimization problem to reconstruct $\hat{\mathrm{x}}$:

$$\hat{\mathrm{x}} = \underset{\mathrm{x}}{argmin} \;\; \alpha|TGV(\mathrm{x})|_1 + \beta\,|Curv(\mathrm{x})|_1 + \frac{\lambda}{2}\,\|A\mathrm{x} - b\|_2^2 \qquad (84),$$

where TGV is the total generalized variation operator and $Curv(\mathrm{x})$ is the combination of different subbands of curvelet transform. α and β are the weighting parameters stressing each of two regularization terms. The value of these two parameters in each loop are adaptively derived based on the variance of noise present in reconstructed image from the previous iteration. We stress more on the curvelet regulaizer term if the estimated variance in each curvelet subband is greater than our specified threshold. The variances of the signal in each curvelet subband, σ_{ij}^2 ,are calculated by utilizing the maximum likelihood estimator applied on all the coefficients in a square neighboring area.

2.2.1.1. Total generalized variation – TGV

Total generalized variation has been introduced to overcome oil painting effects that appears when the total variation (TV) process is used [72]. TV, which is based on the first order derivatives works well on the images with piecewise constant intensities. Since TGV considers the second or a higher order derivatives, it has a potential for preventing the oil painting effects and produce sharp edges or, generally, piecewise polynomial intensities.

Based on the experiments, the third and higher orders total generalized variation are comparable to the second order and they are computationally very intensive. Therefore, TGV with the second order derivatives have been considered as a good alternative [72,73,74].

Fig. 13 depicts the comparison of TV vs TGV (2nd order) reconstruction from a noisy MRI image. The close ups of selected region display that the reconstruction from total generalized variation leads to sharper edge and prevents oil painting effect compared to total variation result. The plots on the right in Figure 2.10 show the edge profile.

The second order TGV regularization can be defined as ℓ_1 optimization term:

$$\min_{\mathrm{x}} \alpha|TGV(\mathrm{x})|_1 = \min_{D\mathrm{x}=g+r} \alpha_1|g|_1^{(2,M)} + \alpha_2|Er|_1^{(3,M)} \tag{85}$$

Where $g, r \in \mathbb{R}^2$ are two introduced auxiliary variables showing differentiated values, $D\mathrm{x} = g + r$ and $|t|_1^{(p,M)} = \sum_{n=1}^{M}\sum_{m=0}^{p-1}\left|t_{n+mp}\right|$.

$$D = \begin{pmatrix} D_h \\ D_v \end{pmatrix}, \tag{86}$$

$$E^T = \begin{pmatrix} D_h & D_v & 0 \\ 0 & D_h & D_v \end{pmatrix}, \tag{87}$$

where D_h , $D_v \in \mathbb{R}^{M \times M}$ are horizontal and vertical differential filter matrices.

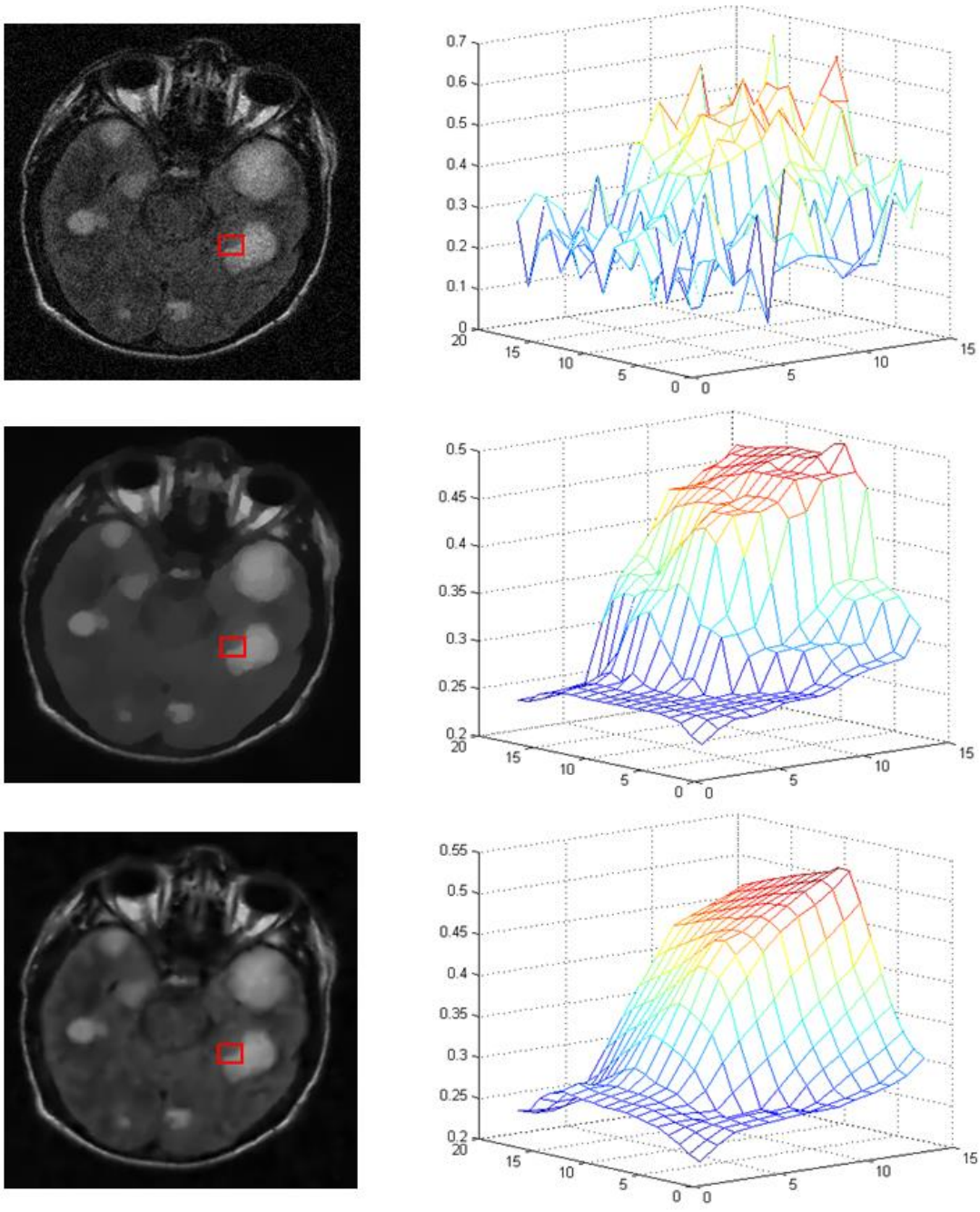

Figure 2.10 1st column: Top: Noisy MRI image, Middle: reconstruction using TV, Bottom: reconstruction using TGV; 2nd column: Edge profile for respective images

2.2.1.2. Curvelet transform

Curvelet transform proposed by Candes [75,76] is an efficient geometric multiscale sparsifying transform. Unlike wavelets, curvelets have directional sensitivity and anisotropy, optimal sparse representation, better ℓ_1-norm sparsity, and thus, they can efficiently characterize anisotropic features such as edges, arcs and curves. Curvelet transform has been used for image denoising, feature extraction and for solving the inverse problem [55,57,70] generally.

The curvelets at scale 2^{-j}, orientation θ_l, and position $k = (k_1, k_2)$ are defined as

$$\varphi_{j,l,k}(x) = \varphi_j(R_{\theta_J}(x - \rho_k^{(j,l)})) \quad (88),$$

where φ_j is a "mother" curvelet, $\theta_J = 2\pi \cdot 2^{-\lfloor j/2 \rfloor} \cdot l$, $J = (j, l)$ indicating the scale/angle, and

$$\rho_k^{(j,l)} = R_{\theta_J}^{-1}(k_1 \cdot 2^{-j}, k_2 \cdot 2^{-j/2}). \quad (89)$$

$$R_\theta = \begin{pmatrix} \cos(\theta) & sin(\theta) \\ -\sin(\theta) & \cos(\theta) \end{pmatrix}, \; R_\theta^{-1} = R_\theta^{\mathrm{T}} = R_{-\theta} \quad (90)$$

The curvelet transform of function x is computed as

$$C_{\varphi}(x)(j,l,k) = \langle x, \varphi_{j,l,k} \rangle \tag{91}$$

The whole process can be performed in the frequency domain, by introducing 2D frequency window as

$$U_j(\omega) = 2^{-\frac{3j}{4}} W(2^{-j}|\omega|) V(\frac{2^{\lfloor j/2 \rfloor}\theta}{2\pi}) \tag{92},$$

where W is the Meyer wavelet window dividing the frequency domain into annuli $|x| \in [2^j, 2^{j+1})$, and V is the angular window dividing the annuli into wedges θ_J. Then the curvelets can be defined in frequency domain as

$$\varphi_{j,l,k}(\omega) = U_J(R_{\theta_J}\omega) e^{-i\langle \rho_k^{(j,l)}, \omega \rangle} \tag{93}$$

In practical implementations, discrete curvelet transform tiling in the frequency plane is based on concentric squares and shears in Cartesian coronae as represented in Figure 2.11. Due to the advantages of curvelets as sparsifiers with their detail representation properties, the transform is adopted for implementation in our method. We can implement k-th subband of curvelet transform (C_k) as a mask in the frequency domain (Z_k) [54].

$$C_k(\mathrm{x}) = F^{*}\mathrm{diag}\big(\mathrm{vec}(Z_k)\big)F.\mathrm{x} = P_k.\mathrm{x} \tag{94}$$

where F is the vectorized form of the discrete Fourier transform operator.

Therefore, the curvelet regularization can be defined as ℓ_1 optimization term:

$$\min_{\mathrm{x}} \ |Curv(\mathrm{x})|_1 \ = \ \min_{\mathrm{x}} \ \beta \sum_k |P_k.\mathrm{x}|_1 = \min_{\mathrm{x}} \beta \sum_k |C_k(\mathrm{x})|_1 \tag{95}$$

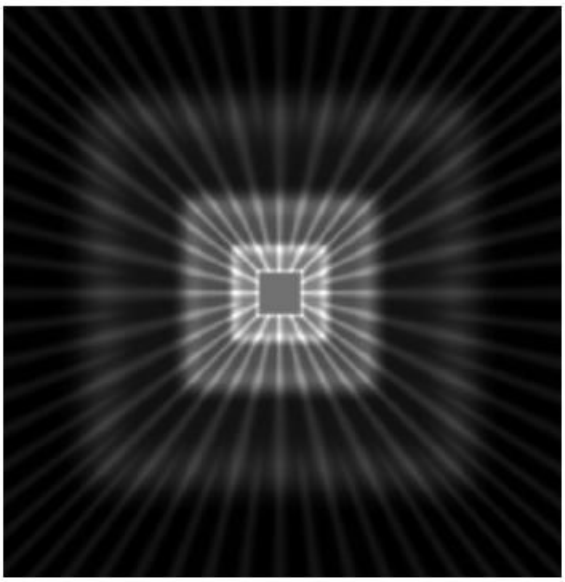

Figure 2.11 Tiling of discrete curvelet transform in the frequency plane

2.2.1.3. Solution

The proposed optimization problem is formulated as follows:

$$\underset{\mathrm{x},r}{argmin}\ \alpha_1|g|_1^{(2,M)} + \alpha_2|Er|_1^{(3,M)} + \beta\sum_k|C_k(\mathrm{x})|_1 + \frac{\lambda}{2}\|Ax-b\|_2^2 \quad (96).$$

The proposed formulation has both l_1 and l_2-norm terms and thus the solution in a closed-form is difficult to obtain. The alternating direction method of multiplier (ADMM) [60] and splitting variables are used to solve the formulated problem as follows:

$$\underset{\mathrm{x},r}{argmin}\ \alpha_1|y_1|_1^{(2,M)} + \alpha_2|y_2|_1^{(3,M)} + \beta\sum_k|y_3(k)|_1 + \frac{\lambda}{2}\|Ax-b\|_2^2 \quad (97)$$

subject to $\quad y_1 = D\mathrm{x} - r,\ \ y_2 = Er,\ \ \ y_3(k) = C_k(\mathrm{x}),$

where $y_1 \in \mathbb{R}^{2M}$, $y_2 \in \mathbb{R}^{3M}$, and $y_3(k) \in \mathbb{R}^M$ are auxiliary variables. The Lagrangian function for the problem can be written as

$$\mathcal{L}(x, r, y_1, y_2, y_3, u_1, u_2, u_3) = \quad (98)$$

$$= \frac{\lambda}{2}\|A\mathrm{x}-b\|_2^2 + \alpha_1|y_1|_1^{(2,M)} + \frac{\mu}{2}\|D\mathrm{x}-r-y_1+u_1\|_2^2 + \alpha_2|y_2|_1^{(3,M)}$$

$$+ \frac{\eta}{2}\|Er-y_2+u_2\|_2^2 + \beta\sum_k|y_3(k)|_1 + \frac{\Gamma}{2}\sum_k\|C_k(\mathrm{x})-y_3(k)+u_3(k)\|_2^2$$

where $u_1 \in \mathbb{R}^{2M}$, $u_2 \in \mathbb{R}^{3M}$, and $u_3(k) \in \mathbb{R}^{M}$ are the newly defined scaled dual variables.

Finally, the problem is solved by iterating over the following equations (99-105):

$$\{\mathrm{x}^{(n+1)}, r^{(n+1)}\} \coloneqq \underset{\mathrm{x},r}{argmin}\ \mathcal{L}\left(x, r, y_1^{(n)}, y_2^{(n)}, y_3^{(n)}, u_1^{(n)}, u_2^{(n)}, u_3^{(n)}\right) \quad (99),$$

$$y_1^{(n+1)} \coloneqq \underset{y_1}{argmin}\ \mathcal{L}\left(\mathrm{x}^{(n+1)}, r^{(n+1)}, y_1, u_1^{(n)}\right) \quad (100),$$

$$y_2^{(n+1)} \coloneqq \underset{y_2}{argmin}\ \mathcal{L}\left(\mathrm{x}^{(n+1)}, r^{(n+1)}, y_2, u_2^{(n)}\right) \quad (101),$$

$$y_3^{(n+1)} \coloneqq \underset{y_3}{argmin}\ \mathcal{L}\left(\mathrm{x}^{(n+1)}, y_3, u_3^{(n)}\right) \quad (102),$$

$$u_1^{(n+1)} \coloneqq u_1^{(n)} + \left(D\mathrm{x}^{(n+1)} - r^{(n+1)} - y_1^{(n+1)}\right) \quad (103),$$

$$u_2^{(n+1)} \coloneqq u_2^{(n)} + \left(Er^{(n+1)} - y_2^{(n+1)}\right) \quad (104),$$

$$u_3^{(n+1)} \coloneqq u_3^{(n)} + \left(C(\mathrm{x}^{(n+1)}) - y_3^{(n+1)}\right) \quad (105).$$

The minimization solutions for Eq. (100-102) can be found using shrinkage operators below:

$$y_1^{(n+1)} \coloneqq Shrink_1\left(D\mathrm{x}^{(n+1)} - r^{(n+1)} + u_1^{(n)}, \vartheta_1\right) \quad (106)$$

$$y_2^{(n+1)} \coloneqq Shrink_1\left(Gr^{(n+1)} + u_2^{(n)}, \vartheta_2\right) \tag{107}$$

$$y_3^{(n+1)} \coloneqq Shrink_2\left(C(\mathrm{x}^{(n+1)}) + u_3^{(n)}, \vartheta_3\right) \tag{108}$$

where $\vartheta_1 = \frac{\alpha_1}{\mu}$, $\vartheta_2 = \frac{\alpha_2}{\eta}$, $\vartheta_3 = \frac{\beta}{\Gamma}$ and

$$Shrink_1(x,\xi)_n = x_n \,.\, max\left\{1 - \xi\left(\sum_{m=0}^{p-1}|x_{n+mp}|\right)^{-1}, 0\right\} \tag{109}$$

$$Shrink_2(x,\xi)_n = sign(x_n).max\{|x_n| - \xi, 0\} \tag{110}$$

The solution for the sub-problem Eq. (99), requires finding the roots of its derivatives which leads to the following:

$$\begin{pmatrix} \lambda A^T A + \mu D^T D + \Gamma \sum_k P_k^* P_k & -\mu D^T \\ -\mu D & \mu I_{2M} + \eta E^T E \end{pmatrix} \begin{pmatrix} \mathrm{x} \\ r \end{pmatrix} =$$

$$\begin{pmatrix} \lambda A^T b + \mu D^T (y_1 - u_1) + \Gamma \sum_k P_k^* (y_3(k) - u_3(k)) \\ -\mu(y_1 - u_1) + \eta E^T (y_2 - u_2) \end{pmatrix} \tag{111}$$

Additionally,

$$D^T D = D_h^T D_h + D_v^T D_v = \Delta \quad (112),$$

$$E^T E = \begin{pmatrix} \Delta & D_v D_h^T \\ D_h D_v^T & \Delta \end{pmatrix} \quad (113),$$

where Δ, is the Laplacian filter matrix, and as a final step, the vectorized data is divided into the blocks of data:

$$r \coloneqq [r_h^T, r_v^T]^T,\ y_1 \coloneqq [y_{1h}^T, y_{1v}^T]^T, u_1 \coloneqq [u_{1h}^T, u_{1v}^T]^T,$$

$$y_2 \coloneqq [y_{2h}^T, y_{2d}^T, y_{2v}^T]^T,\ u_2 \coloneqq [u_{2h}^T, u_{2d}^T, u_{2v}^T]^T \quad (114),$$

We form the solution as:

$$\begin{pmatrix} \lambda A^T A + \mu\Delta + \Gamma \sum_k P_k^* P_k & -\mu D_h^T & -\mu D_v^T \\ -\mu D_h & \mu I_M + \eta\Delta & \eta D_v D_h^T \\ -\mu D_v & \eta D_h D_v^T & \mu I_M + \eta\Delta \end{pmatrix} \begin{pmatrix} \mathrm{x} \\ r_h \\ r_v \end{pmatrix} = \quad (115)$$

$$\begin{pmatrix} \lambda A^T b + \mu D_h^T (y_{1h} - u_{1h}) + \mu D_v^T (y_{1v} - u_{1v}) + \Gamma \sum_k P_k^* (y_3(k) - u_3(k)) \\ -\mu(y_{1h} - u_{1h}) + \eta D_h (y_{2h} - u_{2h}) + \eta D_v (y_{2d} - u_{2d}) \\ -\mu(y_{1v} - u_{1v}) + \eta D_h (y_{2d} - u_{2d}) + \eta D_v (y_{2v} - u_{2v}) \end{pmatrix}$$

2.2.2. Compressed sensing MRI using curvelet sparsity and nonlocal total variation: CS-NLTV

In this section, we introduce a novel CSMRI method, called CS-NLTV that exploits curvelet sparsity (CS) and nonlocal total variation (NLTV) regularization. The curvelet transform is optimal sparsifying transform with the excellent directional sensitivity than that of wavelet transform. The NLTV, on the other hand extends the total variation regularizer to a nonlocal variant which can preserve both textures and structures and produce sharper images. We have explored a new approach of combining alternating direction method of multiplier (ADMM), adaptive weighting, and splitting variables technique to solve the formulated optimization problem.

CS-NLTV

Considering the CSMRI problem defined in section 2.2.1, we propose and formulate the optimization problem using a combination of both the nonlocal total variation and the curvelet as regularizers. The proposed optimization problem to obtain reconstruction $\hat{\mathrm{x}}$ as follows:

$$\hat{\mathrm{x}} = \underset{\mathrm{x}}{argmin}\ \alpha|\nabla_w \mathrm{x}|_1 + \beta \sum_k |C_k(\mathrm{x})|_1 + \frac{\lambda}{2}\ \|A\mathrm{x} - b\|_2^2 \qquad (116).$$

where $|\nabla_w \mathrm{x}|_1 = \sum_t |\nabla_w \mathrm{x}_t|_1$ is the nonlocal total variation norm and nonlocal weights w are computed from image estimate $\hat{\mathrm{x}}$. $C(\mathrm{x})$ is the combination of different subbands of curvelet

transform. α and β are the weighting parameters stressing two regularization terms. The value of these two parameters in each loop, are adaptively derived based on the variance of noise present in reconstructed image from previous iteration. We stress more on the curvelet regulaizer term if the estimated variance in each curvelet subband is greater than a specified threshold. The variances of the signal in every curvelet subband are computed by exploiting the maximum likelihood estimator applied on the neighborhood (a square) areas of coefficients.

2.2.2.1. Nonlocal total variation – NLTV

Nonlocal total variation (NLTV) is defined to describe the patch-level correspondence in contrast to the total variation (TV) which is based on the correspondence at the pixel-level [54]. For image x, the nonlocal weights can be formed concerning any two spatial nodes i and j,

$$\varpi_{\mathrm{x}}(i,j) = e^{-\frac{\int_{\mathcal{R}_1} G_\sigma(t)(\mathrm{x}(j+t)-\mathrm{x}(i+t))^2 dt}{\sigma^2}} \quad (117),$$

where G is a Gaussian kernel with the variance σ^2; and $\mathcal{R}_1$ characterizes the spatial neighborhood around i and j for similarity consideration. The nonlocal gradient $\nabla_w \mathrm{x}(i,j)$ at i is described as a vector of all partial derivatives $\nabla_w \mathrm{x}(i,.)$ [72]:

$$\nabla_w \mathrm{x}(i,j) = \big(\mathrm{x}(j) - \mathrm{x}(i)\big)\sqrt{\varpi_{\mathrm{x}}(i,j)}\,, \quad \forall j \in \mathcal{R}_2 \quad (118),$$

where $\mathcal{R}_2$ is the spatial neighborhood around i , whose nonlocal gradient $\nabla_w \mathrm{x}(i,j)$ is calculated. The adjoint of Eq. (118) is derived from the adjoint relationship with a nonlocal divergence operator $\mathrm{div_w}$ as:

$$\langle \nabla_w \mathrm{x}\,, v\rangle = \langle \mathrm{x}\,, \mathrm{div}_w v\rangle \tag{119}$$

$$\mathrm{div}_w v(i,j) = \int_{\mathcal{R}_2} \big(v(i,j) - v(j,i)\big)\sqrt{\varpi_{\mathrm{x}}(i,j)}\, dj \tag{120}.$$

Given the image $\mathrm{x} \in \mathbb{R}^M = \mathbb{R}^{m\times n}$ with $\mathcal{R}_1 = \mathbb{R}^{(2a_1+1)(2b_1+1)}$, $\mathcal{R}_2 = \mathbb{R}^{(2a_2+1)(2b_2+1)}$, nonlocal total variation weights are defined as

$$\varpi_{\mathrm{x}}(k_1,l_1,k_2,l_2) = e^{-\frac{\sum_{z_1=0}^{2a_1}\sum_{z_2=0}^{2b_1} G_\sigma(z_1,z_2)(\mathrm{x}(k_1-a_1+z_1,l_1-b_1+z_2)-\mathrm{x}(k_2-a_1+z_1,l_2-b_1+z_2))^2}{\sigma^2}}$$

$$k_1,k_2 = 1,\dots,m.\;\; l_1,l_2 = 1,\dots,n. \tag{121}.$$

Therefore, nonlocal gradient $\nabla_w \mathrm{x} \in \mathbb{R}^{m\times n\times(2a_2+1)\times(2b_2+1)}$ is as follows:

$$\nabla_w \mathrm{x}(k_1,l_1,:,:) =$$

$$\begin{bmatrix} (\mathrm{x}(k_1-a_2,l_1-b_2)-\mathrm{x}(k_1,l_1))\sqrt{\varpi_{\mathrm{x}}(k_1-a_2,l_1-b_2,k_1,l_1)} & \dots & (\mathrm{x}(k_1-a_2,l_1+b_2)-\mathrm{x}(k_1,l_1))\sqrt{\varpi_{\mathrm{x}}(k_1-a_2,l_1+b_2,k_1,l_1)} \\ (\mathrm{x}(k_1-a_2+1,l_1-b_2)-\mathrm{x}(k_1,l_1))\sqrt{\varpi_{\mathrm{x}}(k_1-a_2+1,l_1-b_2,k_1,l_1)} & \vdots & (\mathrm{x}(k_1-a_2+1,l_1+b_2)-\mathrm{x}(k_1,l_1))\sqrt{\varpi_{\mathrm{x}}(k_1-a_2+1,l_1+b_2,k_1,l_1)} \\ \dots & \dots & \dots \\ (\mathrm{x}(k_1+a_2,l_1-b_2)-\mathrm{x}(k_1,l_1))\sqrt{\varpi_{\mathrm{x}}(k_1+a_2,l_1-b_2,k_1,l_1)} & \dots & (\mathrm{x}(k_1+a_2,l_1+b_2)-\mathrm{x}(k_1,l_1))\sqrt{\varpi_{\mathrm{x}}(k_1+a_2,l_1+b_2,k_1,l_1)} \end{bmatrix} \tag{122},$$

where $\nabla_w \mathrm{x}(k_1, l_1, :, :)$ is a 2D submatrix acquired by stacking the third and fourth dimensions of $\nabla_w \mathrm{x}$ at $k_1 th$ location in the first and $l_1 th$ location in the second dimension. Figure 2.12 depicts the comparison of TV vs NLTV reconstruction from a noisy MRI image.

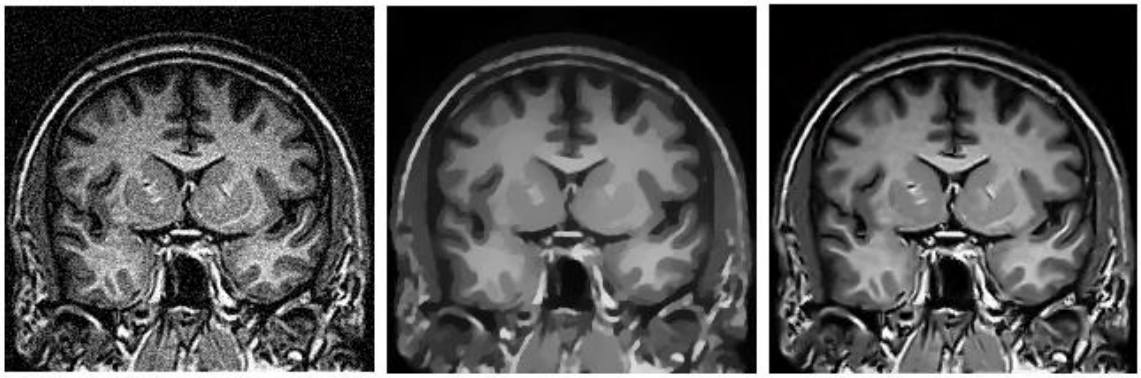

Figure 2.12 Left: Noisy MRI image, middle: recovered using TV, right: recovered using NLTV for respective image

2.2.2.2. Solution

Considering the k-th subband of curvelet transform (C_k) defined in section 2.2.1.2 as a mask in the frequency domain:

$$C_k(\mathrm{x}) = F^* \mathrm{diag}\big(\mathrm{vec}(Z_k)\big) F.\mathrm{x} = P_k.\mathrm{x} \quad (123),$$

The proposed optimization problem has both l_1 and l_2-norm terms and thus the solution in a closed-form is difficult to obtain. The alternating direction method of multiplier (ADMM) [60] and splitting variables are used to solve the formulated problem as follows:

$$\underset{\mathrm{x}}{argmin}\ \alpha|y_1|_1 + \beta \sum_k |y_2(k)|_1 + \frac{\lambda}{2}\ \|A\mathrm{x} - b\|_2^2 \tag{124}$$

$$\text{subject to} \qquad y_1 = \nabla_w \mathrm{x},\ \ y_2(k) = \ C_k(\mathrm{x}),$$

where $y_1 \in \mathbb{R}^M$, and $y_2(k) \in \mathbb{R}^M$ are auxiliary variables. The Lagrangian function for the problem can be written as below:

$$\mathcal{L}(x, y_1, y_2, u_1, u_2) = \tag{125}$$

$$= \frac{\lambda}{2}\ \|A\mathrm{x} - b\|_2^2 + \alpha|y_1|_1 + \frac{\eta}{2}\ \|\nabla_w \mathrm{x} - y_1 + u_1\|_2^2 + \beta \sum_k |y_2(k)|_1$$

$$+ \frac{\Gamma}{2} \sum_k \|C_k(\mathrm{x}) - y_2(k) + u_2(k)\|_2^2$$

where $u_1 \in \mathbb{R}^M$ and $u_2(k) \in \mathbb{R}^M$ are the newly defined scaled dual variables. Finally, the problem is solved by iterating over equations (126-130):

$$\mathrm{x}^{(n+1)} \coloneqq \underset{\mathrm{x}}{argmin}\ \mathcal{L}\left(\mathrm{x}, y_1^{(n)}, y_2^{(n)}, u_1^{(n)}, u_2^{(n)}\right) \quad (126),$$

$$y_1^{(n+1)} \coloneqq \underset{y_1}{argmin}\ \mathcal{L}\left(\mathrm{x}^{(n+1)}, y_1, u_1^{(n)}\right) \quad (127),$$

$$y_2^{(n+1)} \coloneqq \underset{y_2}{argmin}\ \mathcal{L}\left(\mathrm{x}^{(n+1)}, y_2, u_2^{(n)}\right) \quad (128),$$

$$u_1^{(n+1)} \coloneqq u_1^{(n)} + \left(\nabla_w \mathrm{x}^{(n+1)} - y_1^{(n+1)}\right) \quad (129),$$

$$u_2^{(n+1)} \coloneqq u_2^{(n)} + \left(C(\mathrm{x}^{(n+1)}) - y_2^{(n+1)}\right) \quad (130).$$

The optimal solution for the sub-problem by Eq. (126) requires finding roots of its derivatives that leads to Eq. (131):

$$\lambda A^T A\mathrm{x} - \lambda A^T b + \eta\ \mathrm{div_w}(\nabla_w \mathrm{x} - y_1 + u_1) + \Gamma\left(\sum_k P_k^* P_k\ \mathrm{x} + \sum_k\ P_k^*\left(y_2(k) - u_2(k)\right)\right) = 0 \quad (131).$$

Minimization in Eq. (127) and Eq. (128) can be attained by shrinkage operators such as:

$$y_1^{(n+1)} \coloneqq Shrink\left(\nabla_w \mathrm{x}^{(n+1)} + u_1^{(n)}, \vartheta_2\right) \quad (132)$$

$$y_2^{(n+1)} \coloneqq Shrink\left(C(\mathrm{x}^{(n+1)}) + u_2^{(n)}, \vartheta_2\right) \quad (133),$$

where $\vartheta_1 = \frac{\alpha}{\eta}$, $\vartheta_2 = \frac{\beta}{\Gamma}$ and

$$Shrink(x, \xi)_n = sign(x_n).max\{|x_n| - \xi, 0\} \quad (134).$$

2.2.3. Compressed sensing MRI based on shearlet sparsity and nonlocal total variation: SS-NLTV

In this section, we introduce a novel CSMRI method, called SS-NLTV that exploits shearlet sparsity (SS) and nonlocal total variation (NLTV) regularization. The shearlet transform is an optimal sparsifying transform with excellent directional sensitivity compared to that by wavelet transform. The NLTV, on the other hand extends the total variation regularizer to a nonlocal variant which can preserve both textures and structures and produce sharper images. We have explored a new approach of combining alternating direction method of multipliers (ADMM), splitting variables technique, and adaptive weighting to solve the formulated optimization problem.

SS-NLTV

Considering the CSMRI problem defined in section 2.2.1, we propose and formulate the optimization problem wherein the nonlocal total variation and the shearlets are used concurrently for regularization. The proposed optimization problem to obtain reconstruction $\hat{\mathrm{x}}$ as follows:

$$\hat{\mathrm{x}} = \underset{\mathrm{x}}{argmin}\ \alpha|\nabla_w \mathrm{x}|_1 + \beta \sum_k |SH_k(\mathrm{x})|_1 + \frac{\lambda}{2}\ \|A\mathrm{x} - b\|_2^2 \qquad (135).$$

where $|\nabla_w \mathrm{x}|_1 = \sum_t |\nabla_w \mathrm{x}_t|_1$ is the nonlocal total variation norm and nonlocal weights w are computed from image estimate $\hat{\mathrm{x}}$. $SH(\mathrm{x})$ is the combination of different subbands of shearlet

transform. α and β are the weighting parameters stressing two regularization terms. The value of these two parameters in each loop, are adaptively derived based on the variance of noise present in reconstructed image from previous iteration. We stress more on the shearlet regulaizer term if the estimated variance in each shearlet subband is greater than a specified threshold. The variances of the signal in every shearlet subband are computed by exploiting the maximum likelihood estimator applied on the neighborhood (a square) areas of coefficients.

2.2.3.1. Shearlet sparsity

Shearlet transform is introduced and generally has been used for solving the inverse problems [42,77]. Let $\psi_{a,s,t}$ be shearlet basis functions, i.e., shearlets. For continuous case, shearlet transformation of image f is modeled as

$$SH_{a,s,t}(x) = \int_{\mathcal{R}^2} f(x)\, \psi_{a,s,t}(t-x)dx \quad (136),$$

where $s \in \mathcal{R}$, $a \in \mathcal{R}$, and $t \in \mathcal{R}^2$ are orientation, scale, and location parameters, respectively and $f(x) \in \mathcal{R}^2$ is a two-dimensional reconstructed image. Shearlets are defined by dilating, shearing and translating $\psi_{a,s,t} \in \mathcal{R}^2$, as presented below:

$$\psi_{a,s,t}(x) = \left|detK_{a,s}\right|^{-\frac{1}{2}} \psi\left(K_{a,s}^{-1}(x-t)\right), \quad (137)$$

$$K_{a,s} = \begin{pmatrix} a & \sqrt{a}s \\ 0 & \sqrt{a} \end{pmatrix} \tag{138}$$

Assume l be a function describing piecewise smooth images $l \in C^2(\mathbb{R}^2)$ and l_{SH_p} be the shearlet approximation of l obtained by taking the p largest absolute shearlet coefficients, then

$$\left\| l - l_p \right\|_2 \leq Cp^{-2}(\log p)^3 \tag{139}$$

as $p \to \infty$, while the asymptotic error is Cp^{-1} for wavelet. Consequently, shearlet transform is better in sparsely approximating piecewise smooth images. We can implement k-th subband of shearlet transform (SH_k) as a mask Z_k in the frequency domain [54].

$$SH_k(\mathrm{x}) = F^* \mathrm{diag}\big(\mathrm{vec}(Z_k)\big) F.\mathrm{x} = P_k.\mathrm{x} \tag{140}$$

2.2.3.2. Solution

Considering the nonlocal TV term $|\nabla_w \mathrm{x}|_1$ defined in section 2.2.2.1, the proposed problem is formulated as follows:

$$\underset{\mathrm{x}}{argmin}\ \alpha|\nabla_w \mathrm{x}|_1 + \beta \sum_k |SH_k(\mathrm{x})|_1 + \frac{\lambda}{2}\ \|A\mathrm{x} - b\|_2^2 \tag{141}$$

The optimization problem has both l_1 and l_2-norm terms and thus the solution in a closed-form is difficult to obtain. The alternating direction method of multiplier (ADMM) [60] and splitting variables are used to solve the formulated problem as follows:

$$\underset{\mathrm{x}}{argmin}\ \alpha|y_1|_1 + \beta \sum_k |y_2(k)|_1 + \frac{\lambda}{2}\ \|A\mathrm{x} - b\|_2^2 \tag{142}$$

subject to $\quad y_1 = \nabla_w \mathrm{x},\ \ y_2(k) = SH_k(\mathrm{x}),$

where $y_1 \in \mathbb{R}^M$, and $y_2(k) \in \mathbb{R}^M$ are auxiliary variables. The Lagrangian function for the problem can be written as below:

$$\mathcal{L}(x, y_1, y_2, u_1, u_2) = \tag{143}$$

$$= \frac{\lambda}{2}\ \|A\mathrm{x} - b\|_2^2 + \alpha|y_1|_1 + \frac{\eta}{2}\ \|\nabla_w \mathrm{x} - y_1 + u_1\|_2^2 + \beta \sum_k |y_2(k)|_1$$

$$+ \frac{\Gamma}{2} \sum_k \|SH_k(\mathrm{x}) - y_2(k) + u_2(k)\|_2^2$$

where $u_1 \in \mathbb{R}^M$ and $u_2(k) \in \mathbb{R}^M$ are the newly defined scaled dual variables.

Finally, the problem is solved by iterating over equations (144-148):

$$\mathrm{x}^{(n+1)} \coloneqq \underset{\mathrm{x}}{argmin}\ \mathcal{L}\left(\mathrm{x}, y_1^{(n)}, y_2^{(n)}, u_1^{(n)}, u_2^{(n)}\right) \quad (144),$$

$$y_1^{(n+1)} \coloneqq \underset{y_1}{argmin}\ \mathcal{L}\left(\mathrm{x}^{(n+1)}, y_1, u_1^{(n)}\right) \quad (145),$$

$$y_2^{(n+1)} \coloneqq \underset{y_2}{argmin}\ \mathcal{L}\left(\mathrm{x}^{(n+1)}, y_2, u_2^{(n)}\right) \quad (146),$$

$$u_1^{(n+1)} \coloneqq u_1^{(n)} + \left(\nabla_w \mathrm{x}^{(n+1)} - y_1^{(n+1)}\right) \quad (147),$$

$$u_2^{(n+1)} \coloneqq u_2^{(n)} + \left(SH(\mathrm{x}^{(n+1)}) - y_2^{(n+1)}\right) \quad (148).$$

The optimal solution for the sub-problem by Eq. (144) requires finding roots of its derivatives that leads to Eq. (149):

$$\lambda A^T A\mathrm{x} - \lambda A^T b + \eta\ \mathrm{div}_{\mathrm{w}}(\nabla_w \mathrm{x} - y_1 + u_1) + \Gamma\left(\sum_k P_k^* P_k\ \mathrm{x} + \sum_k\ P_k^*\left(y_2(k) - u_2(k)\right)\right) = 0 \quad (149)$$

Where we can solve it in Fourier domain by multiplying both sides of it by F:

$$\left(\lambda S + \eta\, F\mathrm{div_w}\nabla_w F^* + \Gamma \sum_k \mathrm{diag}\left(\mathrm{vec}(|Z_k|.^2)\right)\right)F\mathrm{x} = \lambda b + \eta\, F\mathrm{div_w}(y_1 - u_1) + \Gamma \sum_k \mathrm{diag}\left(\mathrm{vec}(Z_k)\right)F\left(u_2(k) - y_2(k)\right) \quad (150)$$

Minimization in Eq. (145) and Eq. (146) can be attained by shrinkage operators such as:

$$y_1^{(n+1)} \coloneqq Shrink\left(\nabla_w \mathrm{x}^{(n+1)} + u_1^{(n)}, \vartheta_2\right) \quad (151)$$

$$y_2^{(n+1)} \coloneqq Shrink\left(SH(\mathrm{x}^{(n+1)}) + u_2^{(n)}, \vartheta_2\right) \quad (152)$$

where $\vartheta_1 = \frac{\alpha}{\eta}$, $\vartheta_2 = \frac{\beta}{\Gamma}$ and

$$Shrink(x, \xi)_n = sign(x_n).max\{|x_n| - \xi, 0\} \quad (153)$$

CHAPTER 3- EXPERIMENTS AND RESULTS

In this section, we evaluate the performance of the proposed compressed sensing MRI and CT reconstruction methods. Also, we assess the performance of the proposed 3D object reconstruction and material discrimination methods in sparse-view neutron-photon computed tomography.

3.1. CT reconstruction results

In this section: First, we evaluate the performance of the proposed AIRR method which classified as iterative reconstruction-reprojection (IRR) methods. Second, we assess the performance of the proposed CT reconstruction methods including CTV, and Nonconvex L1-L2 CT. Third, we evaluate the proposed 3D object reconstruction and material discrimination methods in sparse-view Neutron-Photon computed tomography.

3.1.1. Algebraic Iterative Reconstruction-Reprojection (AIRR) Method

For analyses, we use the distance between the reconstructed images and the original phantom image. The distance is calculated according to Eq. (154) [38].

$$Distance = \left(\frac{\sum_{x=1}^{l} \sum_{y=1}^{l} \left(f_{final}(x,y) - X(x,y) \right)^2}{\sum_{x=1}^{l} \sum_{y=1}^{l} (X(x,y))^2} \right)^{\frac{1}{2}} \quad (154),$$

where X is the original $l \times l$ and f_{final} is the reconstructed phantom images.

We evaluate the AIRR method for the fan-beam sparse-view reconstruction on noise-free and noisy projections whose models are defined in Eq. (14) and Eq. (15). In the experiments, l = 256, and for the shearlet-based denoising the number of scales is 3, and the number of directions is 4 step. For noise-free and noisy cases, Noise, n in Eq. (15) is AWG, $\sigma = 10$. Reconstruction is performed from twenty fan-beam projections. Same as in [38] settings are applied for experiments. In Figure 3.1 the distance metrics are shown for the proposed AIRR, IRR and IRR-TV. The proposed AIRR method displays a better performance. The result does not diverge as fast as for other two methods because we update the geometry matrix in the reprojection step. Figure 3.2 shows how the methods under comparison perform in the presence of noise. The IRR-TV shows a better performance in the first three iterations, however it is not stable and as it can be observed, the result diverges after few iterations. The AIRR method has outperformed the IRR-TV for noisy method as well. Figure 3.3 illustrates also the phantom image reconstruction for the noise-free case. The AIRR based reconstruction in Figure 3.3 (a) shows a better contrast if compared that to IRR-TV. Some visible artifacts in the presence of noise are observed in Figure 3.4. SSIM [78] as a standard metric. Table 3.1 summarizes structural similarity indices [78] which are calculated and presented to demonstrate how the structural content is preserved by methods. The AIRR method performs very well on noisy and noise-free models.

Table 3.1 Structural similarity indices for methods per noisy and noise-free projections.

Model / Method	Noise-Free Projections	Noisy Projections
Proposed (AIRR)	0.6769	0.6169
IRR-TV	0.6692	0.5670
IRR	0.6004	0.5275

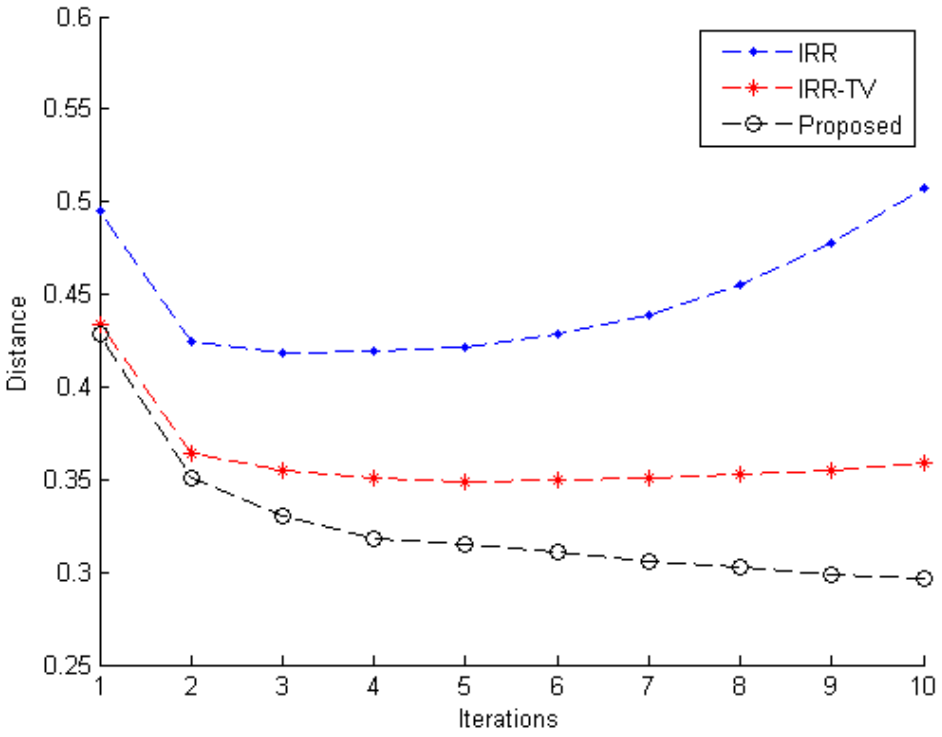

Figure 3.1 Distance metric for different number of iterations for noise-free projections per IRR, IRR-TV, and AIRR.

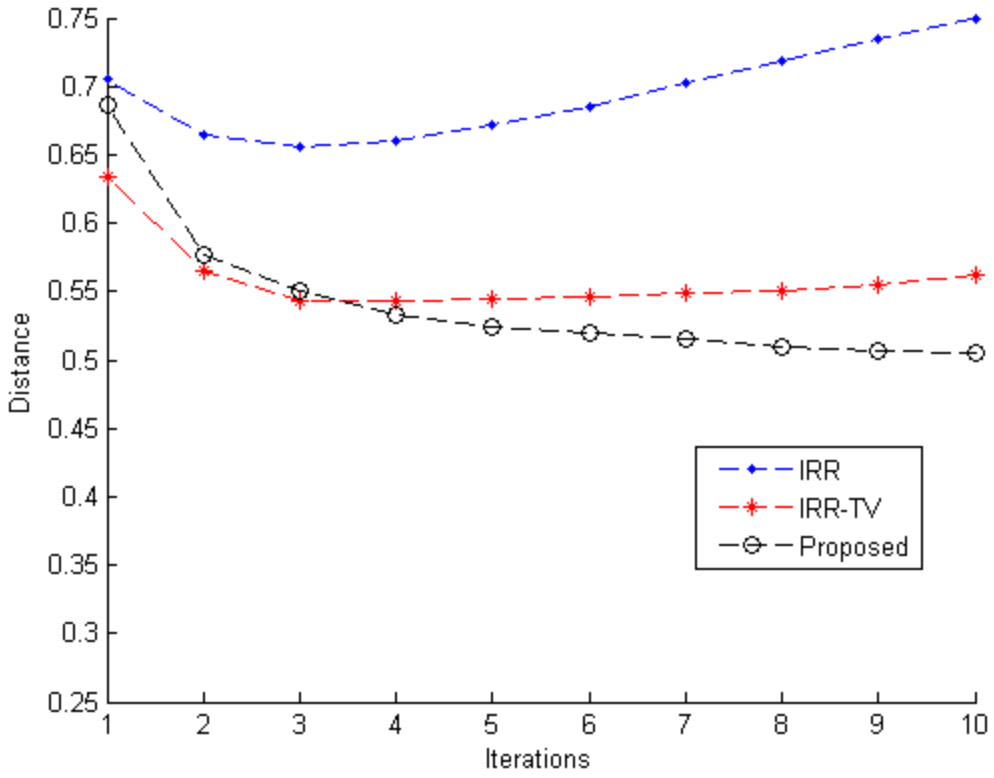

Figure 3.2 Distance metric for different number of iterations for noisy projections (AWG: $\sigma = 10$) per IRR, IRR-TV, and AIRR.

Figure 3.3 (a) Original phantom image

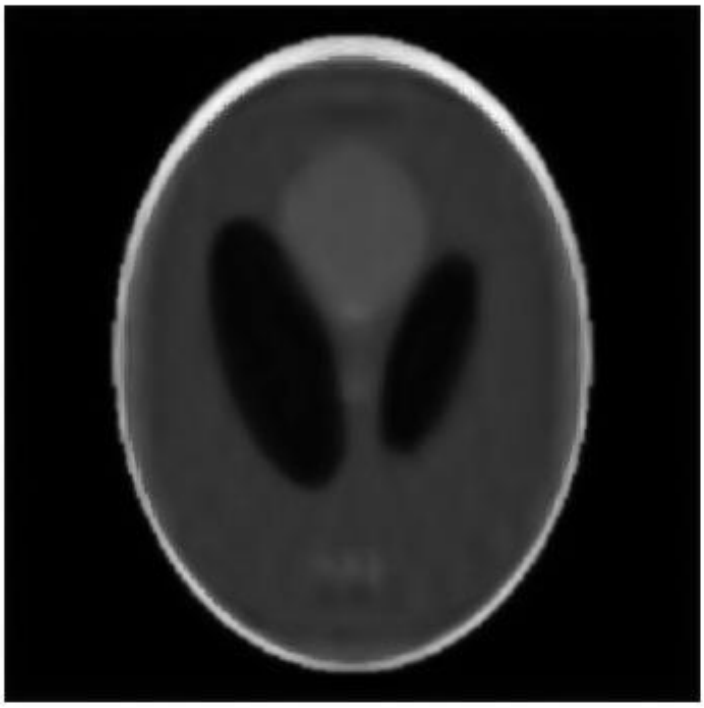

Figure 3.3 (b) The AIRR reconstruction from the noise-free sparse-view projections

Figure 3.3 (c) IRR-TV reconstruction from the noise-free sparse-view projections

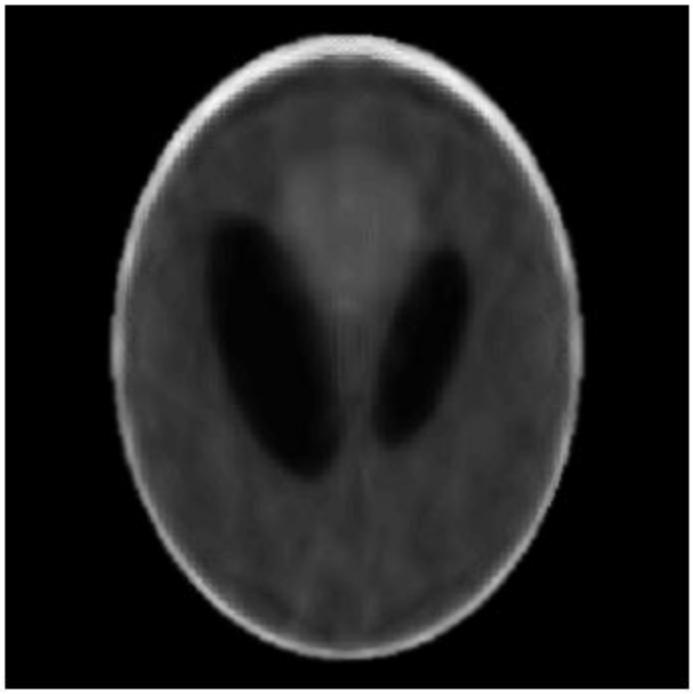

Figure 3.3 (d) IRR reconstruction from the noise-free sparse-view projections

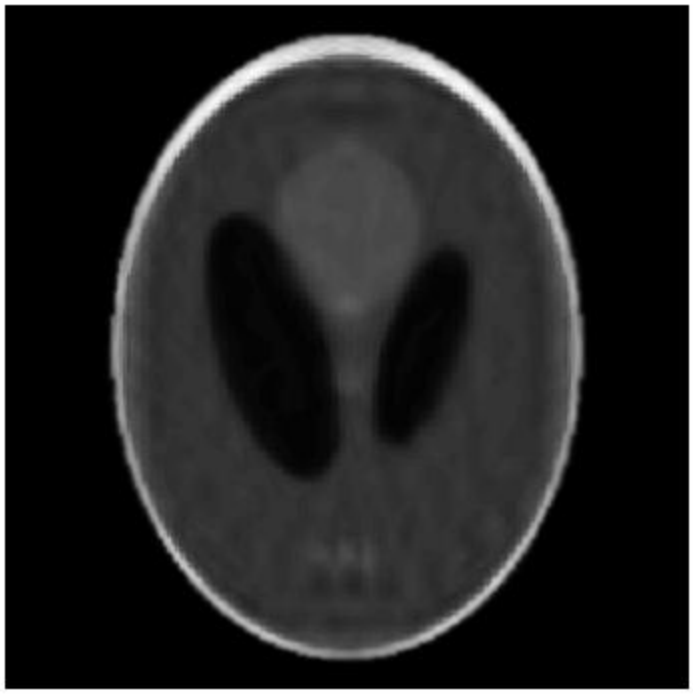

Figure 3.4 (a) Proposed AIRR reconstruction from the sparse-view noisy projections

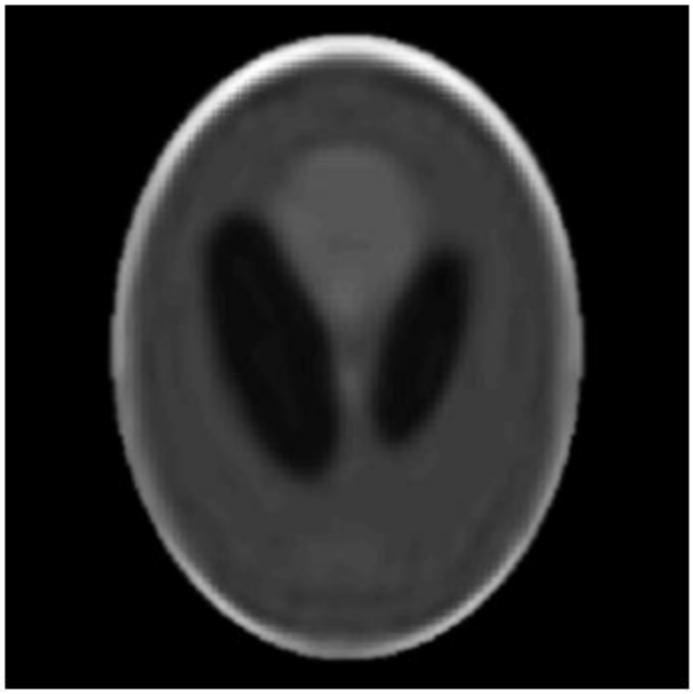

Figure 3.4 (b) IRR-TV reconstruction from the sparse-view noisy projections

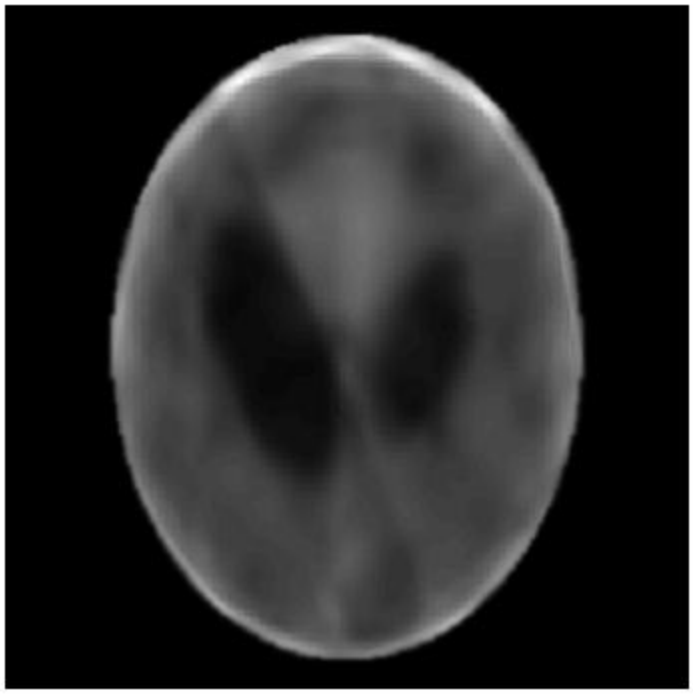

Figure 3.4 (c) IRR reconstruction from the sparse-view noisy projections

3.1.2. Computed Tomography Methods: CTV and Nonconvex L1-L2 CT

The CTV and nonconvex L1-L2 CT methods are evaluated for fan-beam geometry on the SheppLogan phantom [53] and the "head" phantom [79] (Figure 3.5). Data are of the size of 256×256 pixels and they are simulated with 100 projections spaced equally. Reconstruction is performed using TV-based regularization (TV), wavelet-based regularization (wavelet), curvelet-based regularization (curvelet).

Figure 3.5 Left: SheppLogan phantom, Right: FORBILD head phantom

3.1.2.1. CTV

Figures 3.6 and 3.7 show the reconstruction results by the methods for SheppLogan and FORBILD phantoms. The peak signal-to-noise ratios (PSNR) are presented in Table 3.2.

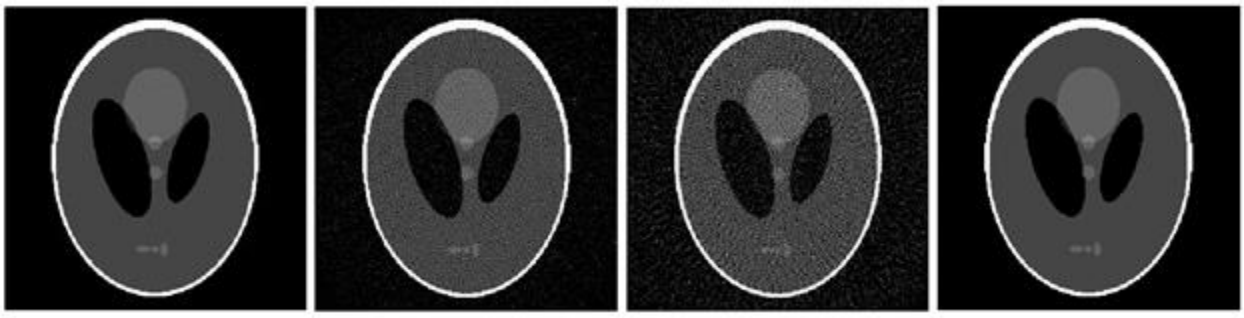

Figure 3.6 Left to right: SheppLogan phantom reconstruction result using TV, curvelet, wavelet and the CTV methods

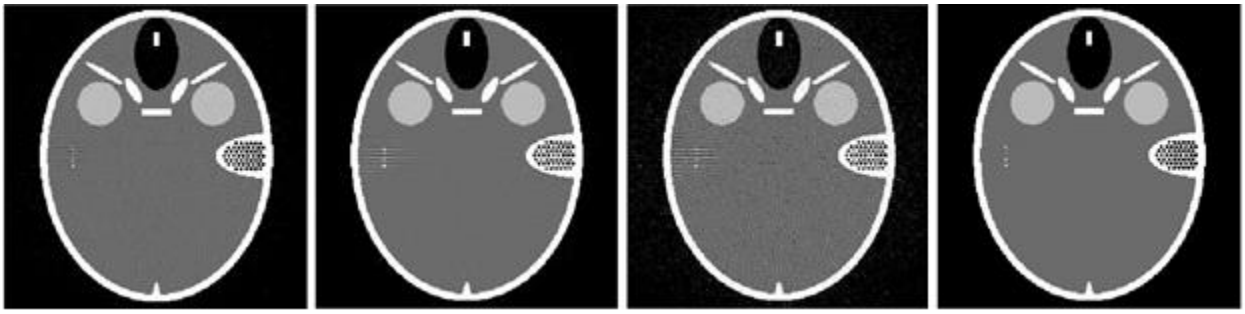

Figure 3.7 Left to right: FORBILD head phantom reconstruction result using TV, curvelet, wavelet and the CTV methods

Table 3.2 PSNR (dB) values for the methods in our experiment

Method	SheppLogan phantom	FORBILD phantom
TV	31.4	29.6
Curvelet	26.6	28.7
Wavelet	19.2	22.0
CTV	37.7	36.2

3.1.2.2. Nonconvex L1-L2 CT

Figure 3.8 and Figure 3.9 show the outcomes of the methods, i.e., a substantial reduction of visible artifacts by the proposed method. The peak signal-to-noise ratio (PSNR) represents the objective metrics presented in Table 3.3, and also demonstrates the high performance achieved by the developed method.

Table 3.3 PSNR (dB) values for the methods in our experiment

	SheppLogan phantom	FORBILD phantom
Wavelet	19.2	22.0
Curvelet	26.6	28.7
TV	31.4	29.6
CTV	37.7	36.2
Nonconvex L1-L2 CT	39.8	38.7

Figure 3.8 Left to right: SheppLogan phantom reconstruction result using Wavelet, Curvelet, TV, CTV, and the Nonconvex L1-L2 methods

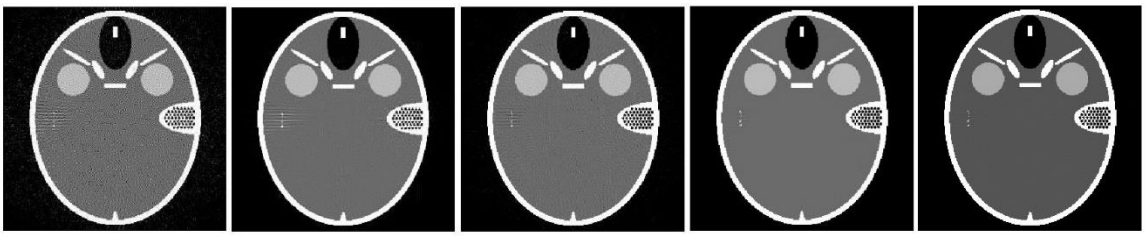

Figure 3.9 Left to right: FORBILD head phantom reconstruction result using Wavelet, Curvelet, TV, CTV, and the Nonconvex L1-L2 methods

3.1.3. Sparse-view fan-beam neutron-photon computed tomography

3.1.3.1. 3D reconstruction and imaging

The described method, in section 2.1.4.1.2, based on FBP reconstruction algorithm was applied to projections obtained for each source separately. For the goal of object reconstruction and material discrimination, the 14-MeV and 2.5-MeV neutron sources and photon sources with energy of 1 MeV, 3 MeV, 6 MeV, and 9 MeV were employed. The methods applied were: (a) visualization of reconstructed 2D slices as a 3D scene for each source separately, (b) visualization in 3D of ratios of reconstructed values obtained by projections generated by two similar sources at different energy levels, and (c) visualization in 3D of ratios of reconstructed values obtained by projections generated from different radiation sources. We also show how we improve representation of objects by combining images by the neutron source and the values of ratio as in c).

Figure 3.10a shows the sinogram (projections) of 2.5-MeV neutron source, and Figure 3.10b shows one reconstructed 2D slice (#34).

In the model in Figure 3.11, the container is fully filled with a combination of high-Z and low-Z materials to represent a scenario of a cluttered scene. In this model, iron, aluminum and polyethylene cells were placed in a staircase way so that at any angle, the line of the side view goes throughout the combination of these materials.

3.1.3.2. Material identification

Results of the study are demonstrated in Figures 3.12 – 3.15. Figure 3.12a shows ratios of 1-MeV to 9-MeV photon transmissions per voxel. The lead is present in the plot, but the three polyethylene cells of different shapes are not because of transparency of low-Z materials for x-rays. The 3D plot of 14-MeV to 2.5-MeV neutron transmissions is shown Figure 3.12b. Both low- or high-Z are visible. The error of the shape reconstruction was calculated as a portion of voxels lost/appeared in the objects' actual voxels. The rate of the error is 55.4% and 21.6% for Figures 3.12a and 3.12b, respectively. We observe that shapes are better preserved. Although high-Z and low-Z materials can be discriminated, but lead and iron are not separated. The ratio of reconstructed values of voxels from 6-MeV photon to 2.5-MeV neutron transmissions can visualize differences between low-Z and high-Z materials. It is observed that objects made of low-Z vanish from the view at the rate reciprocal to the object size and the photon energy. The reconstruction errors in Figures 3.13a and 3.13b are is 37.9% and 49.2%, respectively.

The visualization method proposed here superimposes the reconstruction of the neutron source data and the photon-to-neutron transmission ratio data. As a result, in Figure 3.14a shapes plus materials can be inspected, efficiently. The overall error is 18.1%. The same approach for 4-MeV neutron and 6-MeV photon sources resulted in Figure 3.14b, with the error as high as 21.6%).

Figure 3.15 shows the result of 3D reconstruction for 2.5-MeV neutron and 6-MeV photon sources of the entirely filled-up container. The CT reconstruction resolves regions of iron, aluminum and polyethylene yielding only 2.5% of error. As it can be observed, neutron-photon CT allow us to effectively visualize shapes of objects and differentiate materials inside the cluttered container.

In this section, we investigate the sparse-view CT reconstruction of objects under scrutiny in the combined neutron-photon system, the container and the objects of different shapes and material composition inside it were ideal. In the next section, the CT reconstruction and imaging techniques in the sparse-view conditions such as iterative reconstruction methods will be investigated.

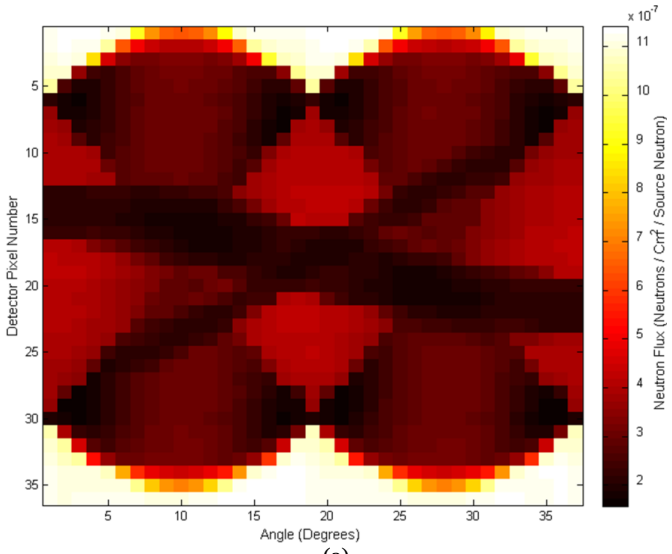

(a)

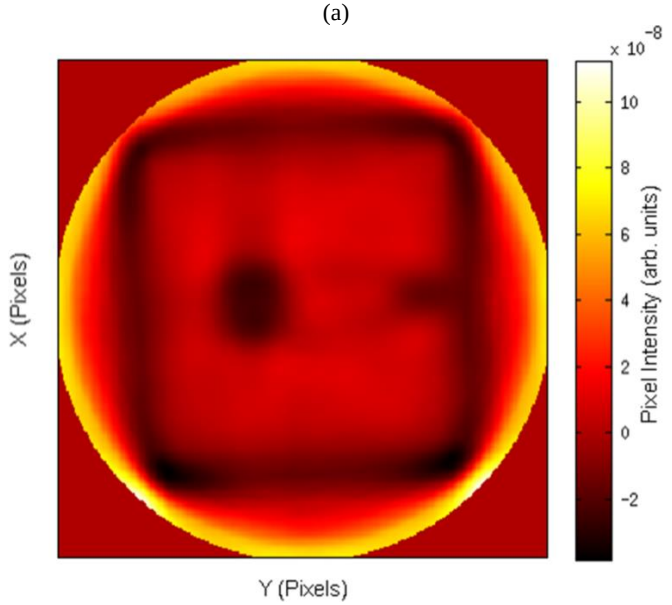

(b)

Figure 3.10 (a) The sinogram and (b) the radiograph for one slice

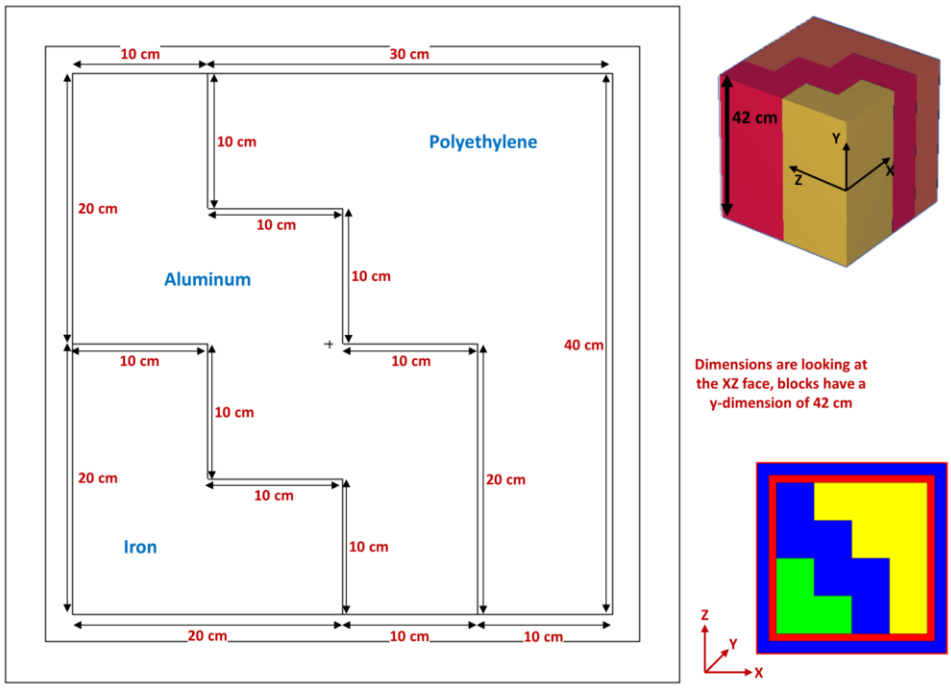

Figure 3.11 Model of the fully filled container [63]

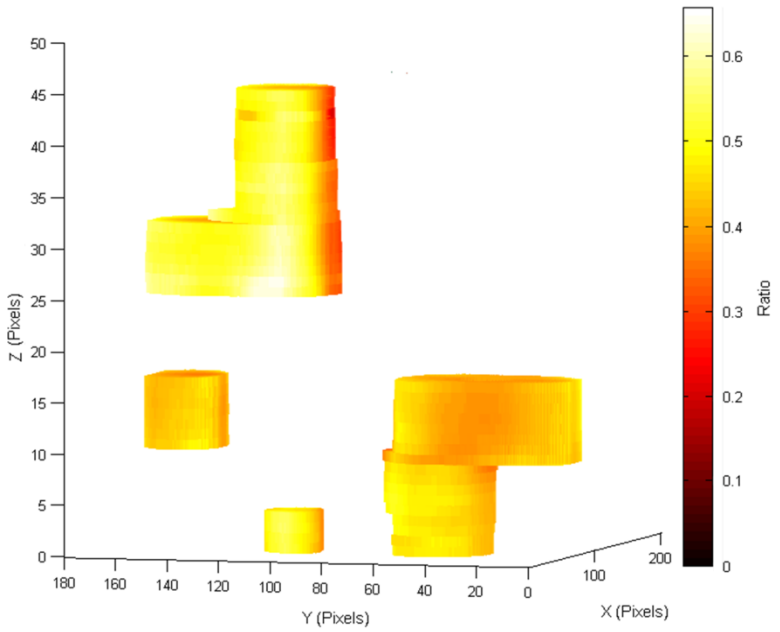

(a)

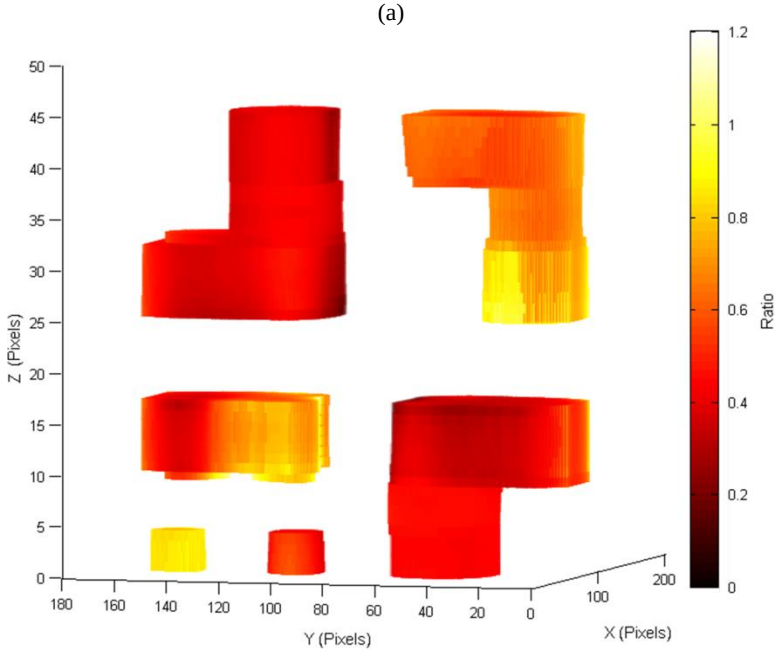

(b)

Figure 3.12 3D visualization of transmission ratios per voxel using (a) 1-MeV and 9-MeV photon sources and (b) 14-MeV and 2.5-MeV neutron sources

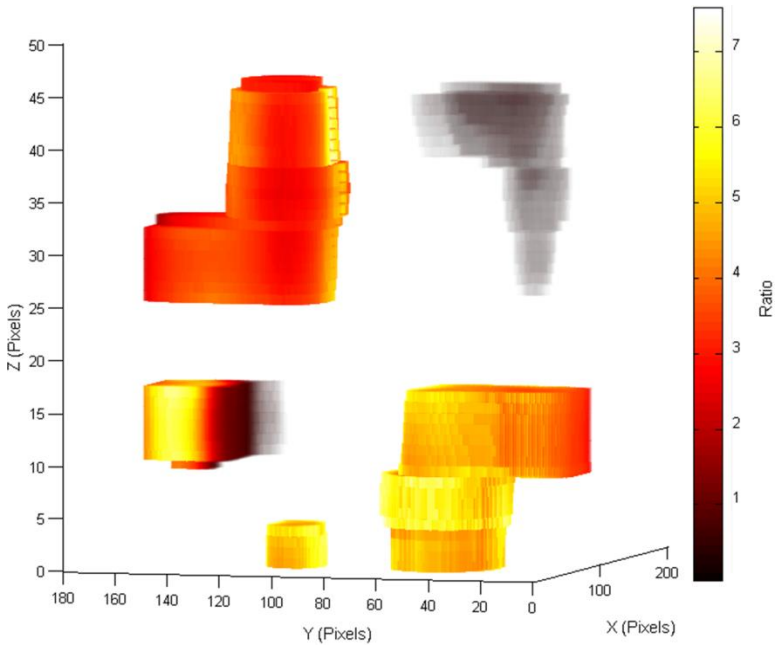

(a)

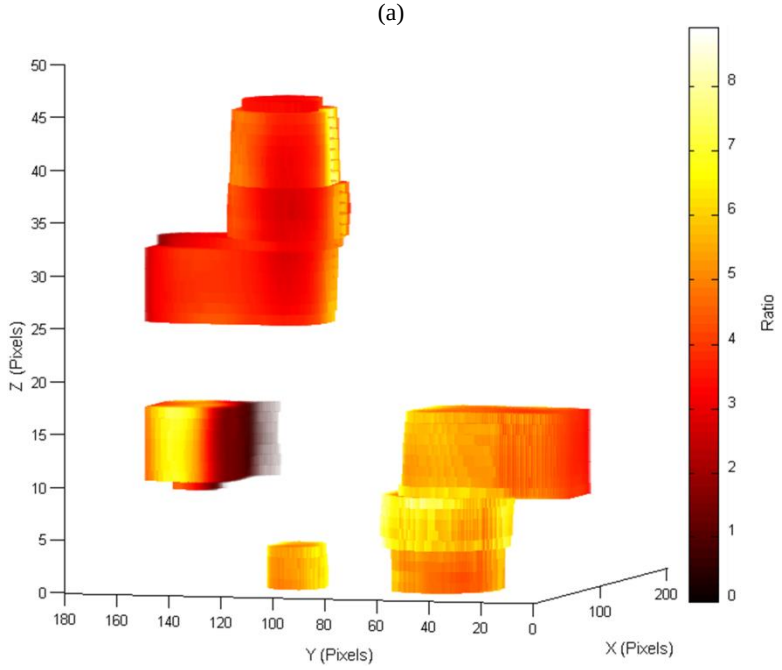

(b)

Figure 3.13 3D visualization of the ratios in the container voxels using transmission data for (a) 6-MeV photons to 2.5-MeV neutrons, and (b) 9-MeV photons to 2.5-MeV neutrons

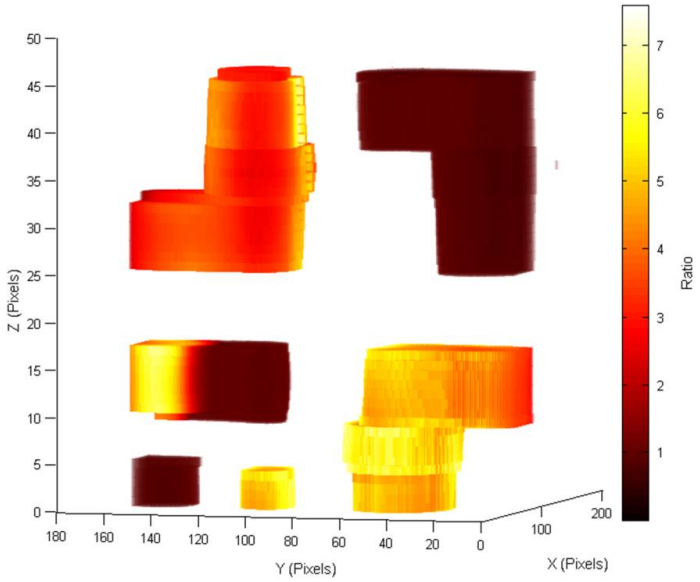

(a)

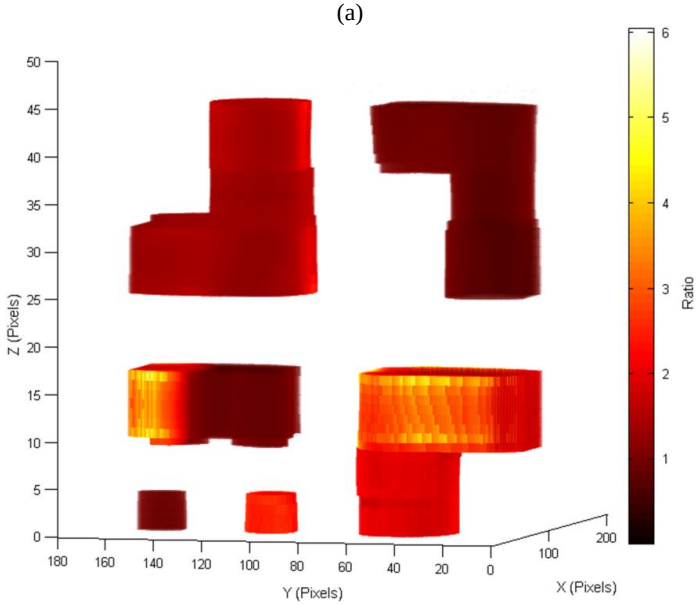

(b)

Figure 3.14 Fusion of 3D reconstruction from neutron source and the ratio of the reconstructed projections from neutron and photon sources: (a) 2.5-MeV neutron reconstruction and the ratio of 6-MeV photon to 2.5-MeV neutron reconstructions; (b) 14-MeV neutron reconstruction and the ratio of 6-MeV photon to 14-MeV neutron reconstructions

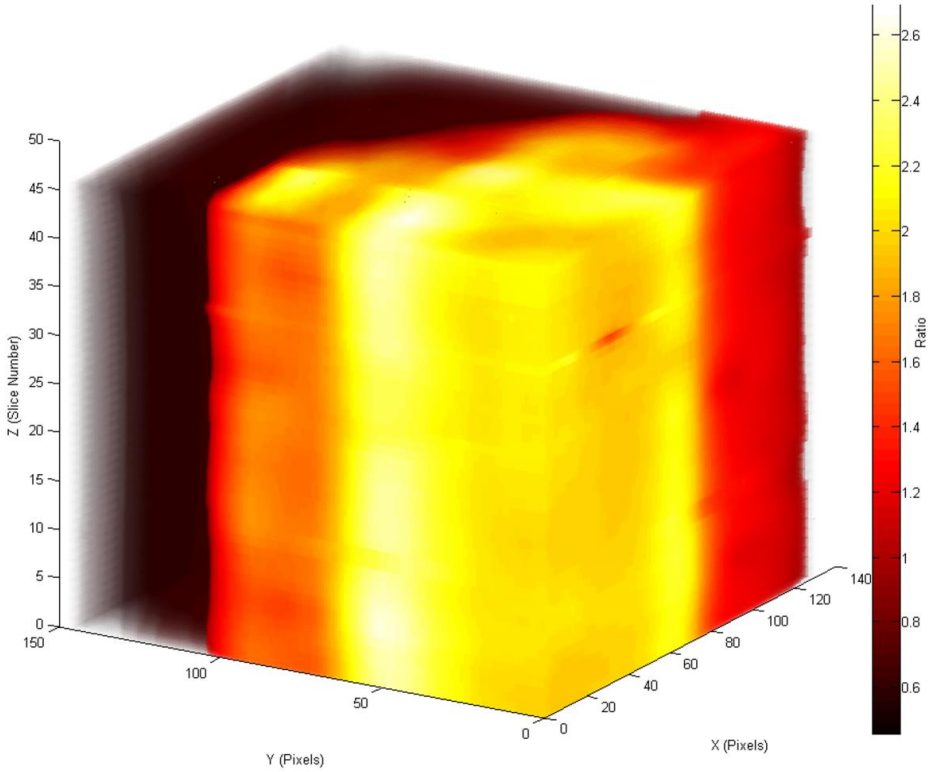

Figure 3.15 3D reconstruction of a fully filled container model using 2D scans obtained with 6-MeV photon source and 2.5-MeV neutron source

3.1.4. Sparse-view cone-beam neutron-photon computed tomography

3.1.4.1. 3D reconstruction and imaging

Two model scenes have been reconstructed using the described iterative reconstruction (IR) methods described in section 2.1.5.2.2.2 and the traditional Feldkamp, Davis and Kress (FDK) method [80]. The stopping criteria for CTV is defined as $\|b - Ax\|_2^2 \leq \sigma$. If $\|b - Ax\|_2^2 \leq$10-4, the algorithm terminates. The reconstruction errors are presented in Table 3.4 for FDK, IR+TV, IR+W and CTV algorithms for the 2.5-MeV neutron images only. The error is calculated as a percentage of voxels lost/added of the object's actual voxels.

Table 3.4 Reconstruction error for neutron sources

Method	Reconstruction error (Model 1)	Reconstruction error (Model 2)
FDK	9.2617%	9.8625%
Regularized Wavelet	8.9713%	9.1264%
Regularized TV	8.0419%	8.9845%
CTV	7.6324%	7.9058%

The errors of reconstruction for the 6-MeV photon images have been calculated only for high-Z objects (Table 3.5) due to the almost complete transmission of 6-MeV photons through low-Z materials as shown in Figure 3.16.

Table 3.6 demonstrates how the error grows when the number of angles in the sparse view is reduced to 18, corresponding to a rotational increment of 10 degrees. Due to the superiority of our CTV method, the latter is selected for object visualization. Reconstruction of Model 1 with 36 angles is shown for photon and neutron sources in Figures 3.16 and 3.17, and for Model 2 in

Figures 3.18 and 3.19, and for 18 angles in Figure 3.20, respectively. Three coordinates in Figures 3.16 – 3.20 are x, y, z coordinates in the reconstruction space. The reconstruction in Figures 3.16 – 3.20 is shown after interpolation.

To summarize, the neutron images represent shapes of low- and high-Z made objects equally well under the sparse views as it can be concluded from Tables 3.5 and 3.6. In Table 3.5, because of photons penetrate through low-Z materials, the accuracy is calculated for only high-Z objects. The CTV method is capable of separating objects which are close to each other and of capturing the main geometric features of objects under the sparse view setting. For the models under considerations, 36 angles are a minimum required for separating objects spatially. Table 3.6 indicates that when the number of angles is reduced to a half of the original number, which is from 36 angles to 18, the reconstruction error has increased significantly.

Table 3.5 Reconstruction error for photon sources

Method	Reconstruction error (Model 1)	Reconstruction error (Model 2)
FDK	13.7320%	8.1441%
Regularized Wavelet	11.4988%	8.8706%
Regularized TV	10.2682%	6.6953%
CTV	9.5469%	6.1576%

Table 3.6 Reconstruction error for neutron sources using 18 angles

Method	Reconstruction error (Model 1)	Reconstruction error (Model 2)
FDK	33.4936%	38.1161%
Regularized Wavelet	28.8301%	33.5375%
Regularized TV	25.9895%	29.7274%
CTV	23.4854%	27.8003%

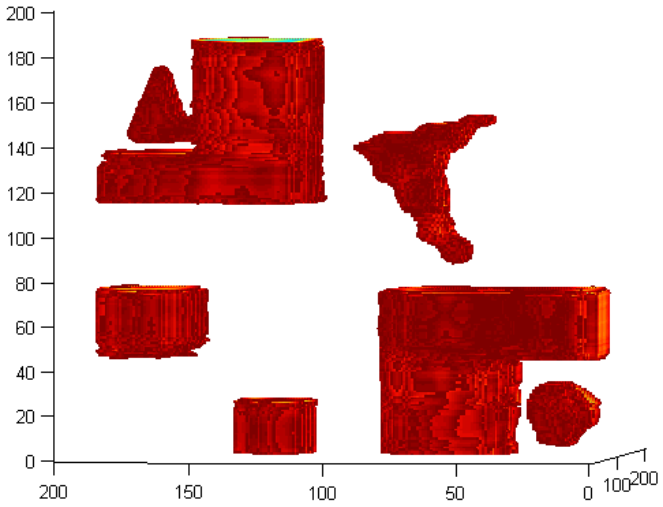

Figure 3.16 3D visualization of the reconstruction for Model 1 using the 6-MeV photon source

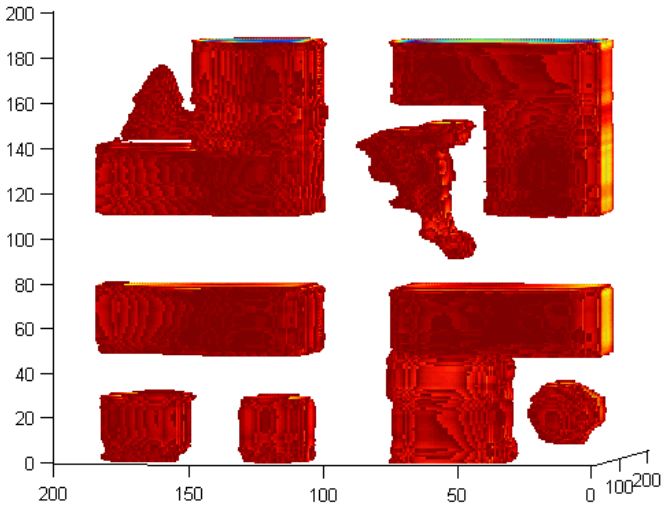

Figure 3.17 3D visualization of the reconstruction for Model 1 using the 2.5-MeV neutron source

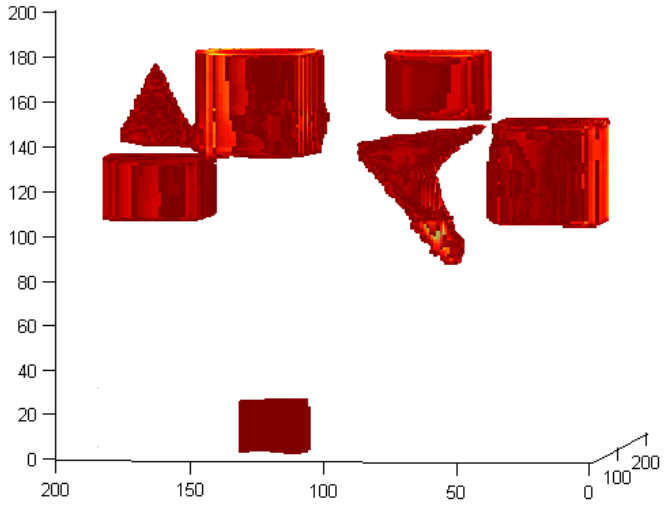

Figure 3.18 3D visualization of the reconstruction for Model 2 using the 6-MeV photon source

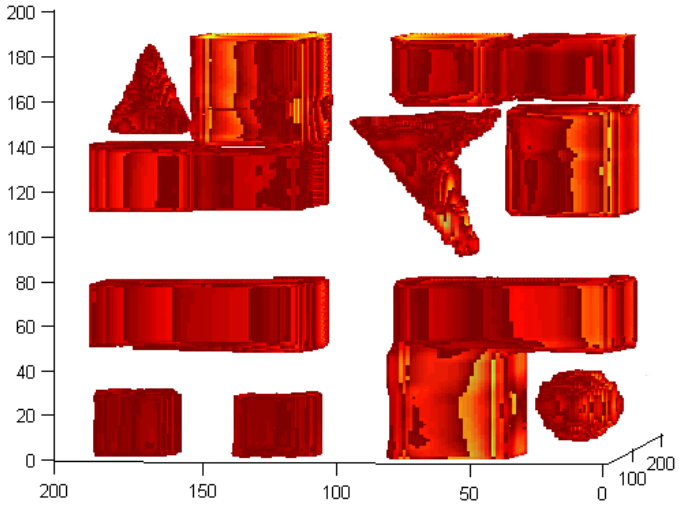

Figure 3.19 3D visualization of the reconstruction for Model 2 with the 2.5-MeV neutron source

3.1.4.2. Material Identification and Object visualization

3.1.4.2.1. 1D signatures

First, the photon-to-neutron transmission ratio, Rp/n, was evaluated. Figure 3.21 and Figure 3.22 plot the values of Rp/n for every voxel of objects/materials in Models 1 and 2, respectively. Voxel ordering is based on raster scan for each object. We refer to these plots as "1D material signatures". Note, that all voxels representing objects composed of the same material contribute to the plot. It can be observed that in a simple scene such as the one presented in the Model 1, the threshold separating those values pertaining to high-Z materials can be easily established for Rp/n. For Model 2, the signatures become closely packed and the average value is no longer robust for representing the material.

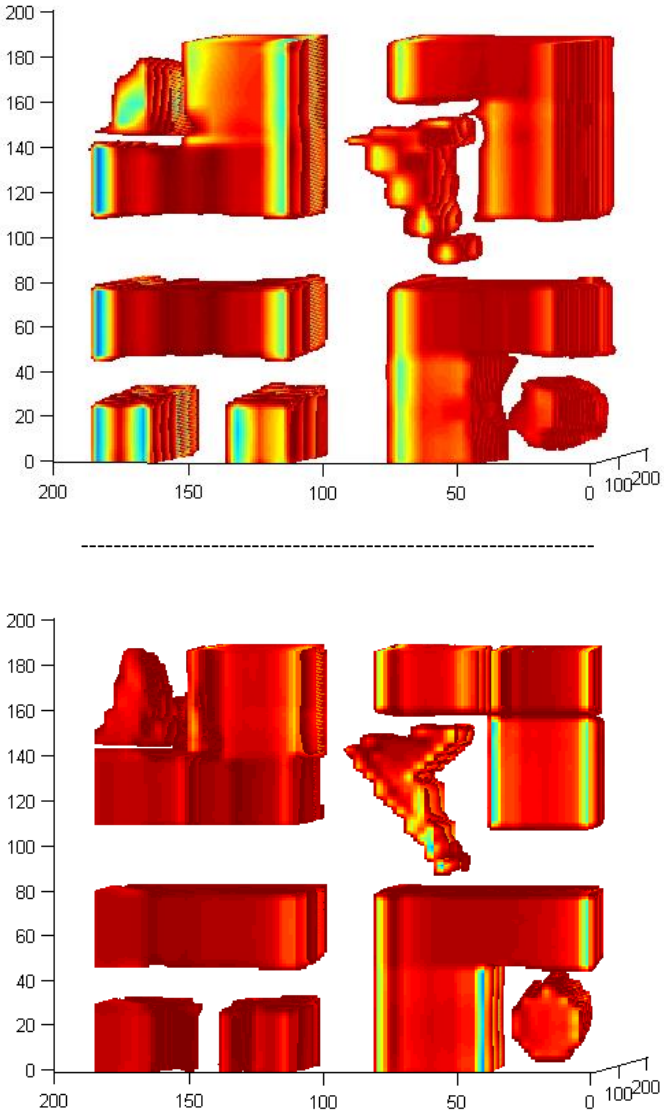

Figure 3.20 3D visualization of the reconstruction using the 2.5-MeV neutron source for Model 1 (top) and Model 2 (bottom) with 18 angles (10^{o} increment)

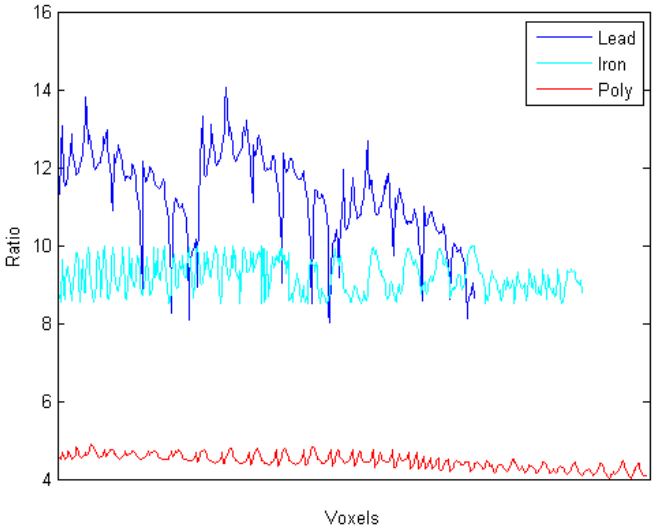

Figure 3.21 1D material signatures: Rp/n per material for Model 1

3.1.4.3. 2D signatures

Now, we introduce 2D material signatures plotted as Rp/n versus Tn values, (Rp/n - Tn) for each object voxel. The plot presented in Figure 3.23 illustrates these 2D signatures for Model 1 materials; values per voxels are represented by point values.

The means of (Rp/n , Tn) clusters are now moved away from each other, making them useful for representing materials. Figures 3.24 and 3.25 respectively display the 2D signatures for the high-Z and low-Z materials included in Model 2. The discrimination among high-Z materials is apparent. Figure 3.26 shows the 2D signatures for the aggregate of individual high-Z materials and grouped low-Z materials used in Model 2. We observe from Figure 3.27 that decoupling for materials of close atomic numbers (z) such as graphite (Carbon, z=6) and Boron (z=5) is problematic. However, when the difference in atomic numbers is greater than 6, as in the model,

partitioning the materials based on 2D signatures promises better accuracy than that based on 1D signatures.

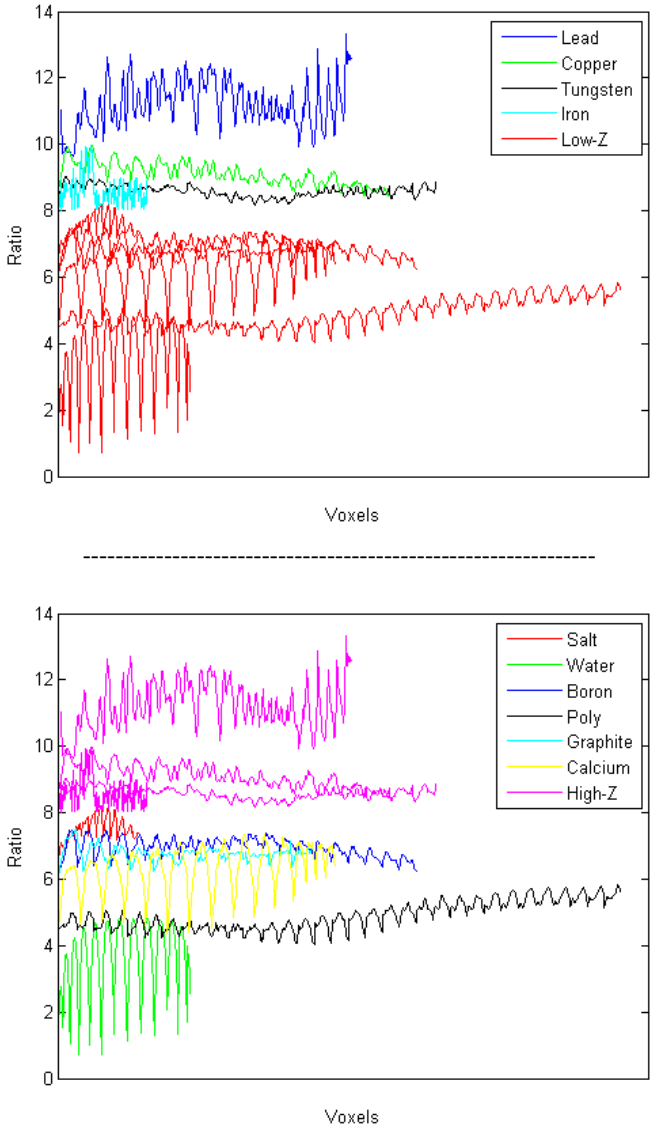

Figure 3.22 1D material signatures: Rp/n per material for Model 2; Top: high-Z materials with low-Z materials grouped together; bottom: low-Z materials with high-Z materials grouped together

Calculated mean and standard deviation values are listed in Table 3.7. Treating these data as a library of materials for objects under inspection, we can calculate the distances in 2D space of

2D signatures for each unknown voxel and compare the results to the mean values in the library. The minimum value for the unknown voxel establishes the material of the object under inspection. This is similar to the k-means clustering [81,82], which would define the mean and standard deviation of each cluster using the data from Table 3.7. The objective distance function to minimize is

$$D = \sum_{i=1}^{C} \sum_{j=1}^{n} \left\| x_j^i - M_i \right\|^2 \tag{155}$$

Where x_j^i corresponds to the signature value in the reconstructed voxel and M_i is the cluster center in the library. C is the number of materials (clusters) and n is the number of data points in each of the respective clusters. Applied to the voxels of objects found using shape reconstruction of neutron transmissions, this approach leads to a noisy classification of materials. Post-processing of the results, based on majority voting per object, yields the reconstructions for Model 1 (Figure 3.27) and Model 2 (Figure 3.28 for high-Z materials). In Figures 3.27, 3.28 random colors assigned to detected classes. The performance of material classification using 1D and 2D signatures, (i.e. Rp/n and (Rp/n – Tn)) can be measured by analyzing the accuracy of forming reconstructed image objects. This is done by calculating the percentage of misclassified object voxels to the total number of voxels in the reconstructed image objects for Model 1 (Table 3.8) and Model 2 (Table 3.9).

Now in order to evaluate the robustness of the proposed 2D signatures, we consider modelling in the presence of error due to the electronic noise in the projection space. As we

mentioned earlier, our noisy imaging model is described by a linear system in Eq. (65). In Eq. (65), n is a additive Gaussian white noise vector with independent identically distributed elements. The relative noise level is 10%. Figures 3.29 and 3.30 show the 2D signatures for the high-Z and low-Z materials of Model 2 obtained after reconstructing noisy projections. Tables 3.10 and 3.11 report the reconstruction errors for neutron and photon sources, respectively. Table 3.12 lists the material statistics in the presence of noise. By comparing this table to the statistics in the material library table (Table 3.7), also from signatures and reconstruction of objects/materials in Figure 3.31, we can see that this level of noise which is a practical level the variation is not high enough to jeopardize the discrimination process.

Table 3.7 Material Library statistic

Material	Mean	Standard Deviation (σ_1, σ_2)
Lead	(2.9637e-11 , 11.2282)	(5.6577e-12 , 0.7004)
Copper	(5.9884e-11 , 9.1126)	(6.3621e-12 , 0.3297)
Tungsten	(8.5562e-11 , 8.5861)	(1.0666e-11 , 0.1696)
Iron	(4.1060e-11 , 8.6169)	(1.0143e-11 , 0.4759)
Salt	(4.8912e-11 , 7.5485)	(4.8526e-12 , 0.3292)
Water	(4.8841e-11 , 3.6257)	(1.5562e-11 , 1.0326)
Boron	(4.4498e-11 , 6.9580)	(4.4199e-12 , 0.2679)
Poly	(3.6353e-11 , 4.9068)	(3.8372e-12 , 0.4224)
Graphite	(4.5082e-11 , 6.7661)	(6.6158e-12 , 0.2183)
Calcium	(2.9765e-11 , 6.3372)	(4.2154e-12 , 0.6371)

Table 3.8 Material discrimination accuracy using 1D and 2D signatures for model one

Material	2D Accuracy	1D Accuracy	2D Overall Accuracy	1D Overall Accuracy
Lead	89.2038%	77.8136 %		
Iron	90.2524%	84.1477 %	93.1520%	87.3204%
Poly	100 %	100 %		

Table 3.9 Material discrimination accuracy using 1D and 2D signatures for model two

Material	2D Accuracy	1D Accuracy	2D Accuracy	1D Accuracy
Lead	89.7892%	91.6188%		
Copper	80.9153%	77.0238%	High-Z	High-Z
Tungsten	88.3264 %	74.8333%	85.0335%	77.4981%
Iron	81.1032%	66.5166%		
Salt	77.4711%	62.3471%	Low-Z	Low-Z
Water	93.5522%	81.0249%	60.9938%	62.1505%
boron	51.2637%	44.0696%		
Poly	81.9953%	85.7179%		
Graphite	54.2694%	41.9689%	Overall	Overall
Calcium	67.4109%	57.7743%	70.6097%	68.2895%

Table 3.10 Reconstruction error for neutron sources in the presence of noise

Method	Reconstruction error (Model 1)	Reconstruction error (Model 2)
FDK	15.8147%	17.9058%
Regularized Wavelet	12.9575%	13.9134%
Regularized TV	11.5469%	13.1270%
CTV	10.1419%	12.7922%

Table 3.11 Reconstruction error for photon sources in the presence of noise

Method	Reconstruction error (Model 1)	Reconstruction error (Model 2)
FDK	19.9320%	12.2673%
Regularized Wavelet	16.6865%	10.6166%
Regularized TV	14.6974%	9.7893%
CTV	12.9595%	8.6557%

Table 3.12 Material statistic in the presence of noise

Material	Mean	Standard Deviation (σ_1, σ_2)
Lead	(3.0963e-11 , 11.1575)	(6.4291e-12 , 1.0598)
Copper	(6.0906e-11 , 9.1119)	(6.3528e-12 , 0.4313)
Tungsten	(8.5540e-11 , 8.5713)	(1.0920e-11 , 0.3625)
Iron	(4.1141e-11 , 8.6504)	(1.0174e-11 , 0.4567)
Salt	(4.9194e-11 , 7.5359)	(4.9897e-12 , 0.3513)
Water	(4.9058e-11 , 3.6245)	(1.5724e-11 , 1.0396)
Boron	(4.4442e-11 , 6.9513)	(4.6190e-12 , 0.3352)
Poly	(3.6339e-11 , 4.8993)	(4.2592e-12 , 0.5109)
Graphite	(4.5106e-11 , 6.7855)	(6.8916e-12 , 0.2812)
Calcium	(2.9603e-11 , 6.3338)	(4.4524e-12 , 0.6757)

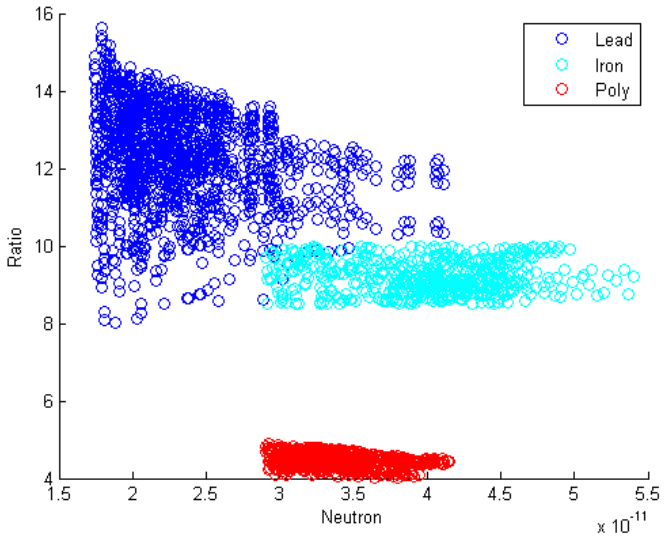

Figure 3.23 2D signatures (Rp/n - Tn): Model 1

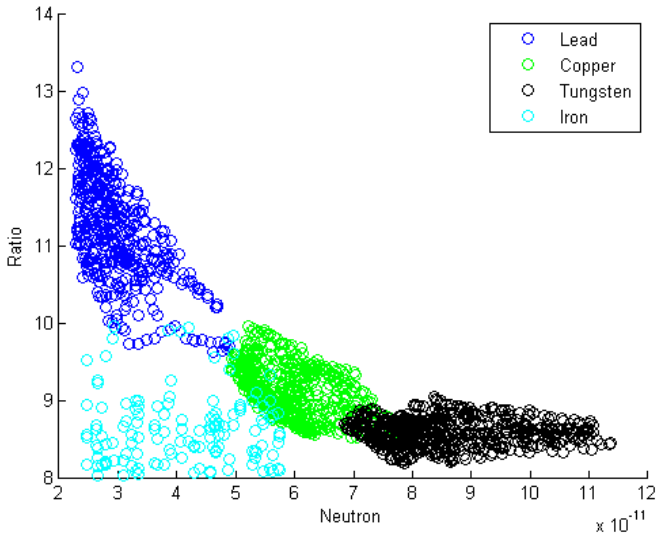

Figure 3.24 2D signatures of high-Z materials in Model 2

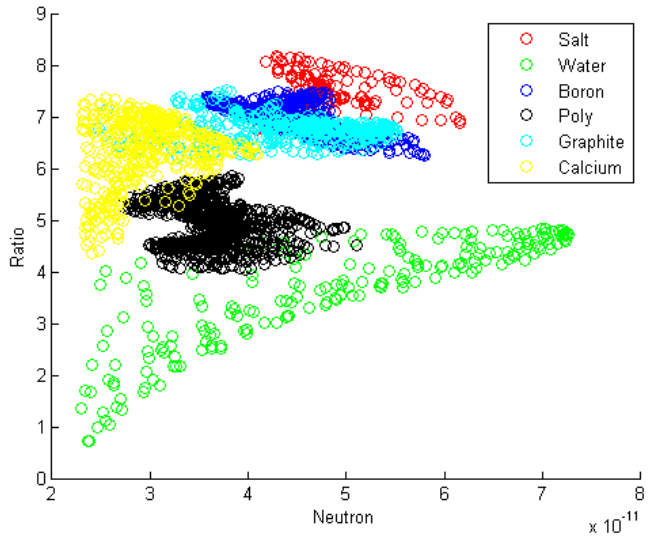

Figure 3.25 2D signatures of low-Z materials in Model 2

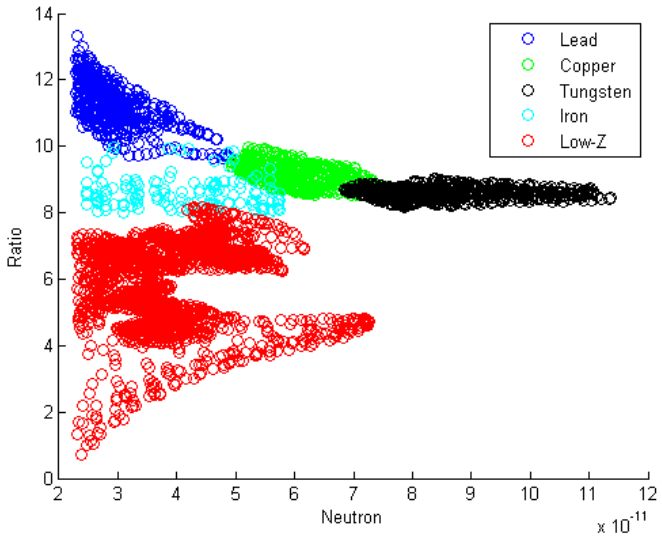

Figure 3.26 2D signature for Model 2, for high-Z materials plus low-Z materials grouped together

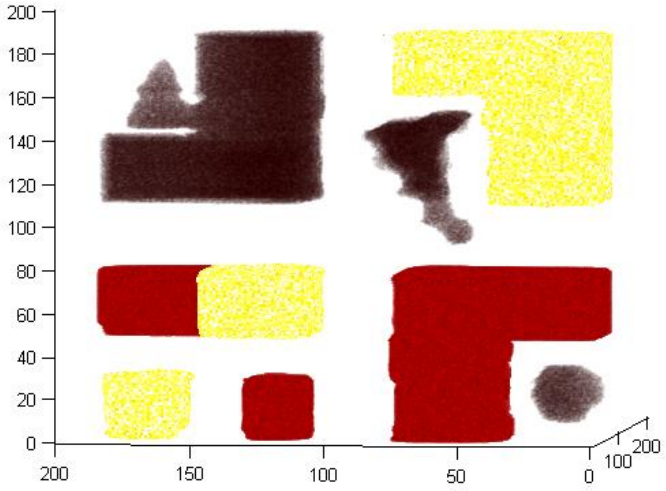

Figure 3.27 Classification result after majority voting/grouping for all materials in Model 1

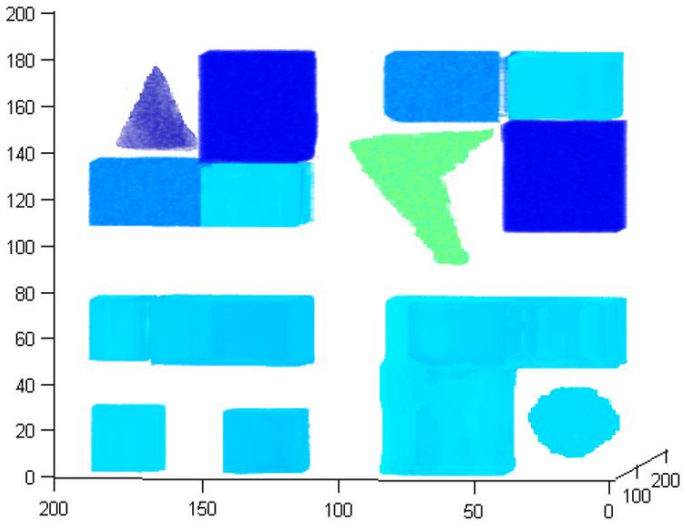

Figure 3.28 Classification result after majority voting/grouping for high-Z materials in Model 2

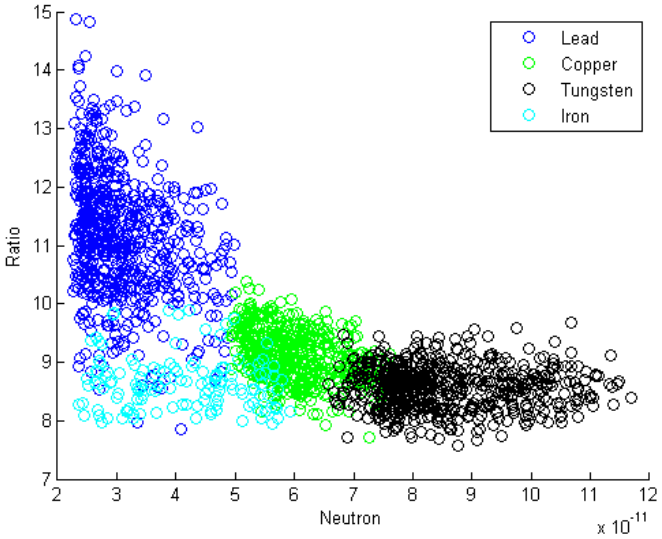

Figure 3.29 2D signatures of high-Z materials in Model 2 in the presence of noise

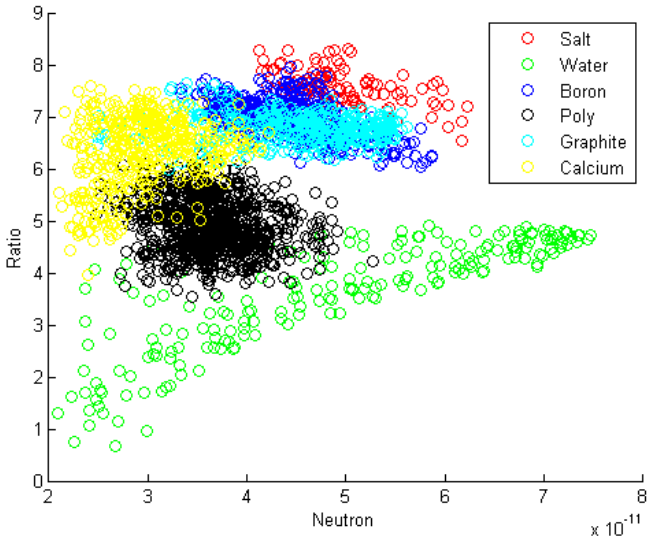

Figure 3.30 2D signatures of low-Z materials in Model 2 in the presence of noise

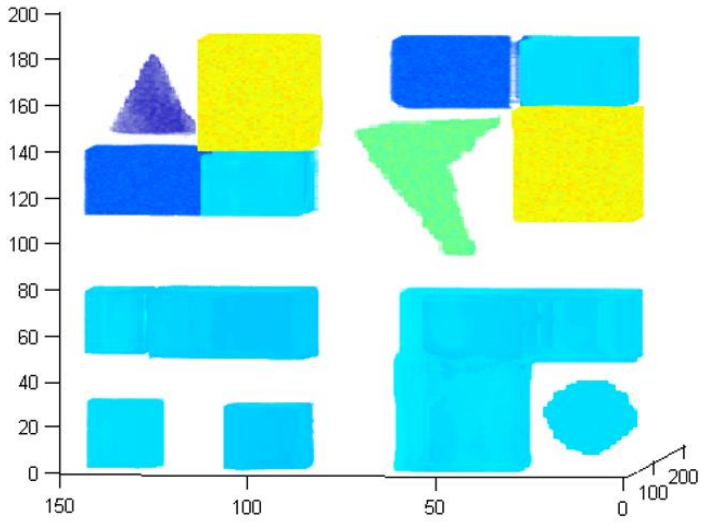

Figure 3.31 Classification result after majority voting/grouping for high-Z materials in Model 2 in the presence of noise

3.2. Compressed sensing MRI results

We evaluate the proposed compressed sensing MRI method on standard 256 × 256 MRI images that includes brain, chest, artery, and cardiac images [27] in Figure 3.32 We compared the performance of our algorithm with five previously introduced state-of-the-art methods: TVCMRI, RecPF, FCSA, FNTV, and FNSISTRA. We considered two different subsampling methods, i.e., random variable subsampling and radial subsampling. Figure 3.33 visualizes these two types of subsampling. For comparison to the reference methods we demonstrate results at the same number of iterations that is 50 iterations as a stopping criteria for all five methods to have a fair comparison. To evaluate the performance, we use four different sampling ratios including 15, 20, 25 and 30% to acquire the measurement b, respectively. The performance comparison is done using the SNR plots for methods under comparison, where $\mathrm{SNR} = 10\log_{10}\frac{\|\mathrm{x}\|_2^2}{\|\mathrm{x}-\mathrm{x}^n\|_2^2}$, x is the original image and x^n represents the reconstructed image after n interations. SNR values are measured for the above quantities of subsampling ratios, with radial and random subsampling.

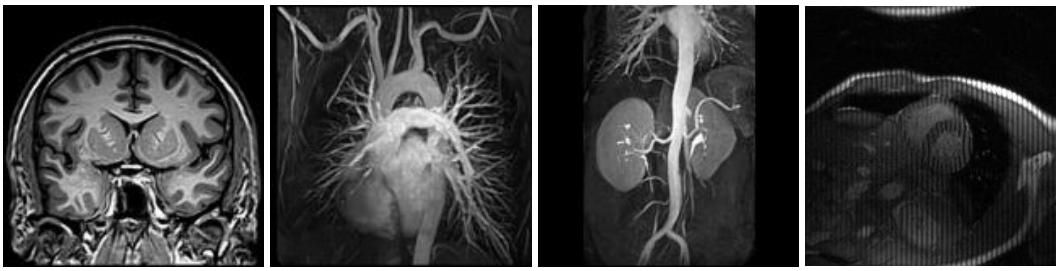

Figure 3.32 Images used to test the performance of the proposed compressed sensing methoda and comparison to reference methods: left to right: brain, chest, artery, and cardiac

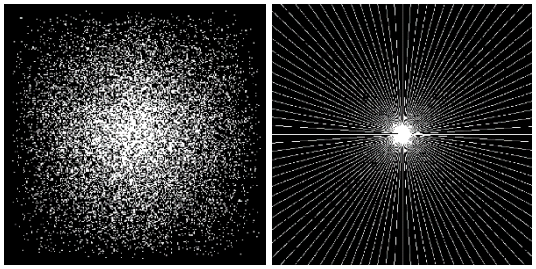

Figure 3.33 Left: random variable subsampling and right: radial subsampling

3.2.1. CT-TGV

We evaluate the proposed CT-TGV method here. For obtaining curvelet transform coefficients for realization of the method, we have used the curvelab implementation [83] because of the offered fast and efficient implementation. Figures 3.34 – 3.37 show the SNR plots for methods under comparison, SNR values are measured for various subsampling ratios, in radial and random subsampling types. As it follows from the plots, the CT-TGV method has achieved a better performance for both types of subsampling types and the overall performance varies based on the subsampling type and the type of the image. We demonstrate the reconstruction results for brain image with random subsampling and cardiac image with random subsampling in Figures 3.38 and 3.39, respectively. Table 3.13 shows improvement of the average SNRs by CT-TGV and five reference methods evaluated under random variable and radial subsampling at 20% subsampling ratios. number of repeated experiments for computing the average SNRs is 10. The improvement of the quality of reconstruction by the proposed CT-TGV method over the best performance among the reference methods that is one by the FNSISTRA is clearly shown in table 3.13. The superior performance of CT-TGV stems from utilization of total generalized variation which locates

sharper edges and suppress artifacts; and due to the exceptional spatial localization and directional selectivity of the curvelet transform.

Table 3.13 Improvement of the average signal to noise ratios (SNR) by CT-TGV at 20% random and radial sampling ratios

	MR Image	TVCMRI	RecPF	FCSA	FNTV	FNSISTRA
Random Subsampling	Brain	9.44	8.88	7.85	4.66	0.86
	Cardiac	6.08	5.40	4.28	2.12	0.82
	Artery	10.94	9.66	6.03	2.43	0.53
	Chest	8.03	7.64	7.39	4.86	0.80
Radial Subsampling	Brain	9.80	8.95	7.50	4.26	0.74
	Cardiac	8.92	6.50	4.44	2.73	0.51
	Artery	8.93	6.88	6.30	1.73	0.42
	Chest	8.98	7.39	6.42	4.21	0.48

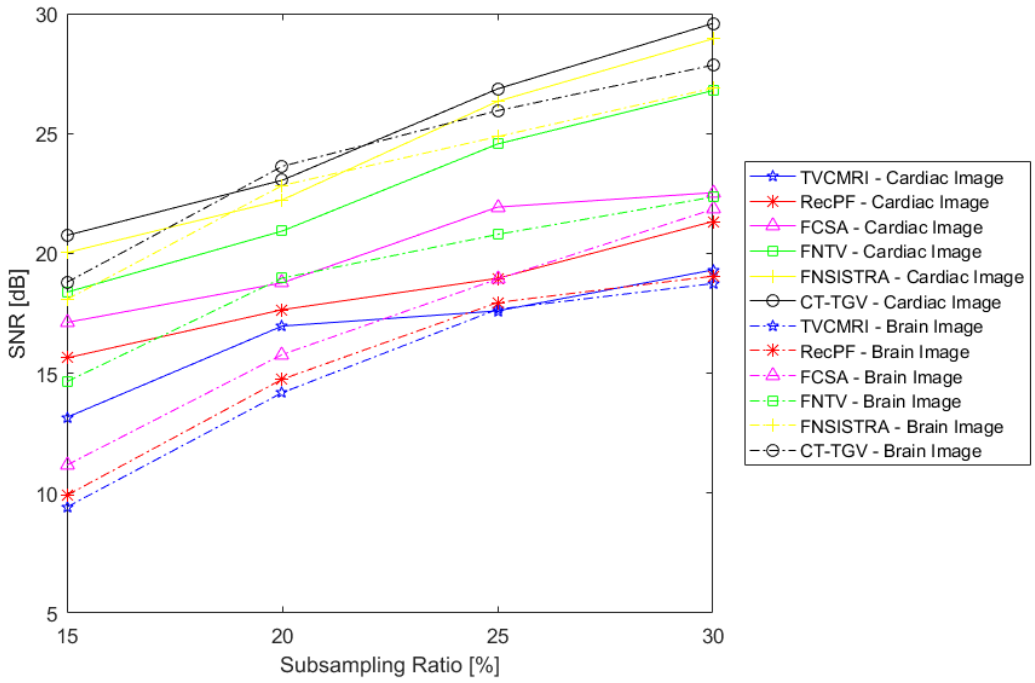

Figure 3.34 The performance of different methods with random subsampling for cardiac and brain images

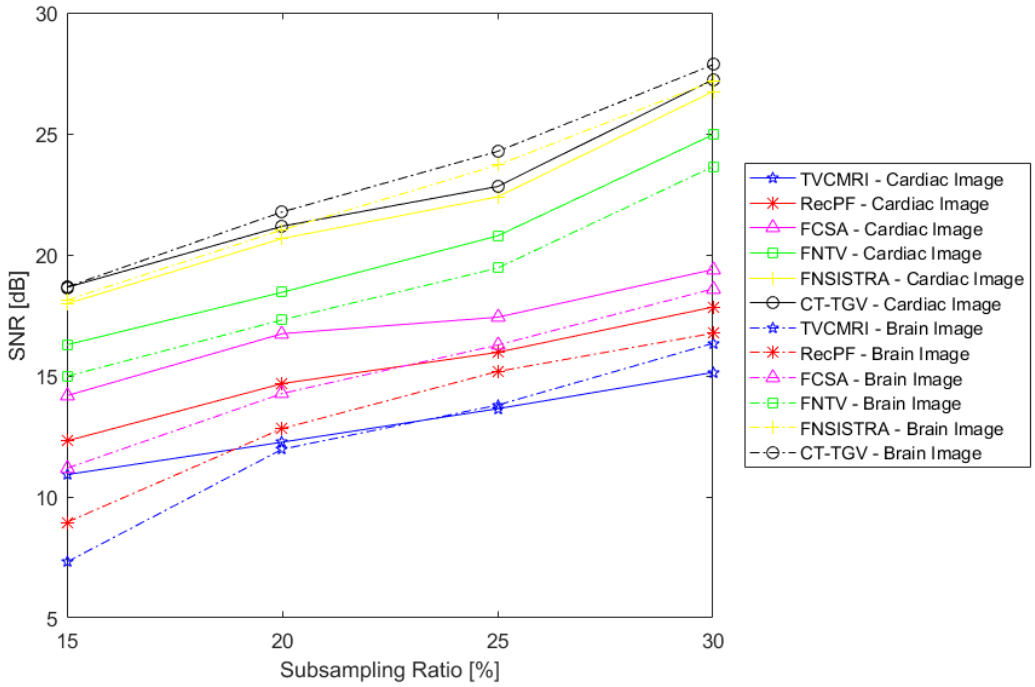

Figure 3.35 The performance of different algorithms with radial subsampling for cardiac and brain images

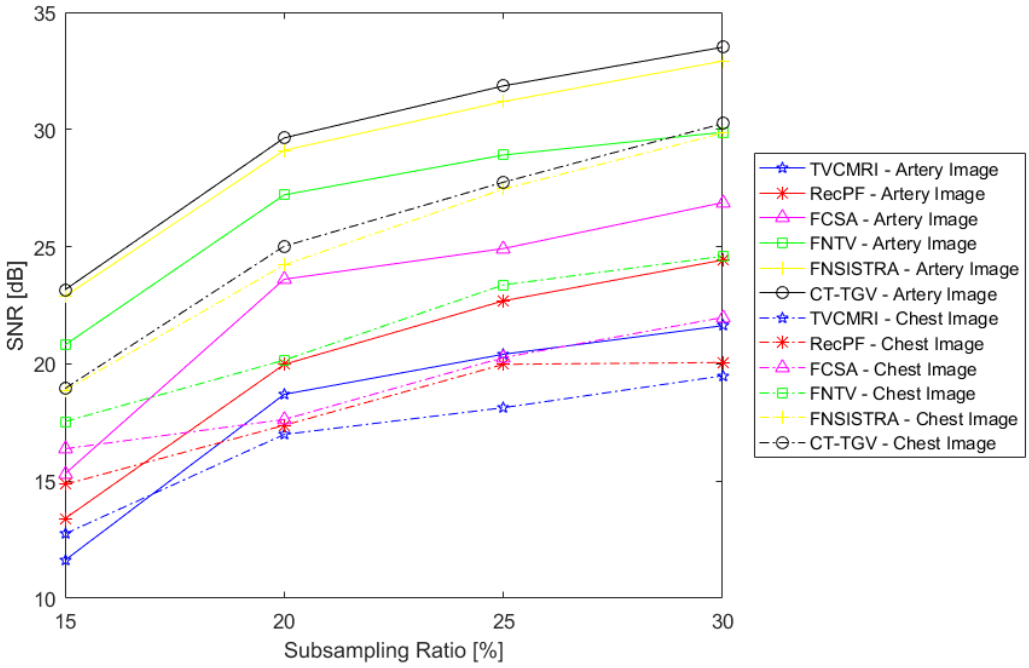

Figure 3.36 The performance of different algorithms with random subsampling for artery and chest images

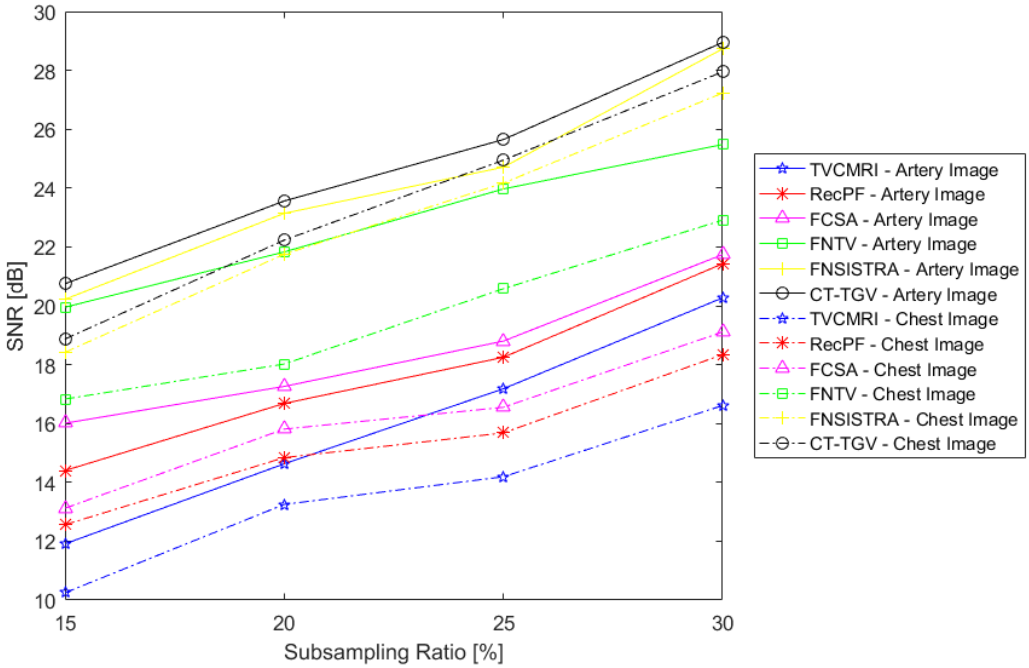

Figure 3.37 The performance of different algorithms with radial subsampling for artery and chest images

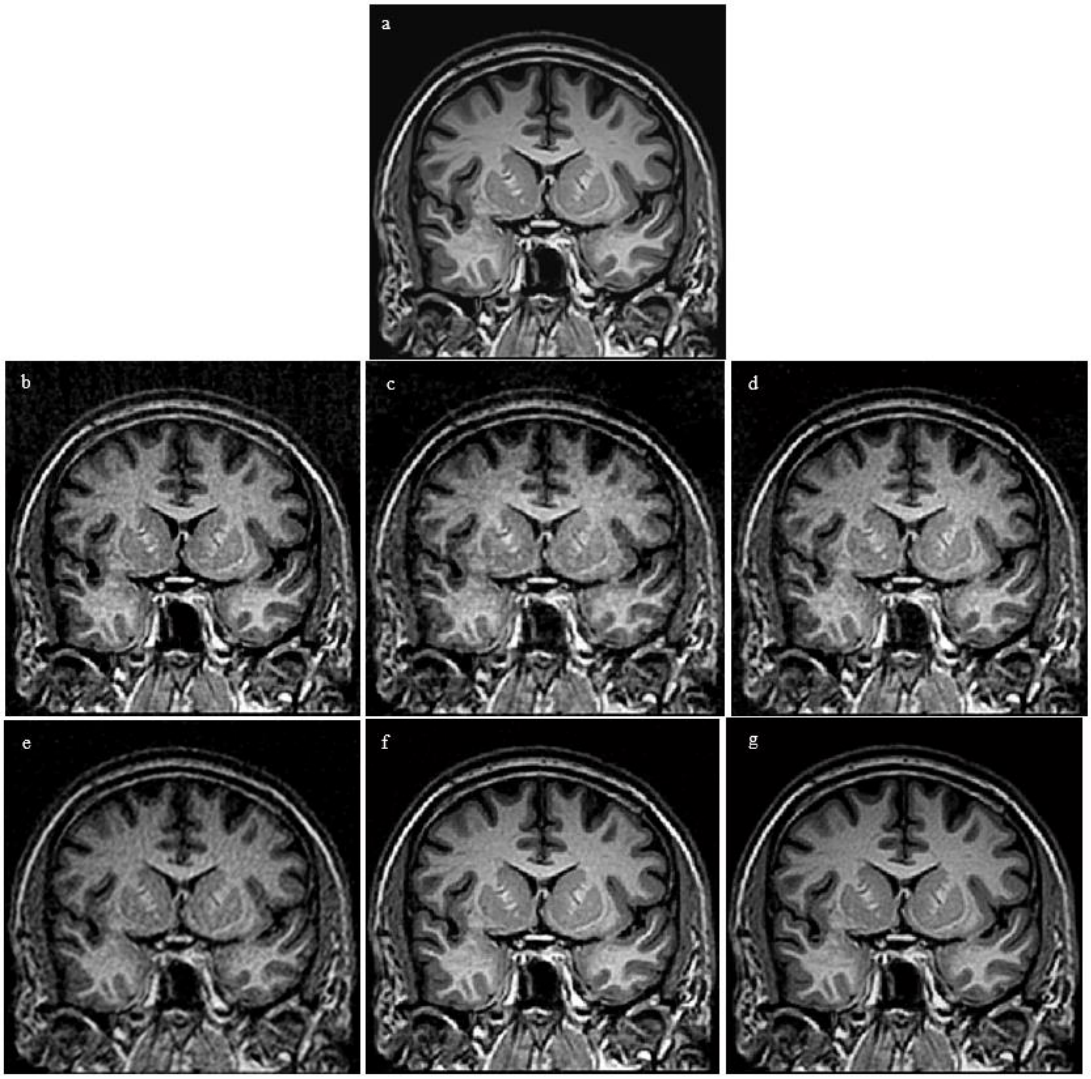

Figure 3.38 Reconstruction of brain image from 20 % random subsampling. a) Original, b) TVCMRI, c) RecPF, d) FCSA, e) FNTV, f) FNSISTRA, and g) CT-TGV

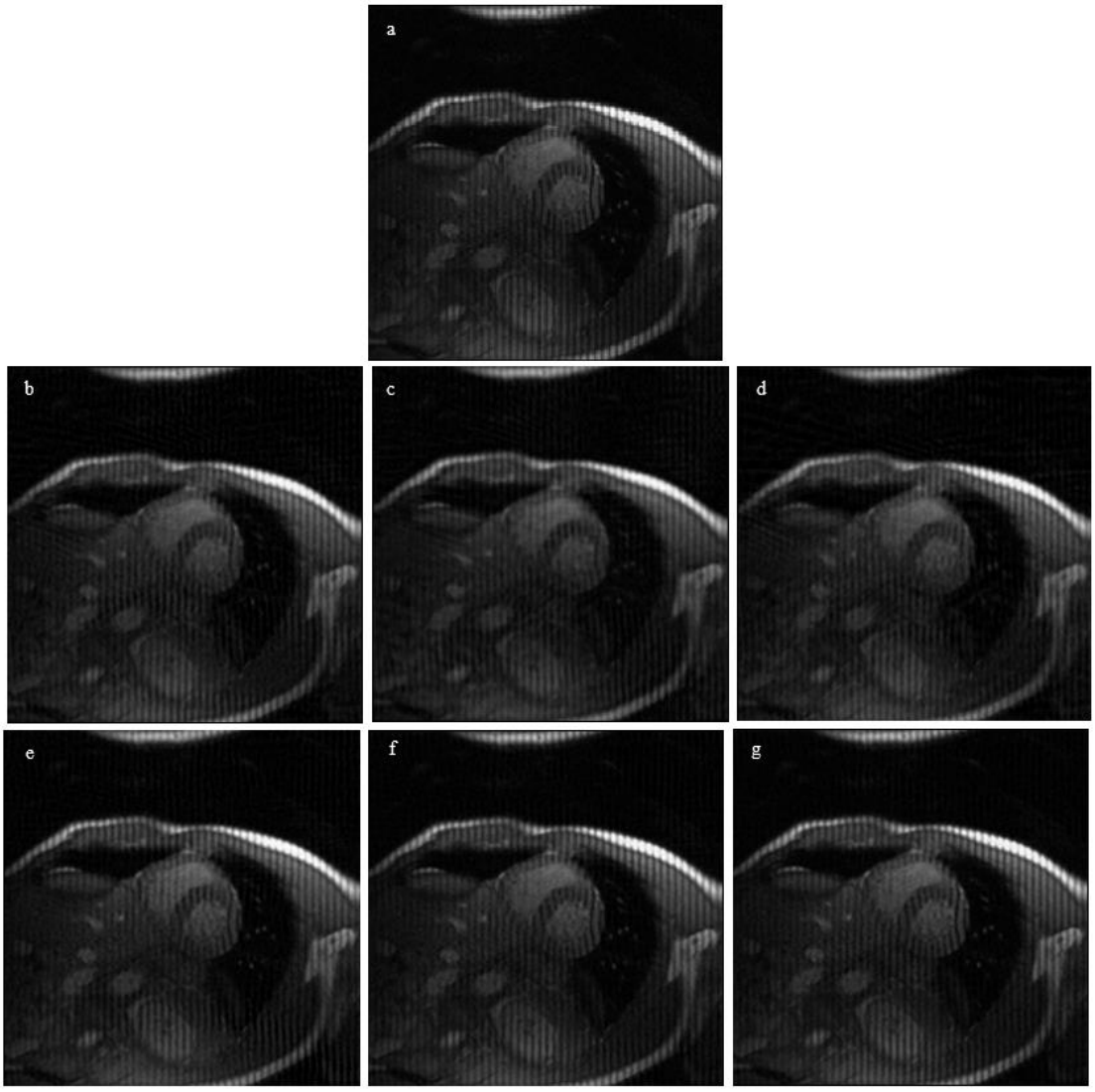

Figure 3.39 Reconstruction of cardiac image from 20 % random subsampling. a) Original, b) TVCMRI, c) RecPF, d) FCSA, e) FNTV, f) FNSISTRA, and g) CT-TGV

3.2.2. CS-NLTV

We evaluate the proposed CS-NLTV method here. For realization of the method we used curvelab implementation [83] to obtain curvelet coefficients because of the fast implementation. Figures 3.40 and 3.41 show the SNR plots for methods under comparison, SNR values are measured for various subsampling ratios, in random subsampling type. As it follows from the plots, the proposed CS-NLTV method has achieved a better performance for both types of subsampling.

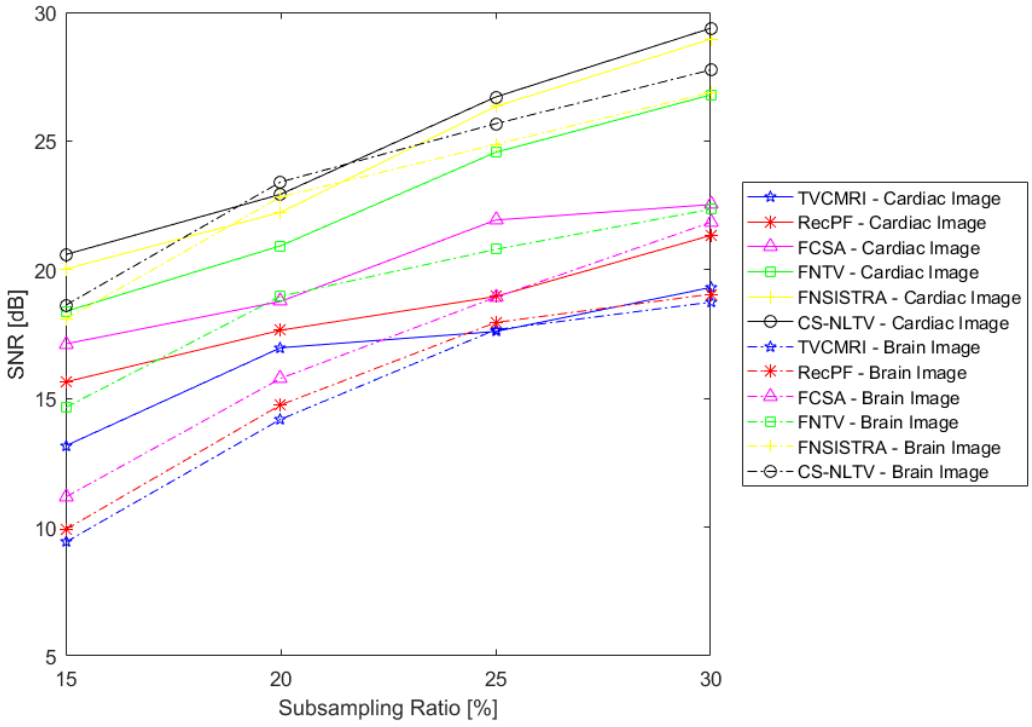

Figure 3.40 Performance of methods with random variable subsampling for cardiac and brain images.

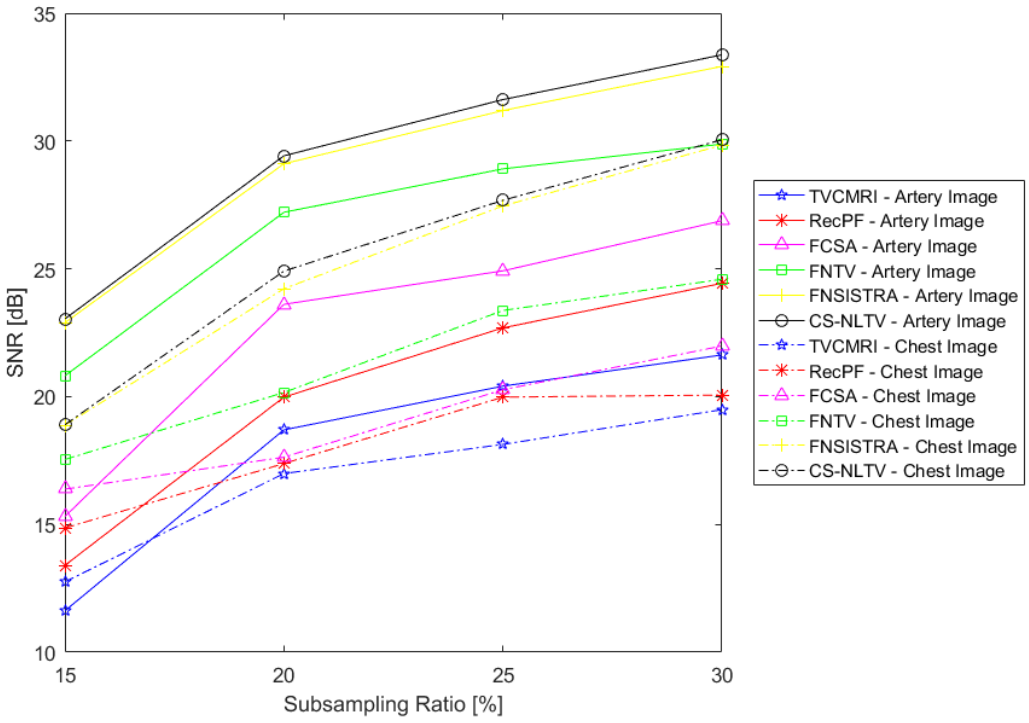

Figure 3.41 Performance of methods with random variable subsampling for cardiac and brain images.

3.2.3. SS-NLTV

We evaluate the proposed SS-NLTV method here. For realization of the method we used shearlab [84] to obtain shearlet coefficients because of the fast implementation.

Figures 3.42 - 3.45 show the SNR plots for methods under comparison, SNR values are measured for various subsampling ratios, in radial and random subsampling types. As it follows from the plots, the proposed SS-NLTV method has achieved a better performance for both types of subsampling. We demonstrate the reconstruction results for brain and cardiac image with random subsampling in Figures 3.46 and 3.47, respectively. Table 3.14 shows improvement of the average SNRs by SS-NLTV and five reference methods evaluated under random variable and radial subsampling at 20% subsampling ratios. The number of repeated experiments for computing the average SNRs is 10. The improvement of the quality of reconstruction by the proposed SS-NLTV method over a best among the reference methods that is by FNSISTRA is between 0.84 and 1.30 db. The superior performance of SS-NLTV is derived from utilization of nonlocal total variation which locates sharper edges and suppresses artifacts; and it is due to the exceptional spatial localization and directional selectivity of the shearlet transform.

Table 3.14 Improvement of the average signal to noise ratios (SNR) by SS-NLTV at 20% random and radial sampling ratios

	MR Image	TVCMRI	RecPF	FCSA	FNTV	FNSISTRA
Random Subsampling	Brain	9.94	9.38	8.35	5.16	1.30
	Cardiac	6.49	5.81	4.69	2.53	1.23
	Artery	11.57	10.29	6.66	3.06	1.16
	Chest	8.27	7.88	7.63	5.10	1.04
Radial Subsampling	Brain	10.15	9.30	7.85	4.81	1.09
	Cardiac	9.35	6.93	4.87	3.16	0.94
	Artery	9.35	7.30	6.72	2.15	0.84
	Chest	9.42	7.83	6.86	4.65	0.92

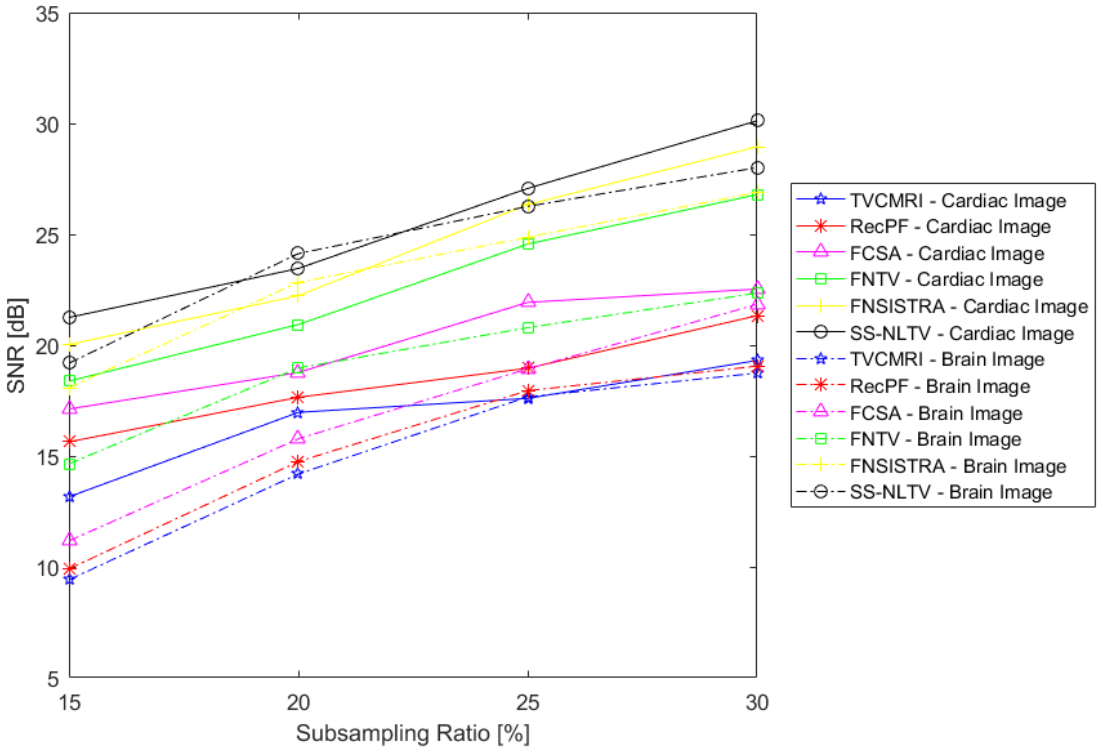

Figure 3.42 Performance of methods with random variable density subsampling for cardiac and brain images

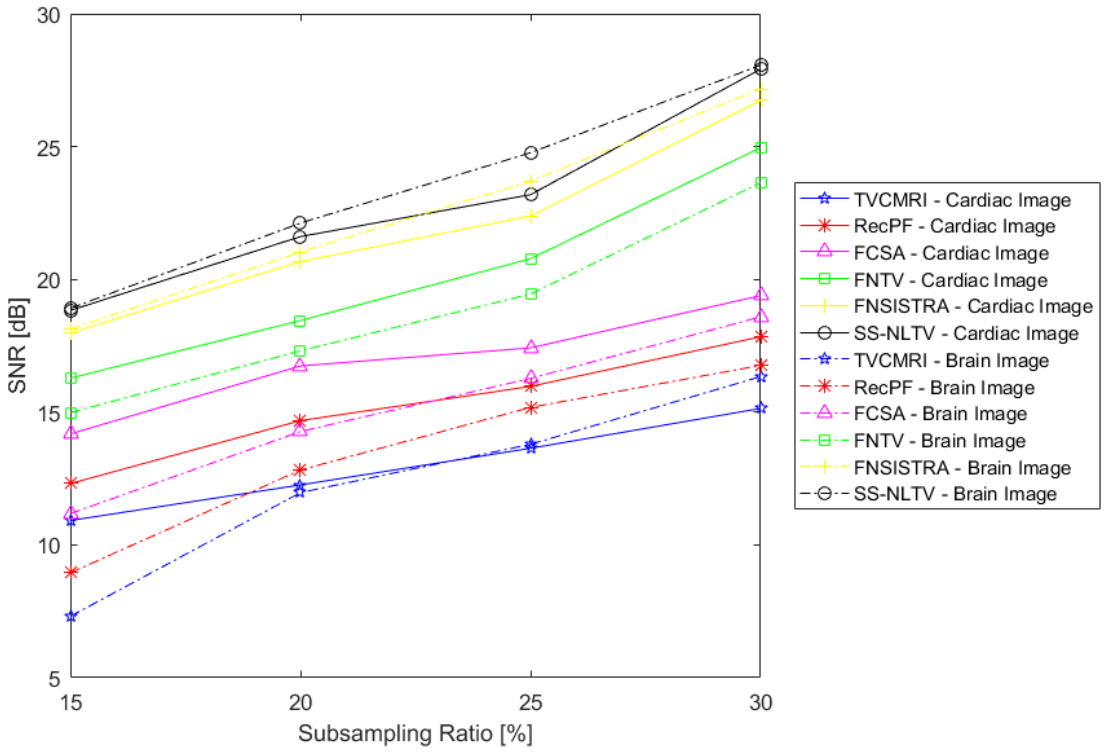

Figure 3.43 Performance of methods with radial subsampling for cardiac and brain images

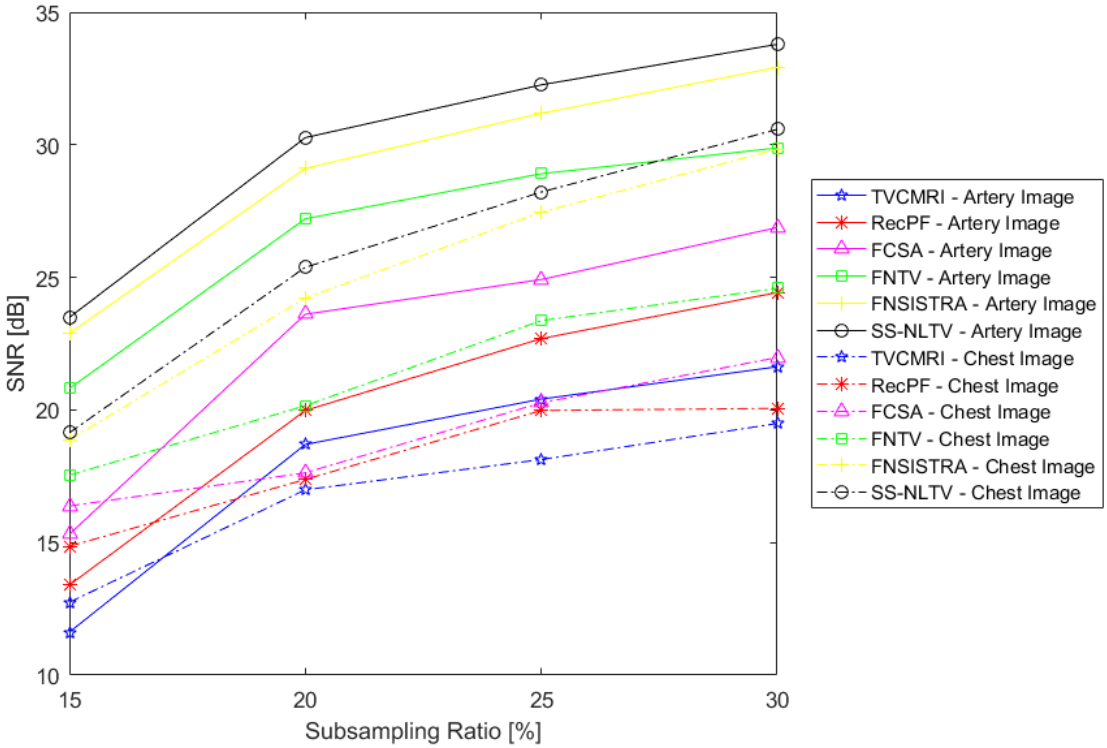

Figure 3.44 Performance of methods with random variable density subsampling for artery and chest images

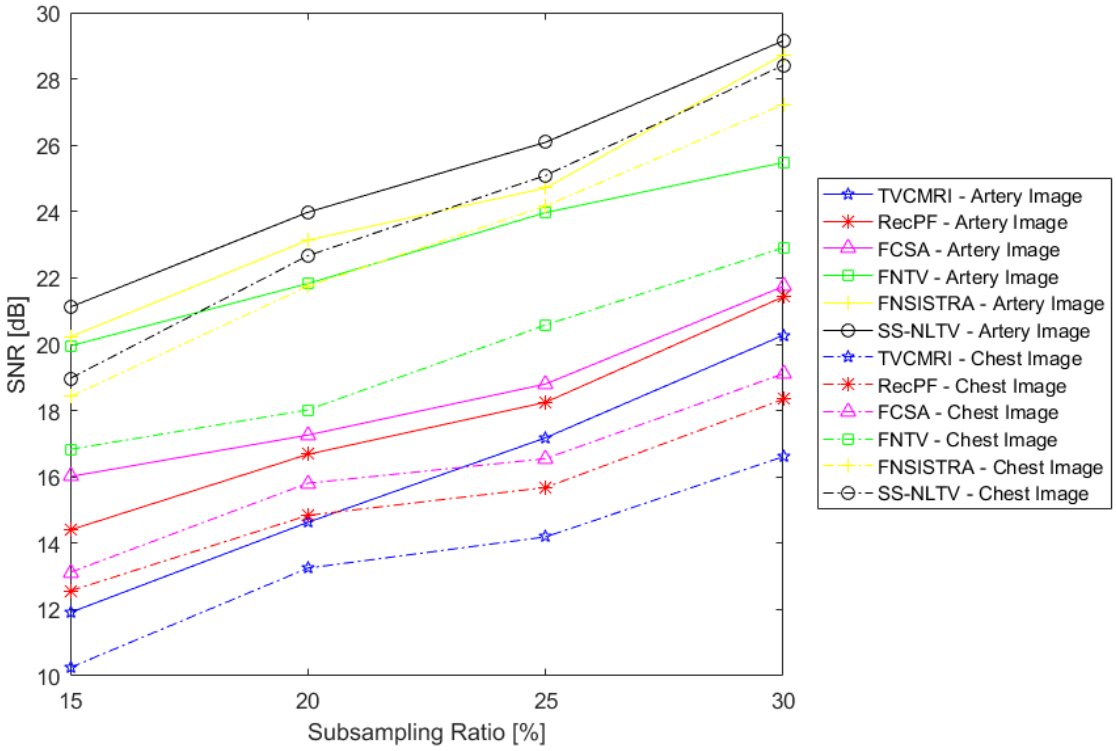

Figure 3.45 Performance of methods with radial subsampling for artery and chest images.

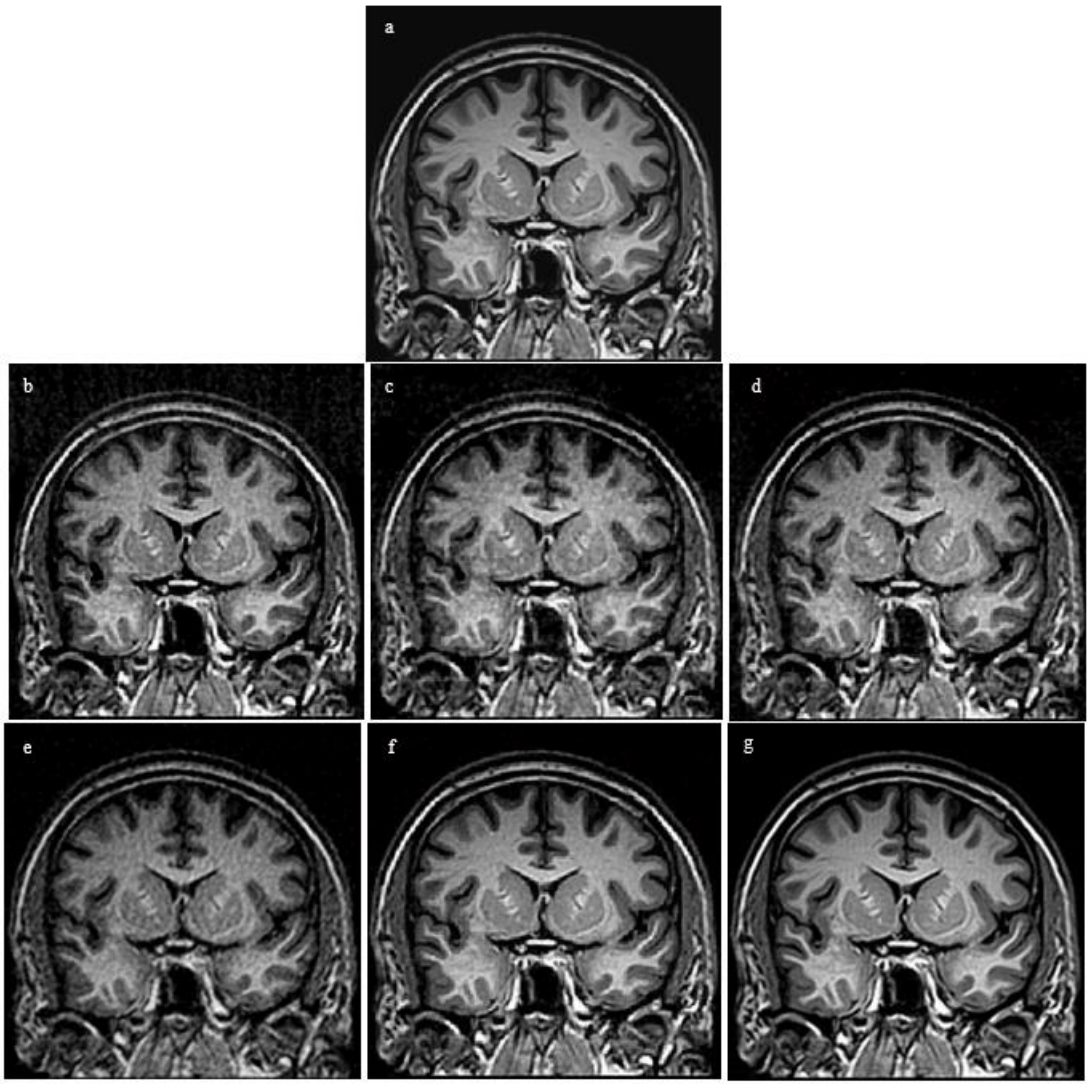

Figure 3.46 Reconstruction of brain image from 20 % random subsampling. a) Original, b) TVCMRI, c) RecPF, d) FCSA, e) FNTV, f) FNSISTRA, and g) SS-NLTV

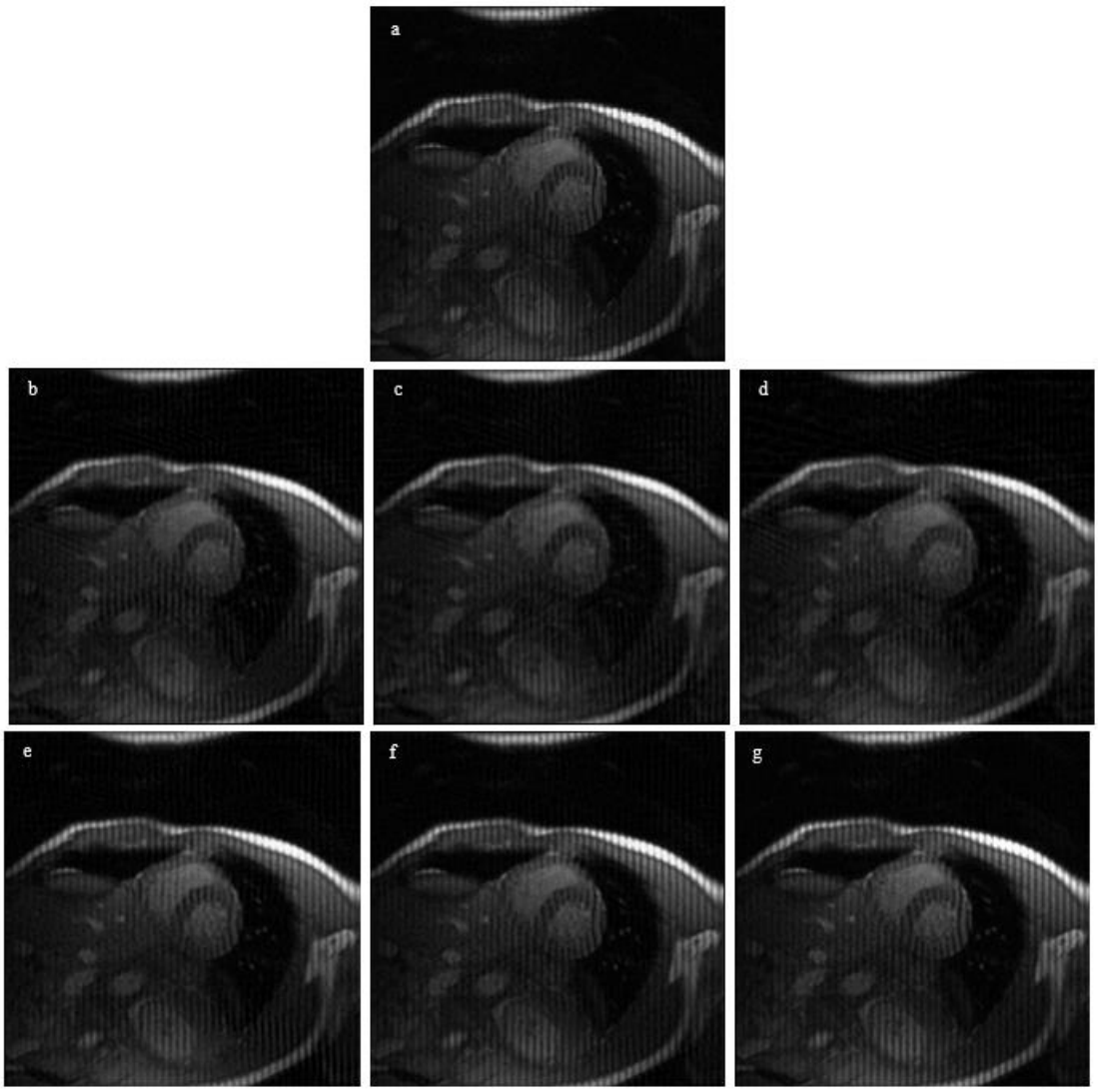

Figure 3.47 Reconstruction of cardiac image from 20 % random subsampling. a) Original, b) TVCMRI, c) RecPF, d) FCSA, e) FNTV, f) FNSISTRA, and g) SS-NLTV

CHAPTER 4- CONCLUSTIONS

Sparse signal reconstruction is used in medical imaging for achieving a higher efficiency of modern medical image modalities. However, the data reduction affects the quality of reconstructed signals. Medical, security, inspection, and non-destructive testing applications demand on high efficiency methods.

In this work, two major sparse signal reconstruction systems such as compressed sensing magnetic resonance imaging (MRI) and sparse-view computed tomography (CT) have been investigated. Both imaging modalities are complementary to each other and provide powerful means for medical diagnostics. However, they are expensive for both patients and insurance companies, and improving their performance is of a paramount importance. Although a significant contribution to this field has been done by research community, the efforts on improving the accuracy while reducing the cost are ongoing. In this work, we have contributed to the field by developing a number of high efficiency signal reconstruction techniques for sparse CT and MRI reconstruction.

Three CT reconstruction methods are proposed: algebraic iterative reconstruction-reprojection (AIRR), sparse-view CT reconstruction using curvelet and total variation based regularization (CTV), and sparse-view CT reconstruction based on nonconvex L1-L2 regularization.

The AIRR coupled with the shearlet regularization in image space achieves a better estimation in the projection space and achieved a better performance based on subjective and objective quality metrics. A unique combination of the curvelet regularizer and TV in the CTV method has led to the considerable improvement of the reconstruction quality. The Split-Bregman

(augmented Lagrangian) approach has been used as a solver which made it easy to incorporate multiple regularization terms including one based on the multiresolution transformation. Also, we propose a new nonconvex, Lipschitz continuous and non-smooth regularization model. Nonconvex L1-L2 CT method is formulated as a nonconvex constrained L1- L2 minimization problem and solved through a difference of convex algorithm and alternating direction of multiplier method which generates a better result than L0 or L1 regularizers in the CT reconstruction.

The neutron-photon tomography has been studied based on Monte-Carlo modelling to demonstrate shape reconstruction, material discrimination and visualization based on the proposed material signatures. 3D object reconstruction and material discrimination methods are proposed in sparse-view Neutron-Photon computed tomography (The scenes modelled using MCNP). A novel 2D signature based method is proposed for material discrimination in Neutron-Photon CT. Based on the proposed 2D signature for material identification, we have created the material library.

Three methods are proposed and evaluated: CT-TGV method exploits adaptively curvelet transform (CT) and total generalized variation (TGV) regulaizers. CS-NLTV method employs curvelet sparsity (CS) and nonlocal total variation (NLTV) regularization. SS-NLTV uses shearlet sparsity (SS) and nonlocal total variation (NLTV) regularization. In the three proposed methods, we have explored a novel approach of combining alternating direction method of multipliers (ADMM), splitting variables technique, and adaptive weighting to solve the formulated optimization problem. The results of the reconstruction obtained by the proposed methods on

different medical MRI datasets demonstrate a significant improvement of image reconstruction quality compared to the state-of-the-art methods.

REFERENCES

[1] Epstein C.L. (2003). *Introduction to the Mathematics of Medical Imaging*. Upper Saddle River, N.J: Prentice Hall.

[2] Hellier, C. (2003). *Handbook of nondestructive evaluation*. New York(NY): McGraw-Hill.

[3] Kirsch, A. (1996). *An introduction to the mathematical theory of inverse problems*. New York, NY: Springer

[4] Natterer, F. & Wübbeling, F. (2001). *Mathematical methods in image reconstruction*. Philadelphia, PA: Society for Industrial and Applied Mathematics

[5] Kuchment.P. (2014). *The radon transform and medical imaging*. Philadelphia, PA: Society for Industrial and Applied Mathematics.

[6] LaRoque, S.J., Sidky, E.Y., & Pan, X. (2008). Accurate image reconstruction from few-view and limited-angle data in diffraction tomography. *Journal of The Optical Society of America A*-Optics Image Science and Vision, 25(7):1772–1782.

[7]Velikina, J., Leng, S., & Chen, G. (2007). Limited view angle tomographic image reconstruction via total variation minimization. *Medical Imaging 2007: Physics of Medical Imaging*, 6510(2):651020

[8] Candes, E., Romberg, J., & Tao, T. (2006). Robust uncertainty principles: exact signal reconstruction from highly incomplete frequency information. *IEEE Transactions on Information Theory*, *52*(2), 489-509

[9] Donoho, D. (2006). Compressed sensing. *IEEE Transactions on Information Theory*, *52*(4), 1289-1306.

[10] Candès, E. J., Romberg, J. K., & Tao, T. (2006). Stable signal recovery from incomplete and inaccurate measurements. *Communications on Pure and Applied Mathematics*, *59*(8), 1207-1223

[11] Lustig, M., Donoho, D., Santos, J., & Pauly, J. (2008). Compressed Sensing MRI. *IEEE Signal Processing Magazine*, *25*(2), 72-82.

[12] Natarajan, B. K. (1995). Sparse Approximate Solutions to Linear Systems. *SIAM Journal on Computing*, *24*(2), 227-234

[13] He, L. K., Chang, T., Osher, S., Fang, T., & Speier, P. (2006). MR image reconstruction by using the iterative refinement method and nonlinear inverse scale space methods. UCLA CAM Report. 06-35.

[14] Block, K. T., Uecker, M., & Frahm, J. (2007). Undersampled radial MRI with multiple coils. Iterative image reconstruction using a total variation constraint. *Magnetic Resonance in Medicine*, *57*(6), 1086-1098.

[15] Chang, T.C., He, L., & Fang, T. (2006). Proceedings of the 13th Annual Meeting of ISMRM MR image reconstruction from sparse radial samples using Bregman iteration. Seattle, WA, 696.

[16] Lysaker, M., Lundervold, A., & Xue-Cheng Tai. (2003). Noise removal using fourth-order partial differential equation with applications to medical magnetic resonance images in space and time. *IEEE Transactions on Image Processing*, *12*(12), 1579-1590

[17] Lustig, M., Donoho, D., & Pauly, J. M. (2007). Sparse MRI: The application of compressed sensing for rapid MR imaging. *Magnetic Resonance in Medicine*, *58*(6), 1182-1195.

[18] Jung, H., Ye, J. C., & Kim, E. Y. (2007). Improved k–t BLAST and k–t SENSE using FOCUSS. *Physics in Medicine and Biology*, *52*(11), 3201-3226.

[19] Ye, J. C., Tak, S., Han, Y., & Park, H. W. (2007). Projection reconstruction MR imaging using FOCUSS. *Magnetic Resonance in Medicine*, *57*(4), 764-775

[20] Candès, E. J., Wakin, M. B., & Boyd, S. P. (2008). Enhancing Sparsity by Reweighted ℓ 1 Minimization. *Journal of Fourier Analysis and Applications*, *14*(5-6), 877-905

[21] Chartrand, R., & Wotao Yin. (2008). Iteratively reweighted algorithms for compressive sensing. *2008 IEEE International Conference on Acoustics, Speech and Signal Processing*.

[22] Rao, B., & Kreutz-Delgado, K. (1999). An affine scaling methodology for best basis selection. *IEEE Transactions on Signal Processing*, *47*(1), 187-200.

[23] Trzasko, J. Manduca, A. & Borisch, E. (2009). Highly undersampled magnetic resonance image reconstruction via homotopic L0-minimization. *IEEE Transactions on Medical Imaging*, *28*(1), 106-121.

[24] Shiqian Ma, Wotao Yin, Yin Zhang, & Chakraborty, A. (2008). An efficient algorithm for compressed MR imaging using total variation and wavelets. *2008 IEEE Conference on Computer Vision and Pattern Recognition*

[25] Junfeng Yang, Yin Zhang, & Wotao Yin. (2010). A Fast Alternating Direction Method for TVL1-L2 Signal Reconstruction From Partial Fourier Data. *IEEE Journal of Selected Topics in Signal Processing*, *4*(2), 288-297

[26] Gabay, D., & Mercier, B. (1976). A dual algorithm for the solution of nonlinear variational problems via finite element approximation. *Computers & Mathematics with Applications*, *2*(1), 17-40

[27] Huang, J., Zhang, S., & Metaxas, D. (2011). Efficient MR image reconstruction for compressed MR imaging. *Medical Image Analysis*, *15*(5), 670-679

[28] Gopi, V. P., Palanisamy, P., Wahid, K. A., & Babyn, P. (2013). MR Image Reconstruction Based on Iterative Split Bregman Algorithm and Nonlocal Total Variation. *Computational and Mathematical Methods in Medicine, 2013*, 1-16.

[29] Gopi, V. P., Palanisamy, P., Wahid, K. A., & Babyn, P. (2013). MR image reconstruction based on framelets and nonlocal total variation using split Bregman method. *International Journal of Computer Assisted Radiology and Surgery*, *9*(3), 459-472

[30] Osher, S., Burger, M., Goldfarb, D., Xu, J., & Yin, W. (2005). An Iterative Regularization Method for Total Variation-Based Image Restoration. *Multiscale Modeling & Simulation*, *4*(2), 460-489

[31] Guo, W., Qin, J., & Yin, W. (2014). A New Detail-Preserving Regularization Scheme. *SIAM Journal on Imaging Sciences*, *7*(2), 1309-1334

[32] Pejoski, S., Kafedziski, V., & Gleich, D. (2015). Compressed Sensing MRI Using Discrete Nonseparable Shearlet Transform and FISTA. *IEEE Signal Processing Letters*, *22*(10), 1566-1570.

[33] Wang-Q Lim. (2013). Nonseparable Shearlet Transform. *IEEE Transactions on Image Processing*, *22*(5), 2056-2065

[34] Beck, A., & Teboulle, M. (2009). A Fast Iterative Shrinkage-Thresholding Algorithm for Linear Inverse Problems. *SIAM Journal on Imaging Sciences*, *2*(1), 183-202

[35] Hao, W., Qu, X., Dong, Z., & Li, J. (2013). Fast iterative contourlet thresholding for compressed sensing MRI. *Electronics Letters*, *49*(19), 1206-1208.

[36] Kim, J. H., Kwak, K. Y., Park, S. B., & Cho, Z. H. (1985). Projection Space Iteration Reconstruction-Reprojection. *IEEE Transactions on Medical Imaging*, *4*(3), 139-143.

[37] Nassi, M., Brody, W. R., Medoff, B. P., & Macovski, A. (1982). Iterative Reconstruction-Reprojection: An Algorithm for Limited Data Cardiac-Computed Tomography. *IEEE Transactions on Biomedical Engineering*, *BME-29*(5), 333-341

[38] Duan, X., Zhang, L., Xing, Y., Chen, Z., & Cheng, J. (2009). Few-View Projection Reconstruction With an Iterative Reconstruction-Reprojection Algorithm and TV Constraint. *IEEE Transactions on Nuclear Science*, *56*(3), 1377-1382.

[39] Gerchberg, R. (1974). Super-resolution through Error Energy Reduction. *Optica Acta: International Journal of Optics*, *21*(9), 709-720

[40] Papoulis, A. (1975). A new algorithm in spectral analysis and band-limited extrapolation. *IEEE Transactions on Circuits and Systems*, *22*(9), 735-742.

[41] Censor, Y., & Elfving, T. (2002). Block-Iterative Algorithms with Diagonally Scaled Oblique Projections for the Linear Feasibility Problem. *SIAM Journal on Matrix Analysis and Applications*, *24*(1), 40-58

[42] Vandeghinste, B., Goossens, B., Van Holen, R., Vanhove, C., Pizurica, A., Vandenberghe, S., & Staelens, S. (2013). Iterative CT Reconstruction Using Shearlet-Based Regularization. *IEEE Transactions on Nuclear Science*, *60*(5), 3305-3317.

[43] Ming Jiang, & Ge Wang. (2003). Convergence of the simultaneous algebraic reconstruction technique (SART). *IEEE Transactions on Image Processing*, *12*(8), 957-961.

[44] Sauer, K., & Bouman, C. (1993). A local update strategy for iterative reconstruction from projections. *IEEE Transactions on Signal Processing*, *41*(2), 534-548.

[45] Guo, K., & Labate, D. (2007). Optimally Sparse Multidimensional Representation Using Shearlets. *SIAM Journal on Mathematical Analysis*, *39*(1), 298-318.

[46] Easley, G., Labate, D., & Lim, W. (2008). Sparse directional image representations using the discrete shearlet transform. *Applied and Computational Harmonic Analysis*, *25*(1), 25-46

[47] Kutyniok, G., & Labate, D. (2008). Resolution of the wavefront set using continuous shearlets. *Transactions of the American Mathematical Society*, *361*(05), 2719-2754.

[48] Sheng Yi, Labate, D., Easley, G., & Krim, H. (2009). A Shearlet Approach to Edge Analysis and Detection. *IEEE Transactions on Image Processing*, *18*(5), 929-941

[49] Guo, K., Labate, D., & Lim, W. (2009). Edge analysis and identification using the continuous shearlet transform. *Applied and Computational Harmonic Analysis*, *27*(1), 24-46

[50] Goossens, B., Aelterman, J., Luong, H., Pizurica, A., & Philips, W. (2009). Efficient design of a low redundant Discrete Shearlet Transform. *2009 International Workshop on Local and Non-Local Approximation in Image Processing*

[51] Daubechies, I. (1992). *Ten lectures on wavelets*. Philadelphia: Society for Industrial and Applied Mathematics.

[52] Da Cunha, A., Zhou, J., & Do, M. (2006). The Nonsubsampled Contourlet Transform: Theory, Design, and Applications. *IEEE Transactions on Image Processing*, *15*(10), 3089-3101.

[53] Shepp, L. A., & Logan, B. F. (1974). Reconstructing Interior Head Tissue from X-Ray Transmissions. *IEEE Transactions on Nuclear Science*, *21*(1), 228-236.

[54] Goldstein, T., & Osher, S. (2009). The Split Bregman Method for L1-Regularized Problems. *SIAM Journal on Imaging Sciences*, *2*(2), 323-343.

[55] Jean-Luc Starck, Candes, E., & Donoho, D. (2002). The curvelet transform for image denoising. *IEEE Transactions on Image Processing*, *11*(6), 670-684.

[56] Afonso, M. V., Bioucas-Dias, J. M., & Figueiredo, M. A. (2011). An Augmented Lagrangian Approach to the Constrained Optimization Formulation of Imaging Inverse Problems. *IEEE Transactions on Image Processing*, *20*(3), 681-695

[57] Wu, H., Maier, A., & Hornegger, J. (2013). Iterative CT Reconstruction Using Curvelet-Based Regularization. *Bildverarbeitung für die Medizin 2013*, 229-234.

[58] Hestenes, M., & Stiefel, E. (1952). Methods of conjugate gradients for solving linear systems. *Journal of Research of the National Bureau of Standards*, *49*(6), 409.

[59] Pham-Dinh T., Le-Thi, H.A. (1997). Convex analysis approach to D.C. programming: Theory, algorithms and applications. ACTA MATHEMATICA VIETNAMICA. 22(1), 289–355.

[60] Boyd,S., Parikh, N., Chu, E., Peleato, B., & Eckstein, J. Distributed optimization and statistical learning via the alternating direction method of multipliers, *Foundations and Trends® in Machine Learning*, *3*(1), 1-122

[61] Eberhardt, J., Rainey, S., Stevens, R., Sowerby, B., & Tickner, J. (2005). Fast neutron radiography scanner for the detection of contraband in air cargo containers. *Applied Radiation and Isotopes*, *63*(2), 179-188

[62] Los Alamos National Laboratory. (2003). A general Monte Carlo N-Particle transport code. LAUR-03-1987, Verison 5.

[63] Hartman, J., Yazdanpanah, A. P., Barzilov, A., & Regentova, E. (2016). 3D imaging using combined neutron-photon fan-beam tomography: A Monte Carlo study. *Applied Radiation and Isotopes*, *111*, 110-116

[64] Kak, A. C., & Slaney, M. (2001). Principles of Computerized Tomographic Imaging.Society of Industrial and Applied Mathematics (1st edition).

[65] Sidky, E. Y., & Pan, X. (2008). Image reconstruction in circular cone-beam computed tomography by constrained, total-variation minimization. *Physics in Medicine and Biology*, *53*(17), 4777-4807.

[66] Sidky, E. Y., Kao, C., & Pan, X. (2006). Accurate image reconstruction from few-views and limited-angle data in divergent-beam CT. Journal of X-Ray Science and Technology, 14(2), 119–139.

[67] Xu, G., Li, M., Gopinath, A., & Bajaj, C. L. (2011). Inversion of Electron Tomography Images Using L2-Gradient Flows ---- Computational Methods. *Journal of Computational Mathematics*, *29*(5), 501-525

[68] Compton, R., Osher, S., & Bouchard, L. (2012). Hybrid regularization for mri reconstruction with static field inhomogeneity correction. *2012 9th IEEE International Symposium on Biomedical Imaging (ISBI)* 650-655.

[69] Yu, H., & Wang, G. (2009). Compressed sensing based interior tomography. *Physics in Medicine and Biology*, *54*(13), 4341-4341

[70] Yazdanpanah, A. P., & Regentova, E. E. (2016). Sparse-View CT Reconstruction Using Curvelet and TV-Based Regularization. *Lecture Notes in Computer Science*, 672-677.

[71] Yu, H., & Wang, G. (2010). A soft-threshold filtering approach for reconstruction from a limited number of projections. *Physics in Medicine and Biology*, *55*(13), 3905-3916

[72] Bredies, K., Kunisch, K., & Pock, T. (2010). Total Generalized Variation. *SIAM Journal on Imaging Sciences*, *3*(3), 492-526

[73] Setzer, S., Steidl, G., & Teuber, T. (2011). Infimal convolution regularizations with discrete ℓ1-type functionals. *Communications in Mathematical Sciences*, *9*(3), 797-827.

[74] Knoll, F., Bredies, K., Pock, T., & Stollberger, R. (2010). Second order total generalized variation (TGV) for MRI. *Magnetic Resonance in Medicine*, *65*(2), 480-491.

[75] Candès, E., Demanet, L., Donoho, D., & Ying, L. (2006). Fast Discrete Curvelet Transforms. *Multiscale Modeling & Simulation*, *5*(3), 861-899.

[76] Candès, E. J., & Donoho, D. L. (2003). New tight frames of curvelets and optimal representations of objects with piecewiseC2singularities. *Communications on Pure and Applied Mathematics*, *57*(2), 219-266

[77] Yazdanpanah, A. P., Regentova E., & Bebis G. (2016). Algebraic Iterative Reconstruction-Reprojection (AIRR) Method for High Performance Sparse-View CT Reconstruction. *Applied Mathematics & Information Sciences*, *10*(6), 2007-2014.

[78] Wang, Z., Bovik, A., Sheikh, H., & Simoncelli, E. (2004). Image Quality Assessment: From Error Visibility to Structural Similarity. *IEEE Transactions on Image Processing*, *13*(4), 600-612.

[79] FORBILD group. Head Phantom. (n.d.). Retrieved from http://www.imp.uni-erlangen.de/phantoms/head/head.html

[80] A Feldkamp, L. A., Davis, L. C., & Kress, J. W. (1984). Practical cone-beam algorithm. *Journal of the Optical Society of America A*, *1*(6), 612-619.

[81] Jain, A. K. (2010). Data clustering: 50 years beyond K-means. *Pattern Recognition Letters*, *31*(8), 651-666.

[82] Xu, R. K., & WunschII, D. (2005). Survey of Clustering Algorithms. *IEEE Transactions on Neural Networks*, *16*(3), 645-678

[83] Curvelab. (n.d.). Retrieved from http://www.curvelet.org/

[84] Kutyniok, G., Shahram, M., & Zhuang, X. (2012). ShearLab: A Rational Design of a Digital Parabolic Scaling Algorithm. *SIAM Journal on Imaging Sciences*, *5*(4), 1291-1332.

CURRICULUM VITAE

Graduate College
University of Nevada, Las Vegas

Ali Pouryazdanpanah Kermani

Email: pouryazd@unlv.nevada.edu

Dissertation Examination Committee:

Chairperson, Dr. Emma Regentova, Ph.D.
Committee Member, Dr. Venkatesan Muthukumar, Ph.D.
Committee Member, Dr. Shahram Latifi, Ph.D.
Graduate College Faculty Representative, Dr. Alexander Barzilov, Ph.D.